Title

The Chemical Kinetics of Reactive Intermediates in Organic Aerosol Particles

Author

Reynolds, Ryan Scott

Publication Date

2024

Peer reviewed|Thesis/dissertation

The Chemical Kinetics of Reactive Intermediates in Organic Aerosol Particles

by

Ryan Scott Reynolds

A dissertation submitted in partial satisfaction of the

requirements for the degree of

Doctor of Philosophy

in

Chemistry

in the

Graduate Division

of the

University of California, Berkeley

Committee in charge:

Dr. Kevin R. Wilson, co-chair
Professor Richard Saykally, co-chair
Professor Evan R. Williams
Professor Allen H. Goldstein

Fall 2024

Abstract

The Chemical Kinetics of Reactive Intermediates in Organic Aerosol Particles

by

Ryan Scott Reynolds

Doctor of Philosophy in Chemistry

University of California, Berkeley

Dr. Kevin R. Wilson, Co-Chair
Professor Richard J. Saykally, Co-Chair

Aerosols composed primarily of organic constituents are unique chemical environments due to their high surface to volume ratio, their range of chemical complexity, and their variable phase and mixing behavior. In the atmosphere, organic aerosols can have significant impacts on climate, such as when they act as cloud condensation nuclei, as well as impacts on air quality and human health. Additionally, organic aerosols have many applications in industrial processes, such as paints, coatings, and chemical synthesis. An understanding of the mechanisms of chemical transformation in organic aerosol particles is therefore key to understanding how these particles affect both environmental and industrial processes. In oxidation reactions, the particle-phase chemistry and kinetics are often determined by the behavior of reactive intermediates formed after an initiating reaction step. These reactive intermediates can include the stabilized Criegee Intermediate (sCI) formed during ozonolysis, or hydroxyl (OH), alkoxy (RO), or alkylperoxy (RO_2) radicals formed during radical chain reactions. The reaction kinetics of these various intermediate species are diverse, often interconnected, and can be affected by the properties of the particle matrix, making them difficult to measure.

The first chapter of this thesis introduces the effective reactive uptake coefficient (γ_{eff}), which is used to quantify heterogeneous reaction kinetics. Then experimental results measuring the reaction kinetics of the ozonolysis of alkene-containing aerosol using various forms of aerosol mass spectrometry are presented. In Chapter Two, Atmospheric Pressure Chemical Ionization Mass Spectrometry (APCI-MS) is used to measure the reaction of aerosols composed of a mixture of an alkene and a saturated acid. The decay kinetics of the alkene, as captured by γ_{eff} are used to determine the extent of chain cycling during ozonolysis. The decay kinetics of the acid are used to measure the particle-phase reaction rate between stabilized Criegee Intermediates (sCI) and carboxylic acids, which is found to be six orders of magnitude slower than the corresponding gas-phase reaction rate.

In Chapter Three, temperature-dependent flow tube experiments are conducted using vacuum ultraviolet (VUV) photoionization aerosol mass spectrometry (AMS) to reveal how the energetics of various reaction steps change with temperature. The γ_{eff} of neat alkene aerosol is found to double as temperature is lowered from 293 K to 263 K, which is attributed to a buildup of particle-phase sCI at low temperatures that enhance chain cycling chemistry. The branching ratio between the unimolecular reactions of the sCI and the bimolecular reaction with the acid is investigated, suggesting an activation energy of at least 40 kJ mol^{-1}.

In Chapter Four, progress is described toward an aerosol delivery system for organocerium photocatalysts, which have the potential to perform chemoselective redox chemistry on target molecules for organic synthesis. An apparatus for generating and detecting aerosol containing a Ce (IV) catalyst and target reactants in submicron (~100 nm diameter) organic solvent droplets is developed, allowing particle-phase Ce-ligand complexes to be detected via nanospray ionization (NSI) mass spectrometry. The structures of these complexes in the presence of two different carboxylic acid ligands are discussed and identified as primarily 4-coordinate complexes with 1 or 2 Ce metal centers. These results have implications for the design of future catalysts and experimental apparatus that make use of the particle surface to enhance catalytic performance. Finally, in the fifth chapter, the key findings presented in this thesis are briefly summarized and discussed.

Dedication & Acknowledgements

This thesis is dedicated to my parents, John and Cheryl Reynolds.

Mom, thank you for nurturing my first curiosity about chemistry—we've come a long way from the Oxnard Public Library.

Dad, thank you for saving me from hating math—we've come a long way from Algebra I.

For so many reasons, both obvious and not, none of this would have happened without you.

I also want to acknowledge my many friends at Christ Church Berkeley, who have been family to me these past five years. Thank you for caring for me, praying for me, and even feeding me during some of the toughest challenges of my life. I will cherish your examples of kindness and generosity for many years to come.

I would also like to thank the many current and former Wilson group members (and other denizens of 6-2203) for their camaraderie and encouragement, for honing my paper-reading skills, and for always being willing and excited to talk about science—from navigating instrument and data analysis problems, to dreaming about new experiments. Each of you have made my graduate school and LBL experience so much richer by your presence in it. I particularly want to acknowledge Meirong Zeng, whose mentorship and training in my first few years of graduate school were indispensable, and whose friendship helped make the bleakest COVID times feel a little less bleak.

I'd also like to thank Rich Saykally and the members of the Saykally group for their support in navigating graduate school both on campus and up at LBL.

Finally, I want to give many thanks to Kevin: for being an excellent and patient mentor, for encouraging my growth as a scientist, for providing insight and direction each time I've been stuck, for making yourself eminently available whenever I've had a question. I don't know where I would be today without your guidance and support—thank you.

Car enfin qu'est-ce que l'homme dans la nature? Un néant à l'égard de l'infini, un tout à l'égard du néant: un milieu entre rien et tout.

For what is man in nature? A nothingness when compared to the infinite, everything when compared to nothingness: an intermediate between nothing and everything.

*—Blaise Pascal, Pensées**

* I would also like to thank M. Pascal for his relentless pessimism about human efforts to understand things much bigger (or smaller) than themselves. Although this has made it very difficult to pull a quote sufficiently starry-eyed for a thesis dedication, it is—after 5 years of my own such human efforts—a little hard to argue with. *Joie, joie, pleurs de joie.*

Table of Contents

Chapter 1. Introduction: The Role of Effective Uptake Coefficients in Aerosol Chemistry

Figures and content in this chapter are adapted from Reynolds, R.S.; Wilson, K.R. Unraveling the Meaning of Effective Uptake Coefficients in Multiphase and Aerosol Chemistry. Acc. Chem. Res. **2024, Under review.*

1.1 Introduction

An aerosol is defined as a relatively stable suspension of condensed-phase particles entrained in a gas.[1] Any chemical reaction occurring in an aerosol, therefore, inherently involves multiple phases. As a result, standard descriptions of reaction kinetics, such as rate constants measured in only the gas or aqueous phase, are insufficient on their own to describe the kinetics of aerosol reactions.

For this reason, multiphase reactions are often quantified in terms of a reactive uptake coefficient (γ). γ is defined as the net loss of gas-phase molecules entering the condensed phase, divided by their collision rate with the surface.[1,2] This definition developed in the context of reactions on aqueous interfaces, *e.g.* cloud droplets in the atmosphere, by expanding on notions of mass accommodation coefficients (α).[3,4] Measuring γ can be straightforward for many reaction systems, such as by use of a Knudsen cell or coated flow tube, given that it only requires monitoring relative changes in the flux of gas and not absolute concentrations,[1] and thus can account for the effects of evaporation, desorption, diffusion, and reaction.[5]

However, interpreting the physical meaning of γ has been shown to be an increasing challenge over several decades of measurement and analysis. For aerosol reactions, simple frameworks, such as the resistor model,[4] which assumes that the particle is well-mixed and all processes contributing to gas uptake are independent, often break down when applied to systems where reaction and diffusion are strongly coupled.[6,7] As attention in aerosol research has shifted toward particles of primarily organic constituents, such descriptions of the kinetics have been stretched to the edges of their useful working ranges[8] for organic aerosols with semisolid and highly viscous phase states, in which high concentrations and slow mixing of reactants prove troublesome for analysis in terms of limiting kinetic cases.[9,10] Additionally, for reactions involving gas-phase radicals, γ is often hard to measure, as radical concentrations are generally low, difficult to detect, and can induce significant amounts of chemistry in the particle phase that is not directly reflected in gas-phase measurements.

Alternately, heterogeneous reactions on aerosols with primarily organic constituents can be described in terms of the *effective* uptake coefficient, γ_{eff}, defined as the consumption rate of a condensed-phase reactant relative to the collision rate of the impinging gas (Figure 1.1).[11] In such a measurement (typically by an aerosol mass spectrometer), the collision rate of a trace gas with the particle surface is used as a clock against which the reaction time can be measured. For an aerosol with particles composed of an arbitrary condensed-phase reactant R undergoing reaction with a gas X, γ_{eff} is defined in terms of the loss of R,

$$\frac{d[R]}{dt} = -k_{R-X}[R][X] = -\gamma_{X,eff}^{R} \cdot (C_p \cdot A) \cdot f \cdot J_{coll,X} \quad \text{Eq. (1.1)}$$

where $k_{R\text{-}X}$ is the phenomenological 2nd-order rate constant of the reaction between R and X, C_p and A are the number concentration of the aerosol and surface area of a single aerosol particle, respectively. f is the fraction of R remaining in the aerosol at any point during the reaction, and $J_{coll,X}$ is the flux of X onto the particle surface, given by,

$$J_{coll,X} = \frac{\bar{c}[X]}{4} \quad \text{Eq. (1.2)}$$

where $\bar{c}$ is the mean molecular speed of X. For single-component well-mixed spherical particles this expression reduces to,

$$\gamma_{X,eff}^{R} = \frac{4k_{R-X}D_{surf}\rho_0 N_A}{6\bar{c}M_R} \quad \text{Eq. (1.3)}$$

with D_{surf} the surface-weighted particle diameter, ρ_0 the density of R, M_R its molar mass, and N_A Avogadro's number.

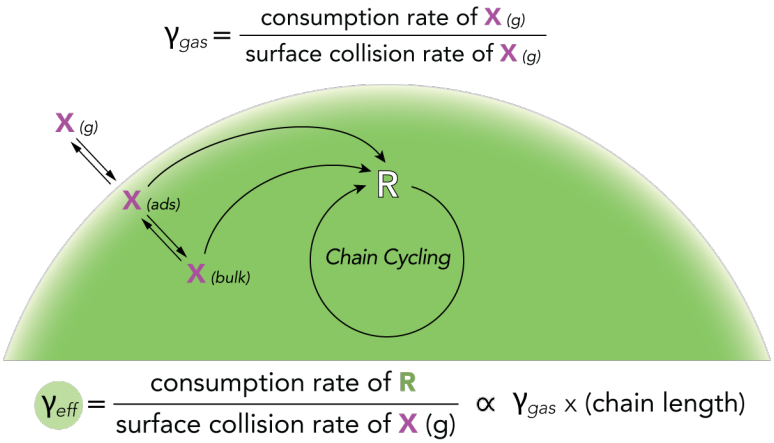

Figure 1.1. Schematic illustrating the effects of chain cycling chemistry on the measurement of γ_{gas} and γ_{eff}.

Since γ_{eff} is measured from the perspective of the condensed phase reactant, it is often not equivalent to the uptake coefficient measured from the gas phase (γ_{gas}, Figure 1.1). For example, in the presence of diffusive limitations, which inhibit reaction, $\gamma_{eff} \ll \gamma_{gas}$, or when secondary reactions in the condensed phase provide additional sinks for reactants, $\gamma_{eff} > \gamma_{gas}$, potentially exceeding unity, such as in the case of radical chain reactions with long chain lengths. γ_{gas}, by contrast, cannot exceed 1 by definition. Thus, γ_{eff} is an emergent property of each reaction system, and through careful measurement and interpretation can be used to interrogate multiple facets of a multiphase reaction mechanism.

In the following sections of this chapter, the versatility of γ_{eff} as an experimental observable will be discussed by examining its role in several studies of model organic aerosols under laboratory conditions (*e.g*, in flow tube reactors). These studies demonstrate how γ_{eff} can report on diffusion coefficients and the timescales of reactant mixing in semisolid aerosol,[12–14]

elucidate competitions between radical propagation and termination mechanisms in chemical reactions,[11,15–17] and help identify new chemical mechanisms involving short-lived reactive intermediates.[18–20] This chapter concludes with a discussion of how information gained from measurements of γ_{eff} can be applied to the chemistry of aerosol particles in the atmosphere and in other systems of interest, as well as an overview of the results that will be presented in the main chapters of this thesis.

1.2 Insights Into the Relative Timescales of Transport and Reaction

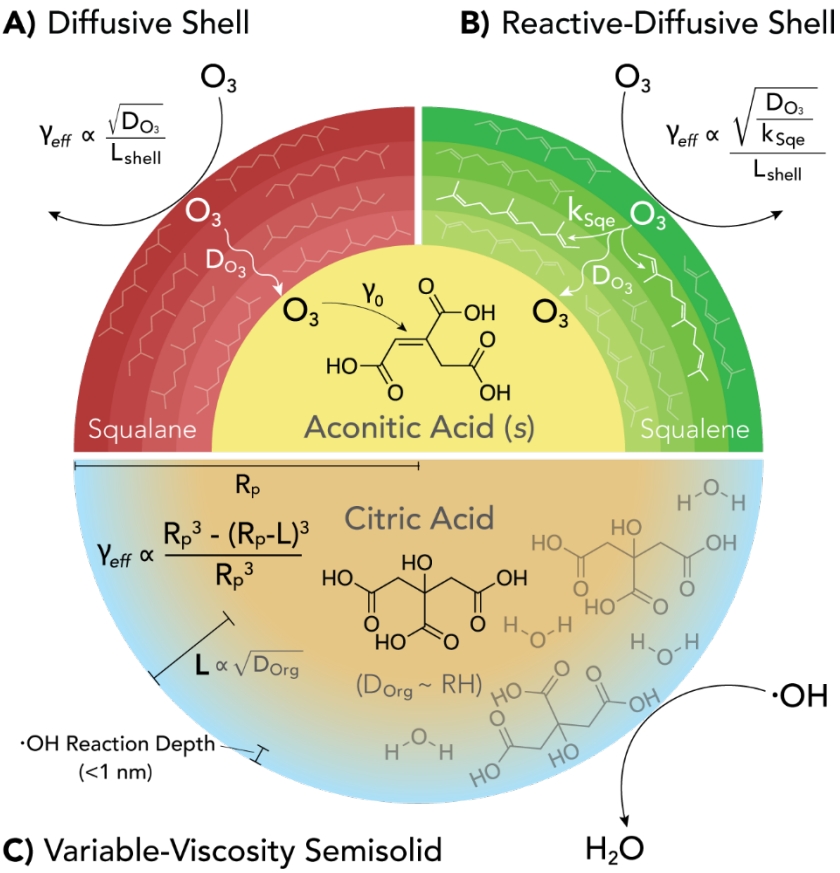

Figure 1.2. Schematic illustrating the relationship between γ_{eff} and reactant transport in ozone reactions with core-shell particles having (a) diffusive and (b) reactive-diffusive organic shells, and (c) in OH radical reactions with citric acid (CA) particles of varying viscosity.

Organic aerosols in the atmosphere can exist in a wide variety of phase states, with particle viscosities ranging from liquid to semisolid (tar-like) to solid,[10,21–23] and recent studies have emphasized how phase state can determine both the transport of gaseous reactants into aerosol particles and the mixing behavior of the particle constituents themselves. Determining the characteristic length- and timescales that govern transport and mixing processes can be experimentally challenging, especially when these processes are inextricably linked with particle-

phase chemical reactions. However, given proper experimental technique, measurements of γ_{eff} can be used to quantify key transport parameters in aerosol particles.

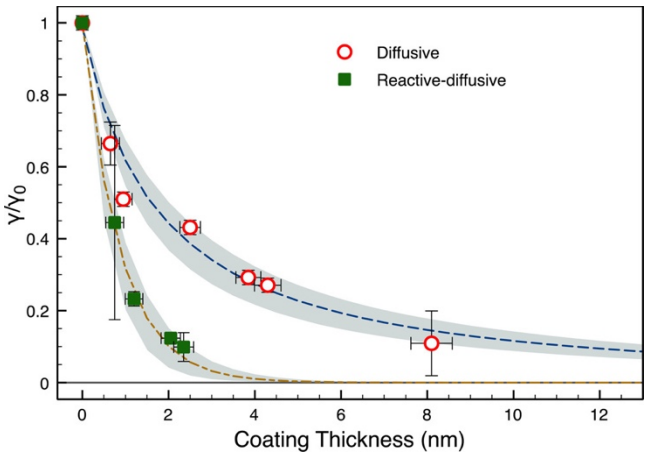

Figure 1.3. The scaling of γ_{eff} with the thickness of purely diffusive and reactive-diffusive shells in model core-shell aerosol upon ozone exposure. Figure used with permission from Lee *et al.*[12]

One such technique was demonstrated by Lee *et al.,*[12] who generated core-shell aerosols with cores of *trans*-aconitic acid (an unsaturated tricarboxylic acid, Figure 1.2) that react with a known rate ($\gamma_{eff} = \gamma_0$) upon exposure to ozone (O_3). The reactive cores were coated with a thin layer of lipid-like, liquid organic, creating a phase-separated shell whose thickness could be determined within ±1 nm by particle size measurements. Depending on whether the shell was composed of a saturated hydrocarbon (Squalane (Sqa), $C_{30}H_{62}$) or an unsaturated hydrocarbon (Squalene (Sqe), $C_{30}H_{50}$), an O_3 molecule colliding with the particle surface would be subject to either diffusion (Figure 1.2A) or both diffusion and reaction (Figure 1.2B) as it transits through the shell, increasing the time required to reach and react with the core. As the shell thickness was increased from 0 up to 12 nm, γ_{eff} for the aconitic acid core was observed to decrease, and the barrier coefficient (the ratio of γ_{eff} to the γ_0 of the uncoated core) was plotted as a function of coating thickness (Figure 1.3).

Since the particle morphology and coating thicknesses were known, each set of barrier coefficients in Figure 1.3 could be fit using a single parameter related to the transport of O_3 through the shell. In the case of aerosol with purely diffusive shells (Figure 1.2A), the decrease in γ_{eff} is directly related to the diffusion coefficient, D_{O_3}, of ozone in Squalane, with a value of D_{O_3} = 1.6x10^{-6} cm^2 s^{-1} estimated by fitting. However, in the case of reactive-diffusive shells (Figure 1.2B), the transit time through the shell additionally depends on the chemical lifetime of O_3 in Squalene, estimated by $\tau_{rxn} = 1/k_{Sqe}[Sqe]_0$. The relative effects of both diffusion and reaction can be expressed as one parameter, the reacto-diffusive length $L_{O_3} = \sqrt{D_{O_3}\tau_{rxn}}$. This length is the average distance an O_3 molecule diffuses in the shell before reacting with an Sqe molecule, with the fitted value of L = 1.03 nm corresponding roughly to the *e*-folding thickness of the barrier coefficient in Figure 1.3. Additionally, by assuming that the value of D_{O_3} is the same for both shell types, the chemical lifetime of O_3 in Sqe was found to be on the order of 7 ns. Thus, by analyzing

how γ_{eff} is modulated, the transport properties of a gaseous reactant could be investigated even when reaction and diffusion are coupled.

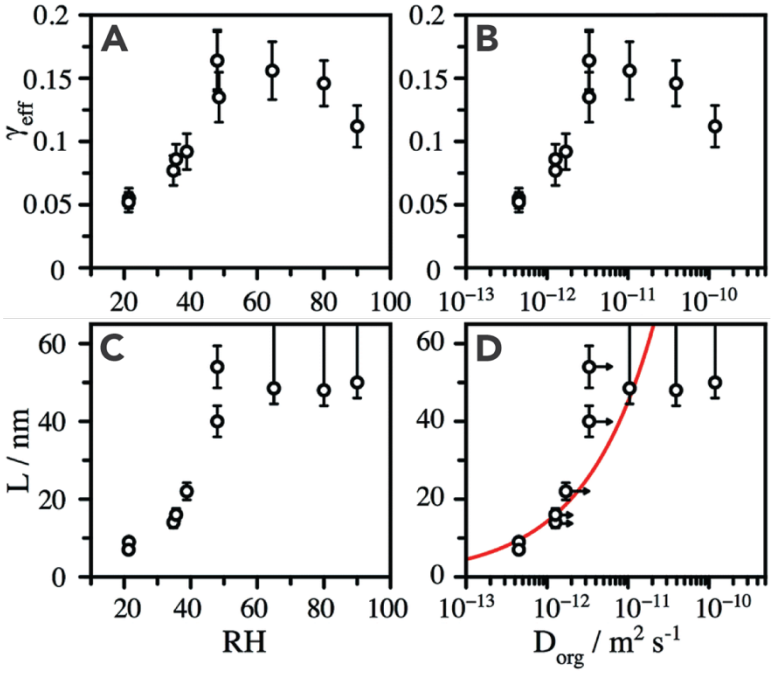

Figure 1.4. Scaling of γ_{eff} (panels A–B) and the accessible depth L (panels C–D) with citric acid + OH radical oxidation (panels A-D). Figure adapted with permission from Davies *et al.*[13]

While this phase-separated system proved useful for controlled experiments, another challenge lies in understanding how reactivity changes when the particle phase state is in a transitional regime, for example beginning in a solid or semi-solid state and becoming more liquid-like.[6,7,13] Davies *et al.* explored such a transition by reacting submicron citric acid (CA) aerosol with gas-phase hydroxyl radicals (OH) in a flow tube reactor (Figure 1.2C).[13] CA is a hygroscopic, amorphous solid whose viscosity depends on the relative humidity (RH): below 50% RH, CA is a diffusion-limited semi-solid, while at 50% RH and above, CA aerosols behave like well-mixed aqueous solutions. From the known viscosity at each RH, a self-diffusion coefficient of CA (D_{org}) can be estimated using the Stokes-Einstein relation.

The decay kinetics of CA upon OH exposure were then monitored using mass spectrometry. γ_{eff} was calculated under each set of conditions, showing an expected dependence on RH (Figure 1.4A), and therefore on D_{org} (Figure 1.4B): below 50% RH, γ_{eff} increases with increasing diffusion rates, reaching an inflection point at 50% RH. Beyond 50% RH, the dilution effect of added water leads to a decrease in uptake. However, the reacto-diffusive length of OH in the CA aerosol yields is calculated to be less than 1 nm over all values of D_{org}, indicating that the reaction takes place primarily at the particle surface. Surface-sensitive measurements supported this conclusion, as the reaction kinetics in the near-surface region appeared well-mixed at all RH values, while whole-particle measurements indicated a fraction of the aerosol remained unreacted below 50% RH.

These results are explained using an accessible-volume model, which relates γ_{eff} to the reaction depth, L (Figure 1.2C), which is the depth of a surface shell of the particle in which the CA appears well-mixed on the timescale of OH reaction. By fitting this model to the observed values of γ_{eff}, values of L can be found as a function of RH (Figure 1.4C). Similar to a reacto-diffusive length, L is roughly proportional to the square root of D_{org} (red line, Figure 1.4D) until L exceeds the particle radius (R_p) and the entire particle is well-mixed and available for reaction. However, instead of the transport of the gas-phase reactant limiting the reaction as with core-shell aerosols, it is the timescale of CA diffusion in the particle phase, which controls its ability to replenish the surface region and therefore controls value of γ_{eff}. These experiments nicely illustrate how γ_{eff} encodes information about the transport timescales of not only incoming gas-phase reactants, but also the subsurface mixing time of particle phase reactants.

In addition to directly modulating the uptake, varying transport times can also have indirect effects on the reactivity in complex reactions. Houle *et al.*[14] conducted detailed reaction-diffusion simulations of the OH oxidation of hydrocarbons under various diffusion limitations and showed that characteristic length scales can exist for individual particle-phase reaction steps. When diffusive limitations restrict the mobility of particle-phase reactants to within these characteristic lengths, changes can occur in the reaction mechanism. While further work is still needed to extend these methods to the complex behavior observed in atmospheric organic aerosol, measurements of γ_{eff} can provide mechanistic insight into how transport and reaction are coupled together across phases.

1.3 Insights into Competing Mechanisms During Radical Reactions

We turn now to a more explicit treatment of the relationship between γ_{eff} and chemistry in the particle phase, where reactions between free radicals and organic molecules often involve complex mechanisms with many competing processes (Scheme 1). After the reaction is initiated by an incoming radical abstracting a hydrogen atom from a C–H bond (Reaction R1), the reaction can either propagate, by forming new radical species that are in turn capable of H-abstraction, or terminate through radical-radical recombination reactions. To understand the behavior of these radical mechanisms under a variety of conditions, one must inquire as to the key steps and species responsible for propagating the radical chain chemistry, as well as the major reactions which compete with each of these steps. Measurements of γ_{eff} are uniquely suited to address these questions since values of $\gamma_{eff} > 1$ are clear signatures of radical chain chemistry. Thus, by examining how γ_{eff} scales with the concentrations of key reactants, crucial mechanistic steps can be inferred.

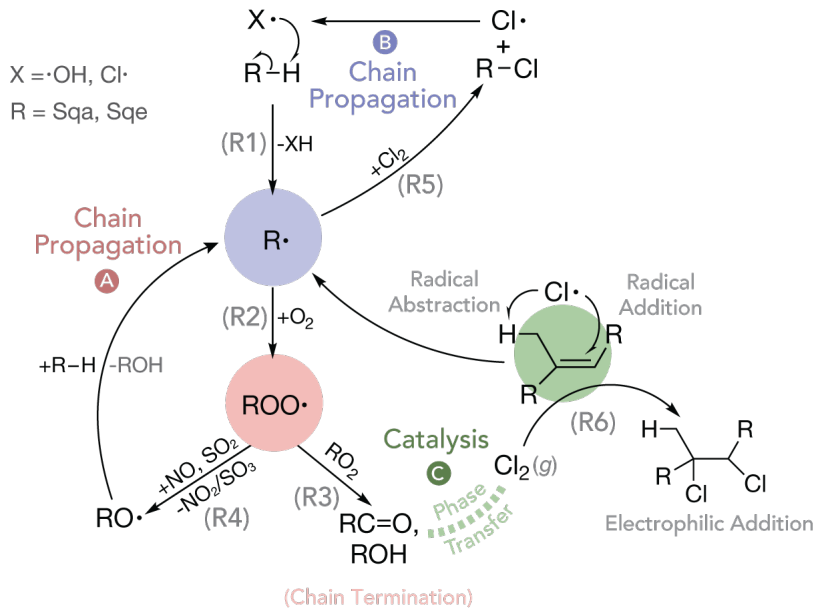

Scheme 1.1. Summary of the radical-initiated reaction pathways discussed in this section. The "resources" at the heart of the key kinetic competition in each example are highlighted and color-coded.

For example, Richards-Henderson *et al.* examined reactions of OH radicals with aerosols composed of alkanes, particularly Sqa.[15,16] Under atmospheric conditions, where molecular oxygen (O_2) is abundant, once an alkyl radical R· is formed (R1) it quickly reacts with O_2 to produce a peroxy radical, (RO_2, reaction R2).[24] Hydrogen abstraction reactions by RO_2 are relatively slow, so under most laboratory conditions (where radical densities are high), recombination reactions are favored (e.g., RO_2 + RO_2). Recombination yields either chain terminating products (aldehydes, ketones, and alcohols—reaction R3), or alkoxy (RO) radicals, which in turn can propagate the reaction.[25–27] In the particle phase, however, the RO-formation channel does not appear as competitive with chain-terminating recombination, so that an OH reaction with an alkane aerosol under pristine conditions does not exhibit chain cycling ($\gamma_{eff} \leq 1$).[28,29]

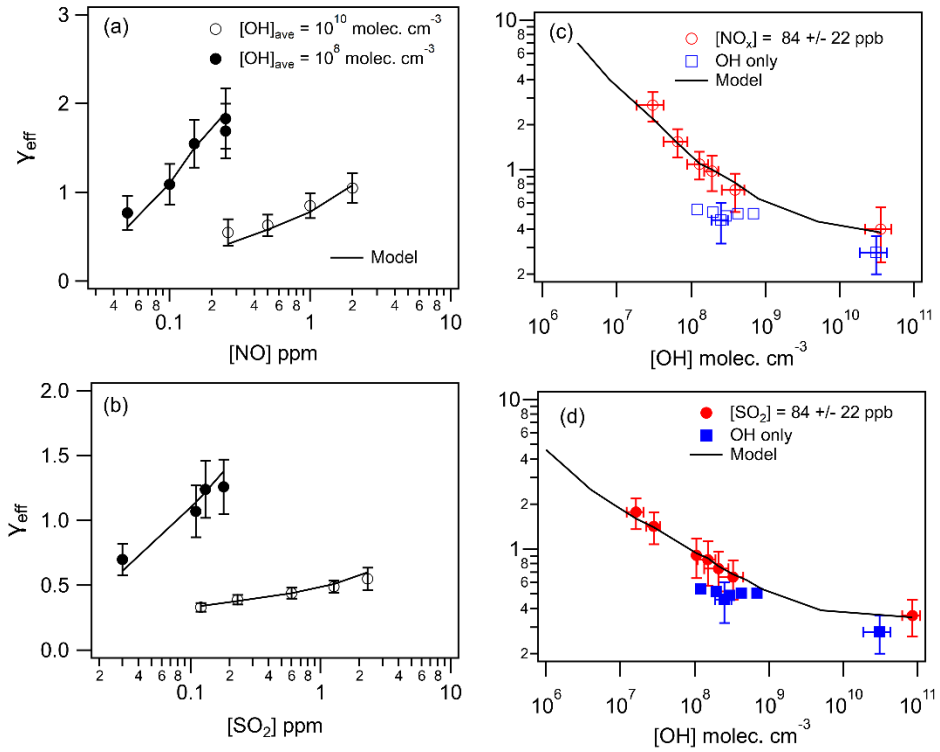

Figure 1.5. Scaling behavior of γ_{eff} during OH radical-initiated oxidation of Squalane in the presence of trace NO (a, c) and SO_2 (b, d). Figures adapted from Richards-Henderson, *et al.*[15,16]

However, when OH radical oxidation is conducted in the presence of NO and SO_2 (Figure 1.5), $\gamma_{eff} > 1$, signaling the onset of radical chain cycling. As seen in Figure 1.5A–B, γ_{eff} scales directly with the concentration of the trace gas, since both NO and SO_2 can undergo oxidation by RO_2 to yield an RO radical (reaction R4, Scheme 1), which propagates the reaction *via* hydrogen abstraction (Label A). Additionally, for each trace gas, γ_{eff} exhibits an inverse dependence on the radical concentration [OH], with increased reaction probabilities at low concentrations. At high [OH], the increased production of RO_2 radicals favors chain termination (R3), since the recombination rate scales as $[RO_2]^2$, effectively out-competing RO formation (R4). Conversely, at low [OH], the reaction between RO_2 and NO/SO_2 dominates the kinetics, leading to RO radicals and subsequent chain cycling. These results demonstrated that, in the presence of SO_2 and NO, the lifetimes of alkanes in atmospheric aerosol could be equivalent to or shorter than the corresponding gas-phase lifetimes. Thus, measurements of γ_{eff} helped identify mechanisms by which particle phase chemistry in polluted conditions could accelerate atmospheric aging.

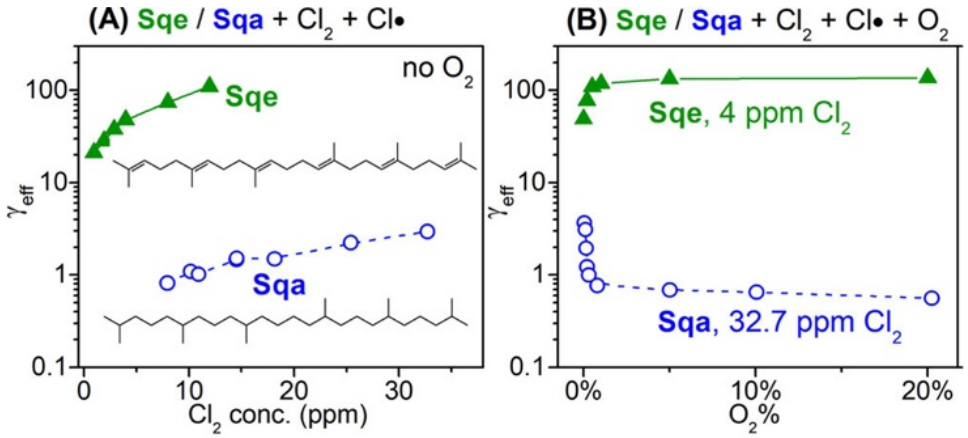

Figure 1.6. Scaling of γ_{eff} with (A) [Cl_2] in the absence of oxygen and (B) [O_2] at constant Cl_2 concentration for the Cl-initiated reaction of Squalane (Sqa) and Squalene (Sqe). Figure adapted with permission from Zeng *et al.*[30]

In addition to OH oxidation, Liu *et al.* studied the reaction of chlorine gas with aerosols of the same saturated hydrocarbon (Sqa).[11] In these experiments, highly reactive chlorine atoms (Cl·) are produced by photolyzing molecular chlorine (Cl_2), and thus both species are present during reaction. As with OH, the reaction is initiated by abstraction of a hydrogen from a C–H bond of Sqa (R1), but in the absence of atmospheric oxygen (O_2), the reaction exhibits $\gamma_{eff} \geq 1$, indicating chain cycling (Figure 1.6A, blue open circles). While Cl_2 is unreactive towards saturated hydrocarbons, increases in Cl_2 concentration lead to an increase in γ_{eff} under these anoxic conditions, as the reaction between Cl_2 and an alkyl radical R· regenerates a Cl· (Reaction R5, Scheme 1) which can initiate hydrogen abstraction and propagate the chain reaction (Label B). By comparing the values of γ_{eff} to the primary uptake coefficient (*ie*, γ_{gas}) inferred from kinetic modeling, it was estimated that an upper bound of 6 Sqa molecules were consumed by secondary reactions for each reactive collision of gas phase Cl·.[11]

When O_2 is reintroduced, however, the chain-propagating step (R5) must compete with the formation of RO_2 radicals (R2).[11] When [O_2] is at atmosphere concentrations (~20%), it is orders of magnitude more abundant than either Cl_2 or Cl· in the experiment, leading to high RO_2 concentrations. Again, since the recombination rate scales as $[RO_2]^2$, this leads to the formation of oxygenated products and termination of the radical chain (R3). Therefore, the presence of O_2 shuts down reaction, giving rise to the inverse relationship of [O_2] and γ_{eff} (Figure 1.6B, blue open circles). Thus, by analyzing the scaling of γ_{eff} with the concentrations of key reactants (O_2 and Cl_2), a rational mechanism for the complex kinetic behavior could be developed.

However, simple changes in the functional groups available for reaction in the condensed phase can lead to unexpected changes in the reaction mechanism and drastic increases in reactivity, as seen in the chlorination of Sqe aerosols studied by Zeng *et al.*[17] The structure of Sqe is nearly identical to that of Sqa, except for 6 alkene functional groups (C=C bonds), which allows electrophilic addition of Cl_2 to the molecule (Reaction R6, Scheme 1). While this reaction is quite slow for pure Sqe aerosols, the presence of particle-phase additives containing oxygenated functional groups enhanced the effective Cl_2 addition rate by 12-23 times over γ_{gas}.[31] While the precise mechanism of this acceleration is under investigation, it was hypothesized that the

oxygenated molecules act as phase transfer catalysts by increasing the Cl_2 residence time at the particle surface.

As a result, when Sqe aerosols were reacted with Cl· in the presence of Cl_2, the combination of Cl_2 electrophilic addition chemistry and the radical cycling mechanism described previously led to an extremely rapid reaction, with γ_{eff} for Sqe (green triangles, Figure 1.6A) that is roughly two orders of magnitude larger than for Sqa. But surprisingly, when $[O_2]$ was increased the reaction was accelerated (green triangles, Figure 1.6B), displaying the opposite the trend in γ_{eff} than that measured previously for Sqa. In addition, the reaction products under high $[O_2]$ were almost entirely chlorinated, not the oxygenated products characteristic of RO_2 recombination and chain termination (R3).

The magnitude of the increase in γ_{eff} therefore eliminates Cl· chain propagation as the source of the accelerated reactivity, as the rate of R5 would not be expected to change so dramatically between Sqa and Sqe. Instead, a catalytic mechanism promoting Cl_2 electrophilic addition chemistry (R6) was proposed.[30] Despite the rapid reaction between Sqe and Cl_2, the radical mechanism described previously is still operative in the presence of high $[O_2]$, leading to RO_2 recombination (R3) and chain termination products. However, these termination products contain the same functional groups as the additives previously observed to catalyze Cl_2 electrophilic addition.[31] Thus, increased $[O_2]$ increases the abundance of these products by generating a Cl_2 phase-transfer catalyst *in situ* in the aerosol (Label C, Scheme 1), which explains the unexpected and dramatic increase of γ_{eff} with $[O_2]$ shown in Figure 1.6B.

As before, investigation of the behavior of γ_{eff} provided insights into a previously unknown process with significant impacts beyond atmospheric chemistry, such as in heterogeneous catalysis. The observation of catalytic behavior during electrophilic addition chemistry raises new questions to be investigated regarding the role of particle interface in controlling these reaction dynamics. The usefulness of γ_{eff} as a probe for discovering novel reaction mechanisms thus extends beyond radical chemistry, as explored further in the following section.

1.4 Insights into Reactive Intermediates in the Condensed Phase

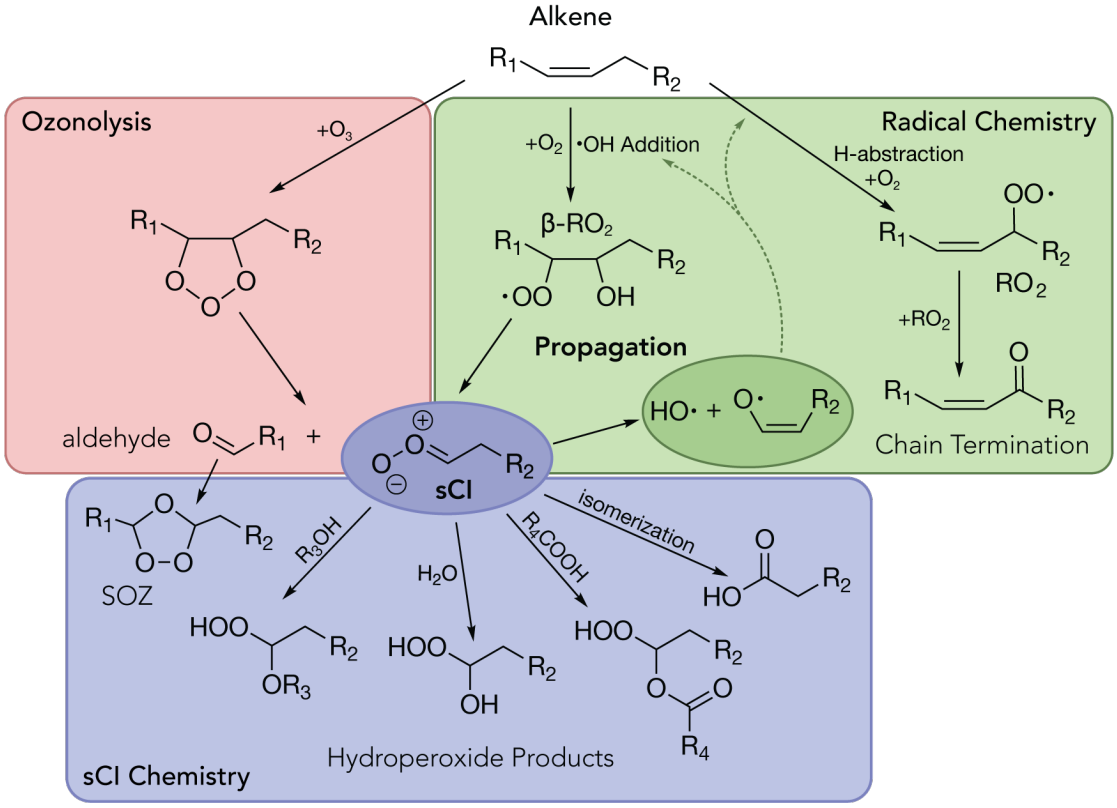

Scheme 1.2. The interconnected reaction pathways of ozone, free radicals, and stabilized Criegee Intermediates (sCI). Figure adapted with permission from Zeng *et al.*[19]

In addition to examining the scaling behavior of γ_{eff} with gas-phase reactants, modifying the structure of particle-phase reactants can also help elucidate complex reaction mechanisms. One example is the peroxidation of unsaturated lipids, which typically proceeds *via* abstraction of a labile allylic hydrogen adjacent to a C=C bond, followed by addition of O_2 to form an unsaturated RO_2 radical (Scheme 2). This species can perform intramolecular hydrogen abstraction from another allylic site, yielding a hydroperoxide (ROOH) and regenerating a R· radical, which propagates the chemistry (known as autoxidation or lipid peroxidation).[32] However, experiments on lipid oxidation have traditionally been performed in the bulk condensed phase using radical initiators, instead of realistic radical species such as OH.[33,32]

To probe this reaction mechanism in aerosols, radical oxidation experiments were again conducted on aerosols of Sqe, a common component of human skin oil, with oxidation initiated by OH.[18] The scaling of γ_{eff} with [OH] shows increased chain cycling at low oxidant concentrations (Figure 1.7). The unsaturated sites play a role in the mechanism, as decreasing the number of C=C bonds in the particle phase reactant from 6 (Sqe) to 1 (*cis*-9-tricosene, Tri) leads to a decrease in γ_{eff}. By contrast, saturated molecules with a single oxygenated functional group all have $\gamma_{eff} < 1$, indicating the absence of chain cycling.

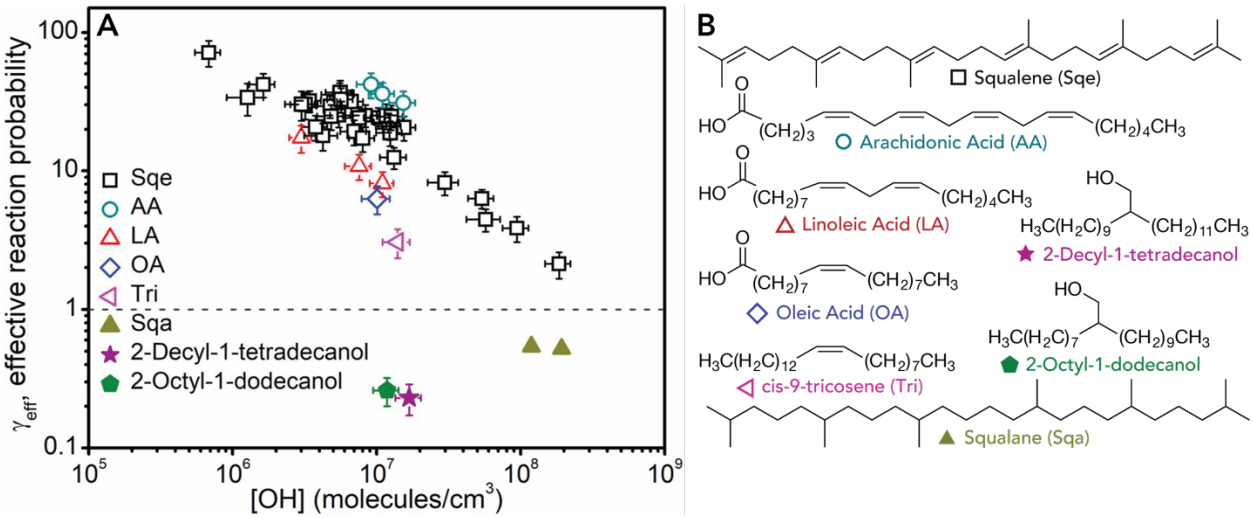

Figure 1.7. (a) Scaling of γ_{eff} with [OH] for various particle-phase organics shown in (b), both unsaturated (Sqe, AA, LA, OA, and Tri) and saturated (Sqa, 2-Decyl-1-tetradecanol, 2-Octyl-1-dodecanol). Figure adapted with permission from Zeng *et al.*[18]

These kinetics could be interpreted as consistent with a typical lipid peroxidation mechanism, however upon analysis, the reaction products were found not to be hydroperoxides (ROOH), but rather secondary ozonides (SOZs), which are typically only observed during ozonolysis (Scheme 2).[34] These species form by reaction between aldehydes and stabilized Criegee Intermediates (sCI, not to be confused with Chlorine/Cl·), which are highly reactive molecules formed during ozonolysis. As first shown by Beauchamp and coworkers,[35] sCIs appear to be formed during radical-initiated oxidation of unsaturated lipids. To test this hypothesis, saturated alcohols, which can act as sCI scavengers, were incorporated into the particle phase with Sqe.[18] The result was the formation of characteristic sCI + alcohol hydroperoxide ether products (Scheme 2), a gradual decrease in the γ_{eff} of Sqe as alcohol was added, and a drastic enhancement in the the γ_{eff} of the alcohol above its value in pure droplets (Figure 1.8A). These results imply that sCIs are not only generated during OH oxidation, but are in fact the species responsible for its chain propagation, as sCIs can regenerate OH radicals *via* unimolecular decomposition channels.

The precise mechanism by which sCIs are produced remains under investigation, though several mechanisms have been proposed[18,35–37] each involving the β-hydroxy peroxy radical (β-RO_2) formed after OH addition to the alkene (Scheme 2). A recent modeling study of the OH oxidation of Sqe evaluated the kinetic viability of 3 possible mechanisms,[38] but further combined theoretical and experimental efforts are needed to establish a comprehensive description of this step.

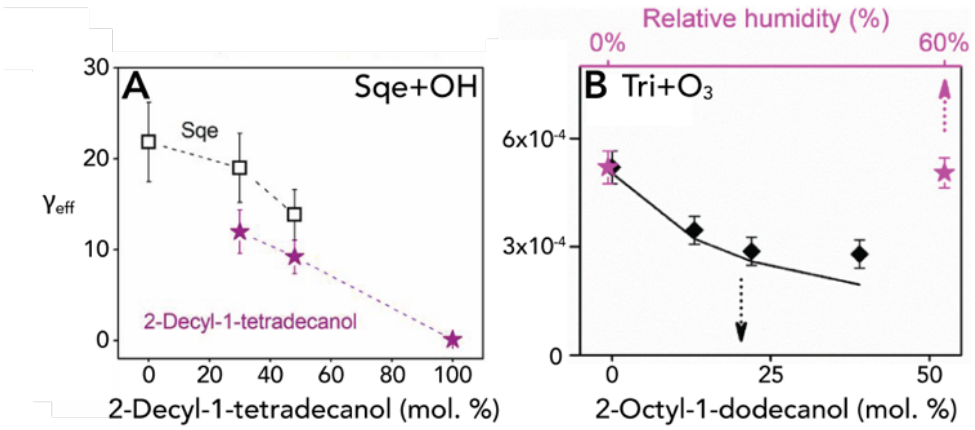

Figure 1.8. Scaling of γ_{eff} with the concentration of sCI scavenger (saturated alcohol) in the condensed phase during (a) OH-radical initiated Sqe oxidation and (b) ozonolysis of Tri aerosol. The value of γ_{eff} is corrected for the mole fraction of the reactant in these mixture experiments to account for dilution effects. Figures adapted with permission from Zeng *et al.*[18] and Zeng and Wilson.[19]

Regardless of the specific mechanism by which they are generated, sCIs have been shown to constitute a new link between two typically distinct chemical mechanisms, namely secondary chemistry resulting from ozonolysis and OH-initiated radical oxidation (Scheme 2). As a result, radical chain cycling can be initiated by ozonolysis in addition to OH oxidation, as further explored by Zeng *et al.* using *cis*-9-tricosene (Tri) aerosols.[19] Tri has a single C=C bond, which simplifies the reaction mechanism and potential products of ozonolysis, and it has no oxygenated functional groups, which act as sCI scavengers. Additionally, the aldehydes formed from ozonolysis of Tri are volatile and preferentially evaporate from the particle, removing another potential sink of the CI in the particle phase. These properties make Tri an excellent candidate for observing CI-propagated chain cycling.

During ozonolysis, the γ_{eff} of Tri during was measured to be 5.2×10^{-4}, which is an order of magnitude larger than previous measurements of $\gamma_{gas,O3}$.[39] Even though the γ_{eff} is less than 1, substantial chain cycling can still be inferred by comparison of these two measurements. Incorporating a particle-phase saturated alcohol, which is unreactive toward O_3, resulted in the decrease of γ_{eff} (Figure 1.8B), as was observed for the OH + Sqe reaction (Figure 1.8A). In addition, a decrease in the radical chain termination products of Tri (Scheme 2) was observed in the presence of the alcohol. Surprisingly, kinetic modeling suggests that radical chain cycling is the dominant oxidation pathway for Tri during ozonolysis, accounting for nearly 70% of the reactivity.[19] Thus, this pathway could be kinetically quite significant during ozonolysis chemistry.

However, assessing the significance of this radical chain cycling to atmospheric aerosol aging requires knowledge of the precise rate constants of reactions between sCIs and the various functional groups, such as carboxylic acids, that might be present in these environments.[40] In particular, gas-phase measurements of reactions between small sCIs and carboxylic acids yield a rate constant (k_{acid}) with values at or exceeding the limit for collision-controlled processes,[41,42] but the applicability of this rate to particle-phase sCI is in need of evaluation.

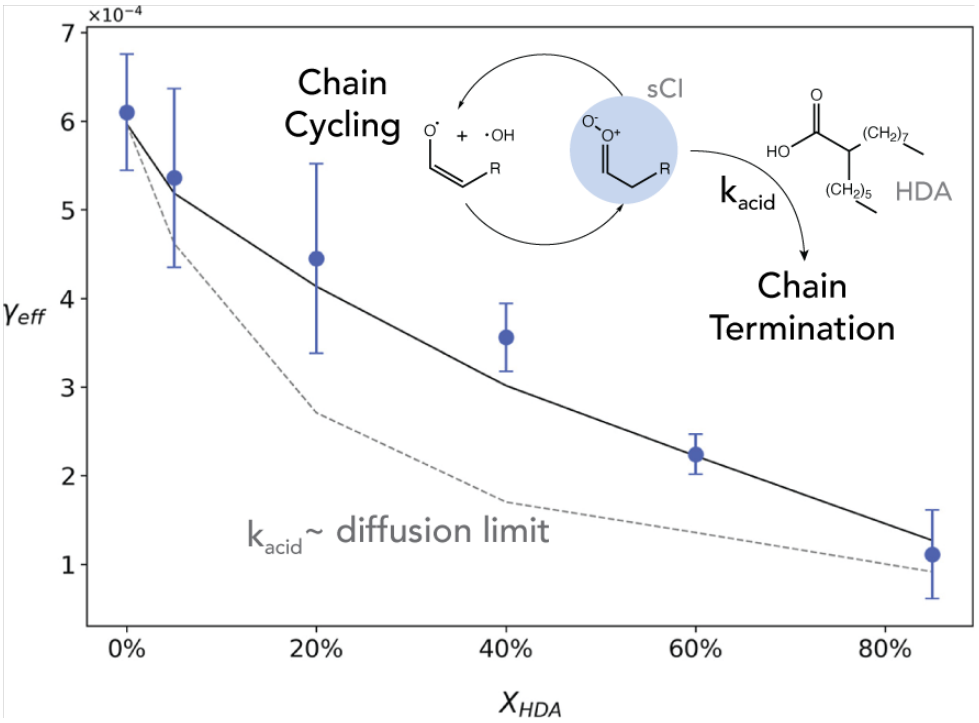

Figure 1.9. Scaling of γ_{eff} for Tri during ozonolysis as a function of mole fraction of acid sCI scavenger (HDA). Lines correspond to model predictions with differing values of k_{acid}: a slower rate competitive with unimolecular processes (solid line) and the diffusion-limited rate analogous to the collision limit in the gas phase (dashed line). Figure adapted with permission from Reynolds *et al.*[20]

Building on previous ozonolysis studies with Tri, an experimental approach involving aerosol mixtures allows the value of k_{acid} in the particle phase to be constrained, as discussed in Chapter 2 of this thesis.[20] Varying amounts of a saturated liquid carboxylic acid, 2-hexyldecanoic acid (HDA), are incorporated into Tri aerosols undergoing ozonolysis where, similar to the behavior with saturated alcohols, the γ_{eff} of Tri decreased. Since HDA is unreactive toward O_3, any decay of HDA observed during ozonolysis is attributable to sCI chemistry, primarily resulting in a hydroperoxide ester product (Scheme 2). These decay kinetics can be explained in terms of a simple model of the competition between bimolecular reaction of sCIs with HDA, which is chain-terminating, and the unimolecular decomposition reactions of sCIs to initiate radical chemistry, as shown in Figure 1.9.[20] By fitting this model to the HDA decay profiles observed during Tri ozonolysis, a relative ratio of these rate constants could be obtained. However, measurements of γ_{eff} also constrain the value of the rate constant k_{acid} in kinetic simulations. If the sCI + HDA reaction is extremely fast, it would be expected to proceed at the diffusion limit in the condensed phase, but simulations corresponding to this rate shut off the radical chain cycling too quickly. This leads to a rapid falloff in γ_{eff} with HDA concentration (dashed line, Figure 1.9) that is inconsistent with experimental observations. Thus, an upper bound can be established on k_{acid}, suggesting a more reasonable rate that keeps this reaction channel competitive with the unimolecular reactions of sCIs.

Through careful experimental design, including changes to the particle-phase composition and molecular structure of the reactants, measurements of γ_{eff} can be used to establish new links between different branches of oxidation chemistry. Applications of this approach thus extend beyond their typical application to heterogeneous reactions on atmospheric aerosols and into research fields such as oxidative stress in biological systems or the design of antioxidants for reducing food spoilage.[18]

1.5 Summary and Outlook

Studies designed around the measurement and interpretation of γ_{eff} have the potential to help explain the complex behavior of chemical systems controlled by reaction and diffusion, as demonstrated by the examples discussed in this chapter. By examining the relationship between γ_{eff} and reactant transport parameters, insight is gained into the effects of diffusion limitations on heterogeneous oxidation. By examining the relationship between γ_{eff} and various gas-phase reactants, the mechanisms of radical reactions can be determined. And by measuring γ_{eff} while selectively modifying the constituents of the particle phase, new links between disparate reaction mechanisms can be uncovered.

In the chapters that follow, measurements of γ_{eff} in aerosol flow tube reactors are used to reveal the reaction rates and temperature-dependent behavior of sCI formed by ozonolysis. In Chapter 2, the content of which was discussed briefly in Section 1.4, room temperature flow tube measurements of ozonolysis of Tri aerosols mixed with particle-phase HDA are used to quantify the reaction rate between sCI and long-chain carboxylic acids. This rate is found to be six orders of magnitude slower than the corresponding gas-phase reaction rate, raising questions about the mechanism of this reaction in the particle phase. In Chapter 3, a follow-up study is conducted on the temperature-dependence of this reaction to investigate the energetics of its key reaction steps. Chain cycling driven by the sCI is found to increase at low temperatures (263 K), due to the effects of increased ozone solubility and decreased unimolecular reaction rates on particle-phase sCI concentrations. Measurements of the decay of HDA during ozonolysis at low temperatures indicate an activation barrier of at least 40 kJ mol^{-1} for the particle-phase sCI + carboxylic acid reaction.

In Chapter 4, attention shifts from Criegee Intermediates to reactive intermediates relevant to synthetic chemistry, namely those produced by cerium organometallic photocatalysts. Progress is described toward an aerosol delivery system for these lanthanide photocatalysts, which have the potential to perform chemoselective redox chemistry on target molecules for organic synthesis. An apparatus for generating and detecting aerosol containing a Ce (IV) catalyst and target reactants in submicron (~100 nm diameter) organic solvent droplets is developed, and particle-phase Ce-ligand complexes are detected via nanospray ionization (NSI) mass spectrometry. The structures of these complexes in the presence of two different carboxylic acid ligands are discussed and identified as primarily 4-coordinate complexes with 1 or 2 Ce metal centers. These results have implications for the design of future catalysts and experiments that will make use of the particle surface to increase catalytic efficiency. Finally, in Chapter 5, the discussion concludes with a brief summary of the key findings presented in this thesis, and a brief comment about the themes that unite these distinct research efforts.

1.6 References

(1) Finlayson-Pitts, B. J.; Pitts, J. N. *Chemistry of the Upper and Lower Atmosphere: Theory, Experiments, and Applications*; Academic Press: San Diego, 2000.

(2) Seinfeld, J. H.; Pandis, S. N. *Atmospheric Chemistry and Physics: From Air Pollution to Climate Change*, Third edition.; Wiley: Hoboken, New Jersey, 2016.

(3) Worsnop, D. R.; Zahniser, M. S.; Kolb, C. E.; Gardner, J. A.; Watson, L. R.; Van Doren, J. M.; Jayne, J. T.; Davidovits, P. The Temperature Dependence of Mass Accommodation of Sulfur Dioxide and Hydrogen Peroxide on Aqueous Surfaces. *J. Phys. Chem.* **1989**, *93* (3), 1159–1172. https://doi.org/10.1021/j100340a027.

(4) Davidovits, P.; Kolb, C. E.; Williams, L. R.; Jayne, J. T.; Worsnop, D. R. Mass Accommodation and Chemical Reactions at Gas−Liquid Interfaces. 32.

(5) Kolb, C. E.; Cox, R. A.; Abbatt, J. P. D.; Ammann, M.; Davis, E. J.; Donaldson, D. J.; Garrett, B. C.; George, C.; Griffiths, P. T.; Hanson, D. R.; Kulmala, M.; McFiggans, G.; Pöschl, U.; Riipinen, I.; Rossi, M. J.; Rudich, Y.; Wagner, P. E.; Winkler, P. M.; Worsnop, D. R.; O' Dowd, C. D. An Overview of Current Issues in the Uptake of Atmospheric Trace Gases by Aerosols and Clouds. *Atmos. Chem. Phys.* **2010**, *10* (21), 10561–10605. https://doi.org/10.5194/acp-10-10561-2010.

(6) Berkemeier, T.; Huisman, A. J.; Ammann, M.; Shiraiwa, M.; Koop, T.; Pöschl, U. Kinetic Regimes and Limiting Cases of Gas Uptake and Heterogeneous Reactions in Atmospheric Aerosols and Clouds: A General Classification Scheme. *Atmos. Chem. Phys.* **2013**, *13* (14), 6663–6686. https://doi.org/10.5194/acp-13-6663-2013.

(7) Steimer, S. S.; Berkemeier, T.; Gilgen, A.; Krieger, U. K.; Peter, T.; Shiraiwa, M.; Ammann, M. Shikimic Acid Ozonolysis Kinetics of the Transition from Liquid Aqueous Solution to Highly Viscous Glass. *Phys. Chem. Chem. Phys.* **2015**, *17* (46), 31101–31109. https://doi.org/10.1039/C5CP04544D.

(8) Jimenez, J. L.; Canagaratna, M. R.; Donahue, N. M.; Prevot, A. S. H.; Zhang, Q.; Kroll, J. H.; DeCarlo, P. F.; Allan, J. D.; Coe, H.; Ng, N. L.; Aiken, A. C.; Docherty, K. S.; Ulbrich, I. M.; Grieshop, A. P.; Robinson, A. L.; Duplissy, J.; Smith, J. D.; Wilson, K. R.; Lanz, V. A.; Hueglin, C.; Sun, Y. L.; Tian, J.; Laaksonen, A.; Raatikainen, T.; Rautiainen, J.; Vaattovaara, P.; Ehn, M.; Kulmala, M.; Tomlinson, J. M.; Collins, D. R.; Cubison, M. J.; E; Dunlea, J.; Huffman, J. A.; Onasch, T. B.; Alfarra, M. R.; Williams, P. I.; Bower, K.; Kondo, Y.; Schneider, J.; Drewnick, F.; Borrmann, S.; Weimer, S.; Demerjian, K.; Salcedo, D.; Cottrell, L.; Griffin, R.; Takami, A.; Miyoshi, T.; Hatakeyama, S.; Shimono, A.; Sun, J. Y.; Zhang, Y. M.; Dzepina, K.; Kimmel, J. R.; Sueper, D.; Jayne, J. T.; Herndon, S. C.; Trimborn, A. M.; Williams, L. R.; Wood, E. C.; Middlebrook, A. M.; Kolb, C. E.; Baltensperger, U.; Worsnop, D. R. Evolution of Organic Aerosols in the Atmosphere. *Science* **2009**, *326* (5959), 1525–1529. https://doi.org/10.1126/science.1180353.

(9) Shiraiwa, M.; Ammann, M.; Koop, T.; Pöschl, U. Gas Uptake and Chemical Aging of Semisolid Organic Aerosol Particles. *PNAS* **2011**, *108* (27), 11003–11008. https://doi.org/10.1073/pnas.1103045108.

(10) Koop, T.; Bookhold, J.; Shiraiwa, M.; Pöschl, U. Glass Transition and Phase State of Organic Compounds: Dependency on Molecular Properties and Implications for Secondary Organic Aerosols in the Atmosphere. *Phys. Chem. Chem. Phys.* **2011**, *13* (43), 19238–19255. https://doi.org/10.1039/C1CP22617G.

(11) Liu, C.-L.; Smith, J. D.; Che, D. L.; Ahmed, M.; Leone, S. R.; Wilson, K. R. The Direct Observation of Secondary Radical Chain Chemistry in the Heterogeneous Reaction of Chlorine Atoms with Submicron Squalane Droplets. *Phys. Chem. Chem. Phys.* **2011**, *13* (19), 8993. https://doi.org/10.1039/c1cp20236g.

(12) Lee, L.; Wilson, K. The Reactive–Diffusive Length of OH and Ozone in Model Organic Aerosols. *J. Phys. Chem. A* **2016**, *120* (34), 6800–6812. https://doi.org/10.1021/acs.jpca.6b05285.

(13) Davies, J. F.; Wilson, K. R. Nanoscale Interfacial Gradients Formed by the Reactive Uptake of OH Radicals onto Viscous Aerosol Surfaces. *Chem. Sci.* **2015**, *6* (12), 7020–7027. https://doi.org/10.1039/C5SC02326B.

(14) Houle, F. A.; Wiegel, A. A.; Wilson, K. R. Changes in Reactivity as Chemistry Becomes Confined to an Interface. The Case of Free Radical Oxidation of $C_{30}H_{62}$ Alkane by OH. *J. Phys. Chem. Lett.* **2018**, *9* (5), 1053–1057. https://doi.org/10.1021/acs.jpclett.8b00172.

(15) Richards-Henderson, N. K.; Goldstein, A. H.; Wilson, K. R. Large Enhancement in the Heterogeneous Oxidation Rate of Organic Aerosols by Hydroxyl Radicals in the Presence of Nitric Oxide. *J. Phys. Chem. Lett.* **2015**, *6* (22), 4451–4455. https://doi.org/10.1021/acs.jpclett.5b02121.

(16) Richards-Henderson, N. K.; Goldstein, A. H.; Wilson, K. R. Sulfur Dioxide Accelerates the Heterogeneous Oxidation Rate of Organic Aerosol by Hydroxyl Radicals. *Environ. Sci. Technol.* **2016**, *50* (7), 3554–3561. https://doi.org/10.1021/acs.est.5b05369.

(17) Zeng, M.; Liu, C.-L.; Wilson, K. R. Catalytic Coupling of Free Radical Oxidation and Electrophilic Chlorine Addition by Phase-Transfer Intermediates in Liquid Aerosols. *J. Phys. Chem. A* **2022**, *126* (19), 2959–2965. https://doi.org/10.1021/acs.jpca.2c00291.

(18) Zeng, M.; Heine, N.; Wilson, K. R. Evidence That Criegee Intermediates Drive Autoxidation in Unsaturated Lipids. *PNAS* **2020**. https://doi.org/10.1073/pnas.1920765117.

(19) Zeng, M.; Wilson, K. R. Efficient Coupling of Reaction Pathways of Criegee Intermediates and Free Radicals in the Heterogeneous Ozonolysis of Alkenes. *J. Phys. Chem. Lett.* **2020**, *11* (16), 6580–6585. https://doi.org/10.1021/acs.jpclett.0c01823.

(20) Reynolds, R.; Ahmed, M.; Wilson, K. R. Constraining the Reaction Rate of Criegee Intermediates with Carboxylic Acids during the Multiphase Ozonolysis of Aerosolized Alkenes. *ACS Earth Space Chem.* **2023**. https://doi.org/10.1021/acsearthspacechem.3c00026.

(21) Reid, J. P.; Bertram, A. K.; Topping, D. O.; Laskin, A.; Martin, S. T.; Petters, M. D.; Pope, F. D.; Rovelli, G. The Viscosity of Atmospherically Relevant Organic Particles. *Nature Communications* **2018**, *9* (1), 1–14. https://doi.org/10.1038/s41467-018-03027-z.

(22) Slade, J. H.; Knopf, D. A. Multiphase OH Oxidation Kinetics of Organic Aerosol: The Role of Particle Phase State and Relative Humidity. *Geophysical Research Letters* **2014**, *41* (14), 5297–5306. https://doi.org/10.1002/2014GL060582.

(23) Slade, J. H.; Ault, A. P.; Bui, A. T.; Ditto, J. C.; Lei, Z.; Bondy, A. L.; Olson, N. E.; Cook, R. D.; Desrochers, S. J.; Harvey, R. M.; Erickson, M. H.; Wallace, H. W.; Alvarez, S. L.; Flynn, J. H.; Boor, B. E.; Petrucci, G. A.; Gentner, D. R.; Griffin, R. J.; Shepson, P. B. Bouncier Particles at Night: Biogenic Secondary Organic Aerosol Chemistry and Sulfate Drive Diel Variations in the Aerosol Phase in a Mixed Forest. *Environ. Sci. Technol.* **2019**, *53* (9), 4977–4987. https://doi.org/10.1021/acs.est.8b07319.

(24) Denisov, E. T.; Afanas'ev, I. B. *Oxidation and Antioxidants in Organic Chemistry and Biology.*; Taylor & Frances: Oxford, 2005.

(25) Russell, G. A. Deuterium-Isotope Effects in the Autoxidation of Aralkyl Hydrocarbons. Mechanism of the Interaction of PEroxy Radicals1. *J. Am. Chem. Soc.* **1957**, *79* (14), 3871–3877. https://doi.org/10.1021/ja01571a068.

(26) Howard, J. A.; Ingold, K. U. Self-Reaction of Sec-Butylperoxy Radicals. Confirmation of the Russell Mechanism. *J. Am. Chem. Soc.* **1968**, *90* (4), 1056–1058. https://doi.org/10.1021/ja01006a037.

(27) Bennett, J. E.; Summers, R. Product Studies of the Mutual Termination Reactions of *Sec* -Alkylperoxy Radicals: Evidence for Non-Cyclic Termination. *Can. J. Chem.* **1974**, *52* (8), 1377–1379. https://doi.org/10.1139/v74-209.

(28) Docherty, K. S.; Ziemann, P. J. Reaction of Oleic Acid Particles with NO_3 Radicals: Products, Mechanism, and Implications for Radical-Initiated Organic Aerosol Oxidation. *J. Phys. Chem. A* **2006**, *110* (10), 3567–3577. https://doi.org/10.1021/jp0582383.

(29) George, I. J.; Abbatt, J. P. D. Heterogeneous Oxidation of Atmospheric Aerosol Particles by Gas-Phase Radicals. *Nature Chem* **2010**, *2* (9), 713–722. https://doi.org/10.1038/nchem.806.

(30) Zeng, M.; Liu, C.-L.; Wilson, K. R. Catalytic Coupling of Free Radical Oxidation and Electrophilic Chlorine Addition by Phase-Transfer Intermediates in Liquid Aerosols. *J. Phys. Chem. A* **2022**, *126* (19), 2959–2965. https://doi.org/10.1021/acs.jpca.2c00291.

(31) Zeng, M.; Wilson, K. R. Experimental Evidence That Halogen Bonding Catalyzes the Heterogeneous Chlorination of Alkenes in Submicron Liquid Droplets. *Chem. Sci.* **2021**, *12* (31), 10455–10466. https://doi.org/10.1039/D1SC02662C.

(32) Yin, H.; Xu, L.; Porter, N. A. Free Radical Lipid Peroxidation: Mechanisms and Analysis. *Chem. Rev.* **2011**, *111* (10), 5944–5972. https://doi.org/10.1021/cr200084z.

(33) Niki, E. Free Radical Initiators as Source of Water- or Lipid-Soluble Peroxyl Radicals. In *Methods in Enzymology*; Elsevier, 1990; Vol. 186, pp 100–108. https://doi.org/10.1016/0076-6879(90)86095-D.

(34) Heine, N.; Houle, F. A.; Wilson, K. R. Connecting the Elementary Reaction Pathways of Criegee Intermediates to the Chemical Erosion of Squalene Interfaces during Ozonolysis. *Environ. Sci. Technol.* **2017**, *51* (23), 13740–13748. https://doi.org/10.1021/acs.est.7b04197.

(35) Zhang, X.; Barraza, K. M.; Beauchamp, J. L. Cholesterol Provides Nonsacrificial Protection of Membrane Lipids from Chemical Damage at Air–Water Interface. *PNAS* **2018**, *115* (13), 3255–3260. https://doi.org/10.1073/pnas.1722323115.

(36) Wagner, J. P. Criegee Intermediates in Autoxidation Reactions: Mechanistic Considerations. *J. Phys. Chem. A* **2021**, *125* (1), 406–410. https://doi.org/10.1021/acs.jpca.0c09971.

(37) Chen, L.; Huang, Y.; Xue, Y.; Jia, Z. Molecular Insights into the Formation of Criegee Intermediates from β-Hydroxyperoxy Radicals. *Atmospheric Environment* **2024**, *338*, 120828. https://doi.org/10.1016/j.atmosenv.2024.120828.

(38) Zeng, M.; Wilson, K. R. Evaluating Possible Formation Mechanisms of Criegee Intermediates during the Heterogeneous Autoxidation of Squalene. *Environ. Sci. Technol.* **2024**, *58* (26), 11587–11595. https://doi.org/10.1021/acs.est.4c02590.

(39) Wells, J. R.; Morrison, G. C.; Coleman, B. K.; Spicer, C.; Dean, S. W. Kinetics and Reaction Products of Ozone and Surface-Bound Squalene. *J. ASTM Int.* **2008**, *5* (7), 101629. https://doi.org/10.1520/JAI101629.

(40) Berkemeier, T.; Mishra, A.; Mattei, C.; Huisman, A. J.; Krieger, U. K.; Pöschl, U. Ozonolysis of Oleic Acid Aerosol Revisited: Multiphase Chemical Kinetics and Reaction Mechanisms. *ACS Earth Space Chem.* **2021**, *5* (12), 3313–3323. https://doi.org/10.1021/acsearthspacechem.1c00232.

(41) Taatjes, C. A. Criegee Intermediates: What Direct Production and Detection Can Teach Us About Reactions of Carbonyl Oxides. *Annu. Rev. Phys. Chem.* **2017**, *68* (1), 183–207. https://doi.org/10.1146/annurev-physchem-052516-050739.

(42) Welz, O.; Eskola, A. J.; Sheps, L.; Rotavera, B.; Savee, J. D.; Scheer, A. M.; Osborn, D. L.; Lowe, D.; Murray Booth, A.; Xiao, P.; Anwar H. Khan, M.; Percival, C. J.; Shallcross, D. E.; Taatjes, C. A. Rate Coefficients of C1 and C2 Criegee Intermediate Reactions with Formic and Acetic Acid Near the Collision Limit: Direct Kinetics Measurements and Atmospheric Implications. *Angewandte Chemie* **2014**, *126* (18), 4635–4638. https://doi.org/10.1002/ange.201400964.

Chapter 2. The Reaction Rate of Criegee Intermediates and Carboxylic Acids During Multiphase Ozonolysis

2.1 Introduction

Criegee Intermediates (carbonyl oxides), formed during the ozonolysis of unsaturated organic compounds (Scheme 2.1), are crucially important oxidants due to their high reactivity and diverse reaction pathways.[1] Extensive gas-phase studies have been conducted on these short-lived intermediates to understand their chemistry, which has been enabled by direct detection of these species in recent years.[2,3] The reaction between a Criegee Intermediate and an organic acid is observed to occur near or exceeding the calculated hard-sphere collision limit in direct measurements.[4,5] As a result, this reaction pathway is thought to represent a significant sink of Criegee Intermediates in the atmosphere. Additionally, the oligomeric hydroperoxide products of this reaction are thought to contribute to atmospheric particle formation.[4]

In condensed phases where both unsaturated organics and saturated carboxylic acids (RCOOH) are present, the loss of RCOOH[6] and subsequent formation of α-acyloxyalkyl hydroperoxides (AAHPs)[7] has been observed during ozonolysis. With analogy to the gas phase mechanism, this reaction is attributed to Criegee Intermediates in the organic matrix which have been stabilized by thermalizing collisions. (These stabilized Criegee Intermediates will furthermore be referred to simply as sCI.) The sCI + RCOOH reaction is significant to the ozonolysis of aerosol composed of unsaturated fatty acids, such as oleic acid, where peroxidic products are estimated to account for between 30–68% of the product yield.[8,9] However, the kinetics of this sCI consumption channel are underdetermined in the condensed phase, which has resulted in significant uncertainty in models of heterogeneous ozonolysis in organic aerosol, where rate constants for the sCI + RCOOH reaction vary over six orders of magnitude.[10,11] Thus, measurements of this rate coefficient would improve the prediction of reaction kinetics and product distributions in models of heterogeneous chemistry.

In this study, a flow tube reactor is used to investigate the heterogeneous ozonolysis of aerosols of a mixture of a model alkene, cis-9-tricosene (**Tri**, $C_{23}H_{46}$ — MW 322), and a saturated organic acid, 2-hexyldecanoic acid (**HDA**, $C_{16}H_{32}O_2$ — MW 256). This mixture is used to constrain the rate of reaction between particle-bound sCI and organic acid functional groups. Tri is a suitable model alkene for this purpose as it contains a single double bond, is a liquid at room temperature, and contains no oxygenated functional groups. The aldehydes produced from ozonolysis of Tri (Scheme 2.1A) are volatile and largely partition out of the aerosol during reaction, thus restricting the number of secondary reaction channels available to the sCI.[12,13] Additionally, the decay rate of Tri during ozonolysis is highly sensitive to additives that behave as sCI scavengers, as a result of radical chain oxidation chemistry.[12] HDA is a suitable model for fatty acid functionality (RCOOH), as its saturated chain is unreactive to both O_3 and sCI, thereby restricting its chemical reactivity to its acid head group. By measuring the decay kinetics of both Tri and HDA upon exposure to ozone, the production rate of sCI, the consumption of sCI by a

condensed-phase organic acid, and the interaction between the sCI + RCOOH and radical chain cycling reactions are probed simultaneously. A simple kinetic model is used to analyze these observations and shows that the kinetic observations can be explained by the competition between bimolecular and unimolecular sinks for sCI, allowing for estimation of the sCI + RCOOH rate constant. This result is validated using explicit kinetic simulations, which incorporate a detailed mechanism derived from previous work.[12]

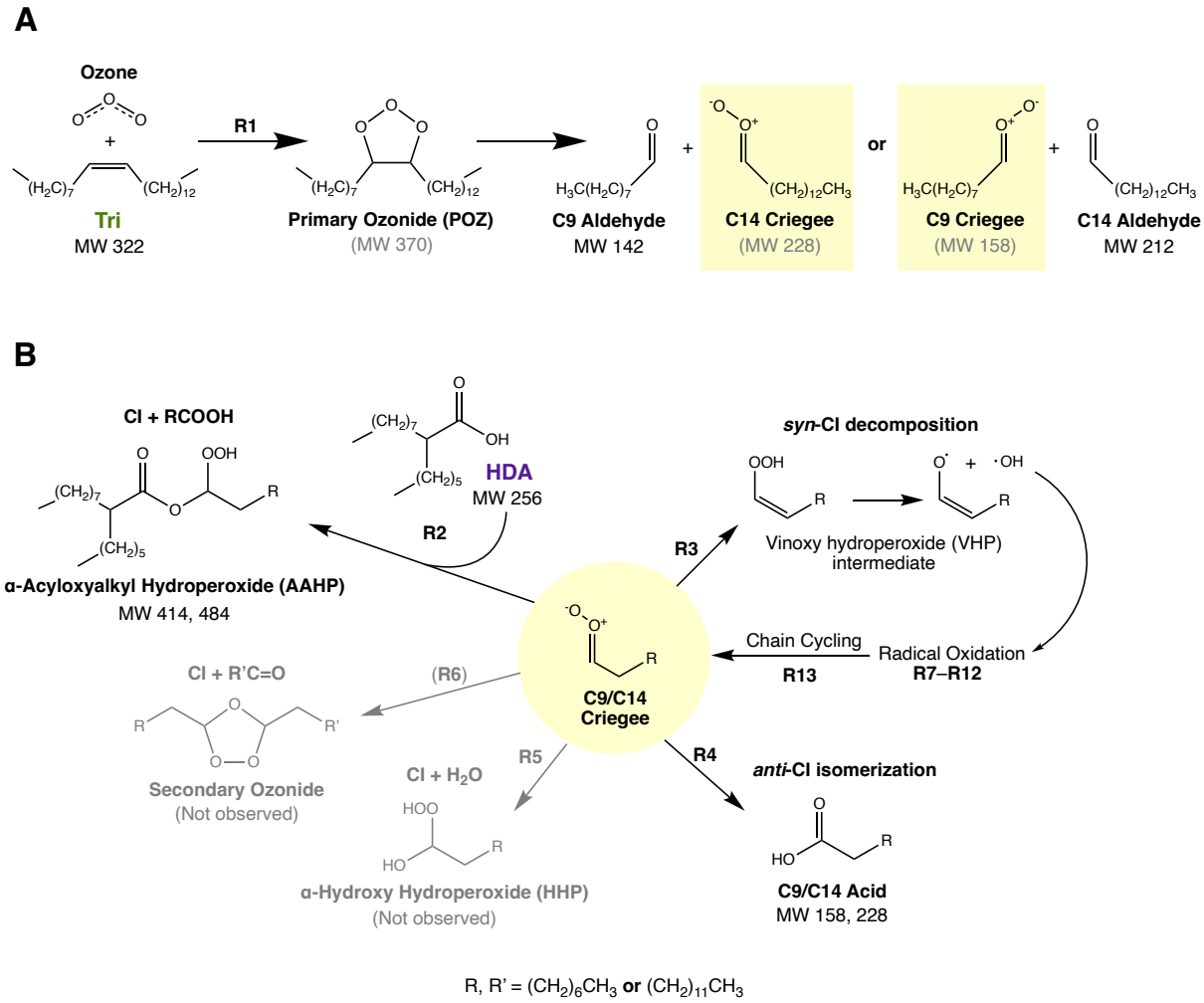

Scheme 2.1. Mechanism of ozonolysis and secondary chemistry observed in this system, as well as the identities of major reactants, products, and intermediates. (**a**) The primary ozonolysis reaction (R1), displaying the reactants (Tri, ozone), the primary ozonide (POZ) intermediate, and the two possible pairs of reaction products. The POZ is assumed to rapidly decompose, and sCI are not observed directly. (**b**) The secondary chemistry, consisting of reaction of sCI (center) with HDA (R2), as well as additional unimolecular (R3, R4) and bimolecular (R5, R6) sinks of sCI considered in this study. Secondary ozonide and HHP products are not observed. Refer to Table

2.S2 (Supporting Information) for a complete mechanism description, including the radical oxidation (R7-R12) and chain cycling (R13) steps included in stochastic kinetic simulations.

2.2 Experimental

2.2.A. Experimental Description

A flow tube reactor (Fig. 2.S1) is used to measure the ozonolysis of Tri:HDA mixtures in mole ratios of 100:0, 95:5, 80:20, 60:40, 40:60, and 15:85 (see Table 2.S1 for a detailed list of experimental conditions). Particles are generated by homogeneous nucleation in a tube furnace. For each mixture, a Pyrex tube is charged with small amounts of Tri (97%, Sigma-Aldrich Co.) and HDA (96%, Sigma-Aldrich Co.), between 2–4 mL in total, using a micropipette. The tube is inserted into the furnace and heated to 110–115 ˚C. 0.3 standard liters per minute (SLM) of dry nitrogen at room temperature is passed through the Pyrex tube, producing polydisperse particles. As the vapor pressures of both organics are expected to be similar (~$1x10^{-5}$ torr at 25 ˚C), the composition of the particles is assumed to match that of the bulk mixture. The resulting flow passes through an annular charcoal denuder to remove residual organics in the gas phase, and then enters the flow tube reactor. Particle distributions are measured at the exit of the flow tube using a Scanning Mobility Particle Spectrometer (SMPS) consisting of a Differential Mobility Analyzer (3080, TSI Inc.) and a Condensation Particle Counter (3025A, TSI Inc.) For pure Tri experiments, the mean diameter of the log-normal distribution lies between 430–480 nm with a geometric standard deviation (σ_g) of 1.29. The tail of this distribution extends beyond the measurement range of the SMPS, so this value for σ_g is an underestimate. In mixture experiments, the mean diameters of the particle distributions lie between 245–370 nm, with σ_g ranging from 1.35 to 1.68.

The cylindrical quartz flow tube reactor is 147 cm in length and 2.4 cm in diameter, resulting in a volume of 665 cm^3, which, given a typical total flow of 1.03 SLM, results in a residence time of approximately 39 seconds. In addition to the 0.3 SLM flow of particle-laden N_2, 0.5 SLM of pure N_2 and 0.2 SLM of dry O_2 (99.993%, Praxair) are introduced at the inlet of the reactor. During reactions, ozone is generated using a 0.1 SLM flow of O_2 into a corona discharge source (Ozone Services, Yanco Industries), after which this flow is diluted with 5 SLM of N_2 in a glass mixing cell. The concentration of O_3 in the flow is measured with a commercial ozone monitor (106M, 2B Technologies) at the exit of the mixing cell. The voltage on the corona discharge source can be adjusted to achieve O_3 concentrations between 8–640 ppm. A rotameter (King Instruments) is used to deliver 30 standard cubic centimeters per minute (SCCM) of the diluted $O_3/O_2/N_2$ flow into the flow tube reactor, where resulting O_3 concentrations range from 0.2-20 ppm. At the exit of the flow tube, the flow passes through an annular denuder packed with Carulite 200 catalyst, which catalytically destroys O_3 and terminates the reaction. During the course of all experiments described here, no unexpected or unusually high safety hazards were encountered.

2.2.B. APCI Mass Spectrometry

The reaction kinetics are monitored using a Thermo Scientific Velos Pro LTQ Mass Spectrometer fitted with an Atmospheric Pressure Chemical Ionization (APCI) source, modified to take particle-laden gas-phase flow through a ceramic inner bore, as described by Roveretto and co-workers[14] and shown in Fig. 2.S1. The outer ceramic inlet tube is heated to 180 ˚C to vaporize the aerosol particles prior to entering the ionization region. The flow into the inlet of the MS includes N_2 sheath gas at a flow setting on the mass spectrometer of 1.8 (arbitrary units). Auxiliary

gas flow is not used. Mass spectra are recorded over the mass range of *m/z* = 50–1000, in both positive and negative ion mode. In positive ion mode, the corona discharge needle is set to 4 kV with a typical current of 5μA, while in negative ion mode the discharge voltage is set to 1.5kV with a typical current of 8μA. The analyzer region of the mass spectrometer is maintained with Helium gas (99.998%, Airgas) at 40 psi.

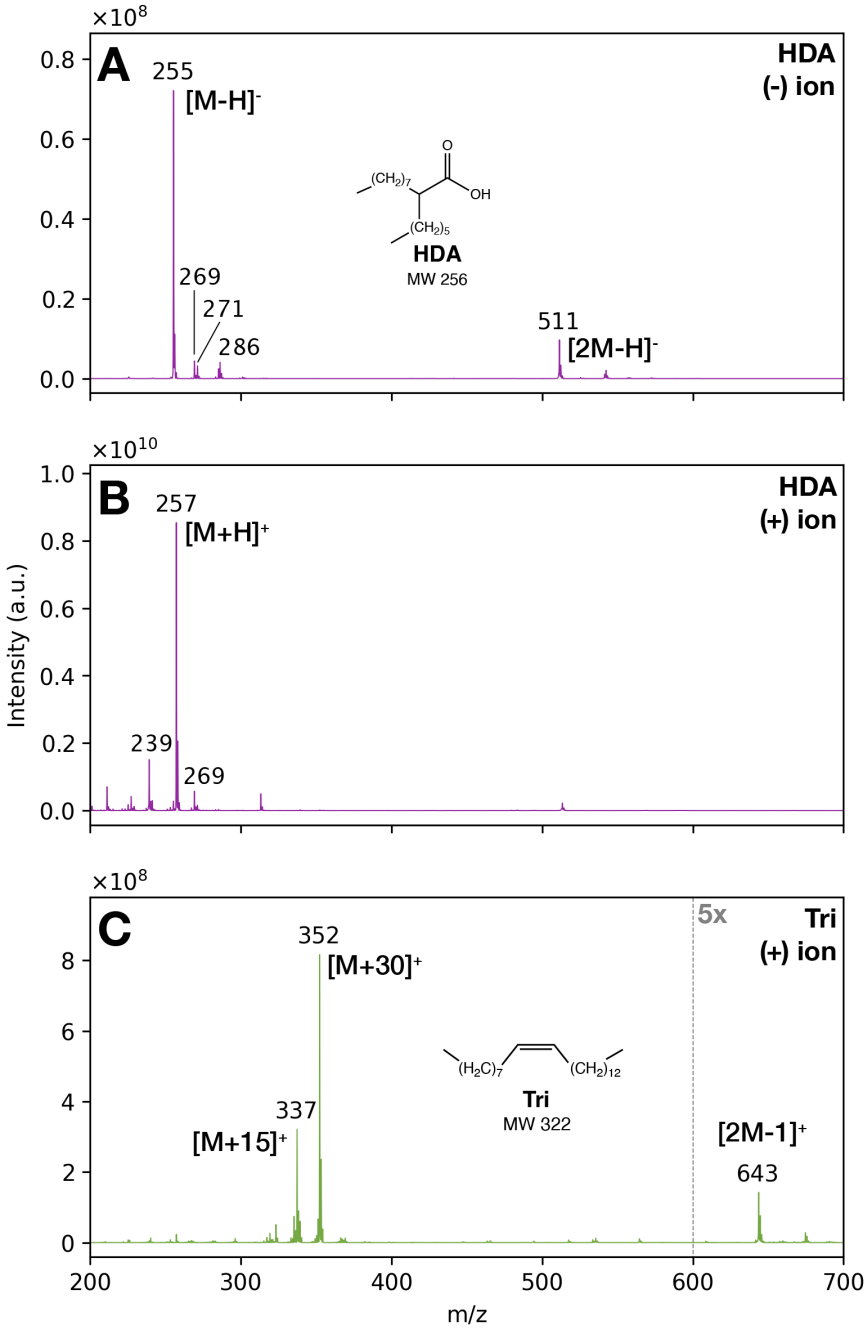

Figure 2.1. APCI Mass spectra of aerosols of pure reactants. a) HDA, negative ion mode mass spectrum, showing the deprotonated dimer peak at m/z = 511. b) HDA positive ion mode mass spectrum. c) Tri positive ion mode mass spectrum, with the region from m/z = 600 to 700 in the Tri spectrum magnified by a factor of 5 to highlight the $[2M-1]^+$ dimer peak at m/z = 643.

The negative and positive ion mass spectra of HDA, and the positive ion spectrum of Tri, are shown in Fig. 2.1A-C. The peak at *m/z* = 255 in Fig. 2.1A corresponds to the $[M-H]^-$ ion of HDA. Deprotonation of acidic functional groups is a dominant mechanism by which APCI

produces negative ions.[15,16] The small clusters of peaks above *m/z* = 255 likely correspond to ketone or alcohol products of radical chemistry occurring in the ionization region, resulting in the +14 and +16 peaks visible in the clusters. Also shown in Fig. 2.1A is a strong peak at *m/z* = 511, corresponding to a $[2M-H]^-$ deprotonated dimer of HDA. In the positive ion mode, APCI primarily generates ions through protonation of oxygenated functional groups to form $[M+H]^+$ ions[16] resulting in the *m/z* = 257 peak observed in Fig. 2.1B, but peaks attributed to oxidation (*m/z* = 269), water loss (m/z = 239), and background species can also be observed. Note that the magnitude of the signal in the positive ion spectrum is two orders of magnitude larger than the negative ion spectrum for HDA.

Tri, being entirely aliphatic, undergoes a different mechanism for positive ion formation. As seen in Fig. 2.1C, the major positive ion is *m/z* = 352, corresponding to $[M+30]^+$, with a smaller peak at *m/z* = 337 (i.e., $[M+15]^+$). Aliphatic compounds in APCI sources typically undergo ionization through hydride charge transfer, which can be accompanied by reductive elimination of H_2, resulting in an $[M-3]^+$ fragment ion.[17] In the presence of ambient H_2O, this ion can then be hydrated to form an $[M+15]^+$ species, or in an excess of O_2 in the ionization region, addition of HO_2 appears to be favored, resulting in the formation of $[M+30]^+$. Dimer formation following hydride charge transfer forms the $[2M-1]^+$ ion visible at *m/z* = 643 in Fig. 2.1C. The negative-mode spectrum for Tri shows signs of similar charge-transfer and oxidation or hydration ionization mechanisms, however the signal from neat Tri in negative mode APCI is extremely small. As a result, the negative ion polarity was not used to quantify Tri decay kinetics and is not shown.

2.3 Results

2.3.A. Reaction Products: Mass Spectra

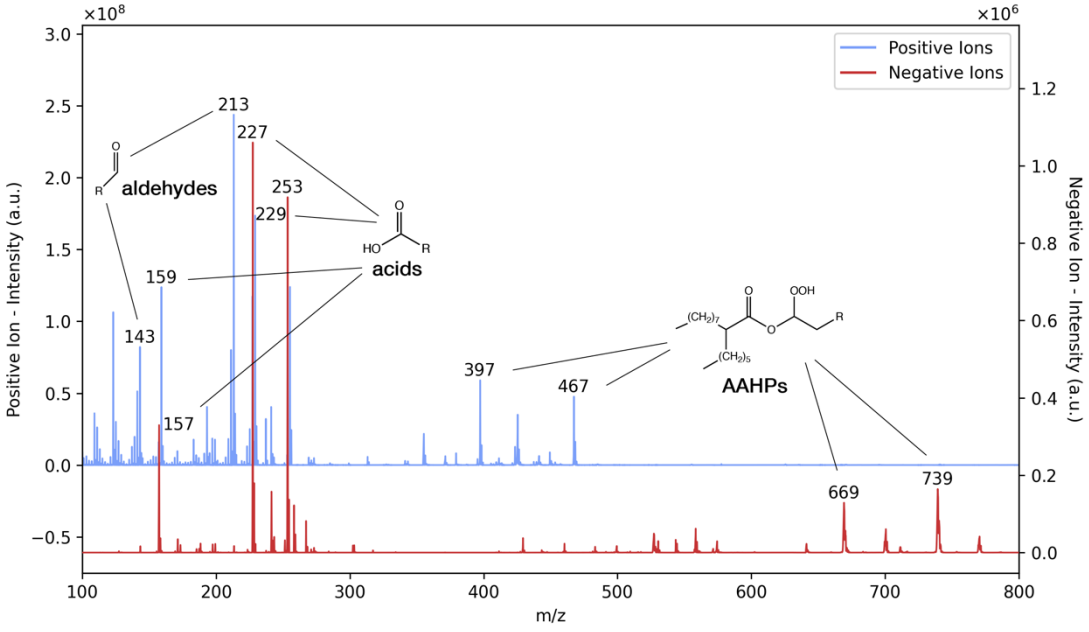

Figure 2.2. Representative difference mass spectra of an ozonized 80:20 Tri:HDA reaction mixture. The positive ion mode spectrum (blue, upper) and negative ion mode spectrum (red,

lower) are presented offset on the same axes to show the complementary peaks in the lower molecular weight region of the spectrum. Major peaks of the AAHP products are clearly visible in both positive ion mode (*m/z* = 397, 467) and negative ion mode (*m/z* = 669, 739).

Upon exposure to ozone, the mass spectrum of the reaction matrix (Fig. 2.2) exhibits a decay in the intensity of reactant peaks and the growth of product peaks, corresponding to both lower-molecular weight products from ozonolysis and new higher-molecular weight AAHP products, consistent with the mechanism shown in Scheme 2.1. Upon accommodating to the surface of the aerosol particle, an ozone molecule encounters the carbon-carbon double bond of Tri and undergoes cycloaddition to form a primary ozonide (POZ), which rapidly decomposes into one of two pairs of carbonyl oxide/aldehyde coproducts (R1, Scheme 2.1A). The positive ion mode peaks at *m/z* 143 and 213 in Fig. 2.2 correspond to the $[M+H]^+$ ions of nonanal ($C_9H_{18}O$, MW = 142) and tetradecanal ($C_{14}H_{28}O$, MW = 212). Since there are no labile hydrogens to be removed during chemical ionization, no corresponding negative ions are observed for the aldehydic products. The POZ ($C_{23}H_{46}O_3$, MW = 370) is not observed in either ionization mode.

After decomposition of the POZ, the chemistry in this reaction system, including radical chemistry, is mediated by sCIs, with the four reactions most significant for this study highlighted in Scheme 2.1B. The dominant unimolecular reaction of the *syn* sCI conformer, which has its terminal oxygen and alkyl chain on the same side of the C=O double bond, generates a hydroxyl radical *via* a vinyl hydroperoxide (VHP) intermediate formed through a 1,4 hydrogen shift (R3, Scheme 2.1B). The presence of this reactive channel in the Tri + O_3 system has been confirmed in a previous study[18] through the detection of ·OH radical oxidation products. Unfortunately, the products of this ·OH radical-initiated chemistry (R7-R12) (e.g., TriO, $TriO_2$, etc.) are isobaric with the oxidized background molecular ions observed in the APCI spectrum of neat Tri. Thus, products corresponding to radical chemistry cannot be definitively observed under current experimental conditions. The *anti* conformer of the sCI, which has its terminal oxygen atom pointed away from the alkyl substituent, can isomerize, forming a carboxylic acid (R4, Scheme 2.1B) *via* 1,3-cyclization followed by a ring-opening rearrangement. The two corresponding acids in this reaction system (nonanoic acid – $C_9H_{18}O_2$, MW 158; and tetradecanoic acid – $C_{14}H_{28}O_2$, MW 228) are clearly observed as pairs of $[M+H]^+$ and $[M-H]^-$ ions in the overlapping positive and negative ion spectra, appearing at *m/z* = 157 and 159, and m/z = 227 and 229 in Fig. 2.2.

Either conformer of the sCI can undergo bimolecular reactions to form hydroperoxide products, though with different rates.[2,19,20] Reaction of sCI with water (R5, Scheme 2.1B) will lead to the formation of α-hydroxy hydroperoxides (HHP), which may potentially decompose into corresponding carbonyl species *via* loss of H_2O_2.[21] Finally, the reaction between sCI and carboxylic acids (R2, Scheme 2.1B) form α-acyloxyalkyl hydroperoxides (AAHP), containing an ester functional group. The primary AAHP products formed in this system are $C_{25}H_{48}O_4$ (MW = 414) and $C_{30}H_{58}O_4$ (MW = 484), resulting from the addition of either the 9- or 14-carbon sCI to HDA. The two major high-molecular weight peaks in the positive ion spectrum, *m/z* = 397 and *m/z* = 467, are $[M-17]^+$ ions of these AAHPs, corresponding to OH loss. An identical pattern is visible in the negative ion spectrum, albeit at *m/z* 669 and 739. Collision-Induced Dissociation (CID) of these peaks (see Figs. 2.S2 and 2.S3) reveals them to be $[M+255]^-$ clusters, formed from the complex of the C_{25} and C_{30} AAHPs with an HDA carboxylate anion. Such clustering behavior is reasonable given the high ionization efficiency of negative mode APCI toward acids and the dimerization of HDA described earlier.

2.3.B. Reaction Kinetics: Uptake Coefficients

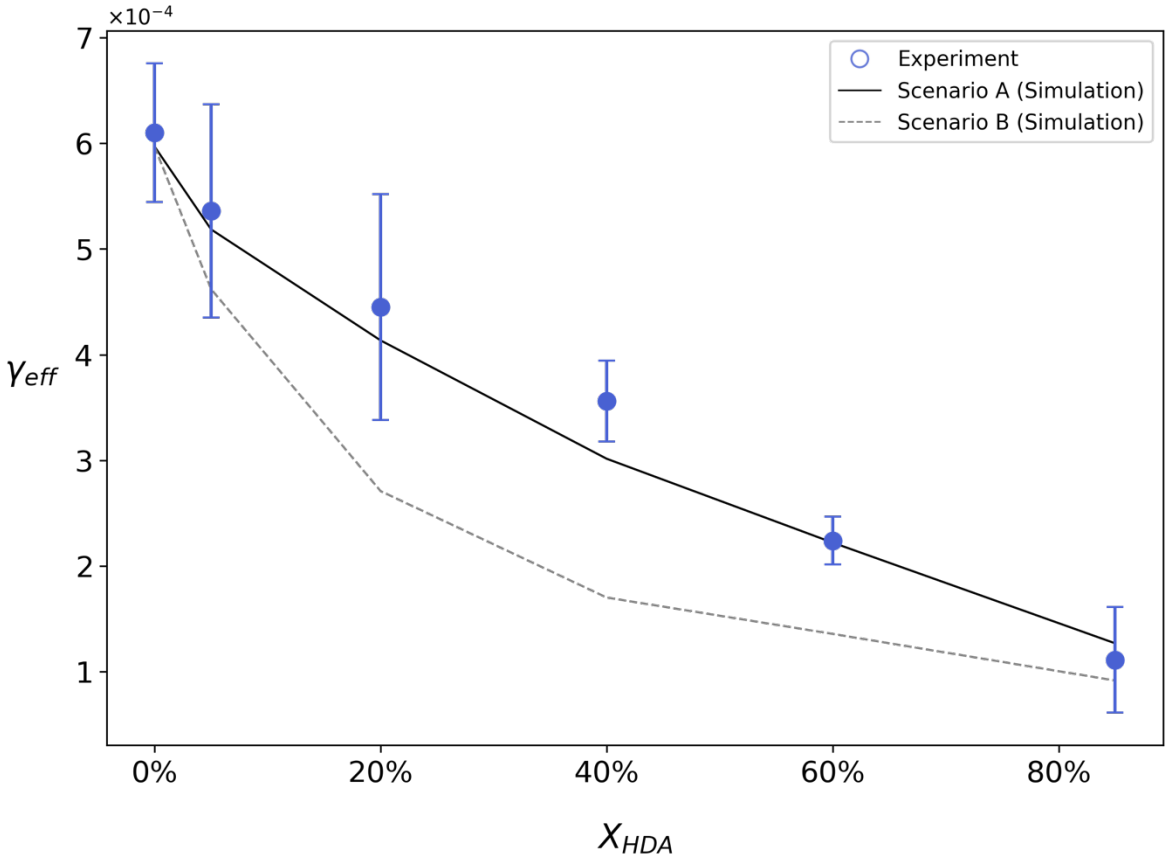

Figure 2.3. Reactive uptake coefficients as a function of HDA mole fraction. Points correspond to the mean of at least 3 experimental measurements, and error bars represent ±1 standard deviation from the mean. Lines represent the results of explicit kinetic simulations under two different modeling scenarios (see Section 4.3): Scenario A (solid black line), where k_{AAHP} is fixed at 2.1x10^{-19} cm^3 molec.$^{-1}$ sec.$^{-1}$ in accord with the empirical rate presented in Section 4.2; and Scenario B (dashed black line), where k_{AAHP} is fixed at 1x10^{-13} cm^3 molec.$^{-1}$ sec.$^{-1}$ to represent a rate limited only by diffusion in the organic matrix. Further model sensitivity tests of k_{AAHP} within an order of magnitude of the Scenario A value can be found in Fig. 2.S10 of the Supporting Information.

The reaction probability of Tri, also termed the effective reactive uptake coefficient (γ_{eff}), is an informative metric of the rate of a heterogeneous reaction and has been defined previously.[22–24] Briefly, γ_{eff} here represents the ratio of the consumption rate of Tri (corrected for its mole fraction in the mixture) to the collision rate of gaseous ozone. Although γ_{eff} is generally less than 1, it can be > 1 in cases, such as in the presence of radical chain reactions, when the arrival of a molecule of the gaseous reactant results in the consumption of more than one molecule of the condensed phase reactant.[22,24,25] In Fig. 2.3, γ_{eff} for Tri is observed to be a function of the mole fraction of

HDA in the aerosol (X_{HDA}). γ_{eff} for neat Tri aerosol measured in this study is 6.5×10^{-4}, and is in agreement with previous measurements by Zeng and Wilson (5.2×10^{-4}, obtained using aerosol photoionization mass spectrometry).[12] Zeng notes that this condensed-phase γ_{eff} is an order of magnitude greater than a previous uptake coefficient obtained using the decay of gas phase ozone. This difference is attributed to radical chain cycling, which accounts for a significant amount of the Tri consumption during the reaction.[26] Similar to the behavior observed by Zeng *et al.* upon addition of a saturated alcohol, the uptake coefficient decreases with increasing mole fraction of HDA. For example, an aerosol composed of 40% HDA exhibits a twofold decrease in γ_{eff} relative to neat Tri. This suggests that presence of RCOOH behaves as a sCI scavenger, as illustrated in Scheme 2.1B: instead of decomposing to form ·OH (R3), which accelerates Tri consumption through radical chain chemistry (R7–R13), sCIs react preferentially with the acid functional group (R2) when HDA is present. Although Zeng did not report data for additive mole fractions greater than 40%, the trend appears to continue linearly: a mixture composed of 85% HDA yields a sixfold decrease in γ_{eff}. Following Zeng's previous work, the addition of sCI to alkenes to form cyclic hydroperoxides is not thought to be kinetically significant in this system.[12] Furthermore, though HDA is expected to react with ·OH radicals, the rate of this reaction is expected to be an order of magnitude slower than that of ·OH addition to alkenes, which is the predominant radical initiation step in this mechanism.[27] Accordingly, assuming the sole reactive sinks for sCI are isomerization to produce ·OH radical and bimolecular reaction with HDA, the decrease in uptake with increased HDA concentration suggests that the rates of these processes are competitive under the experimental conditions studied here. The decrease in γ_{eff} with [HDA] is accurately predicted by the kinetic model developed by Zeng *et al.*, which is slightly adapted to describe these experiments as discussed in Section 4.3. The values of γ_{eff} predicted by the model for two values of the bimolecular rate coefficient k_{AAHP} are additionally shown in Fig. 2.3 as will be detailed below.

2.3.C. Reaction Kinetics: Decay of HDA

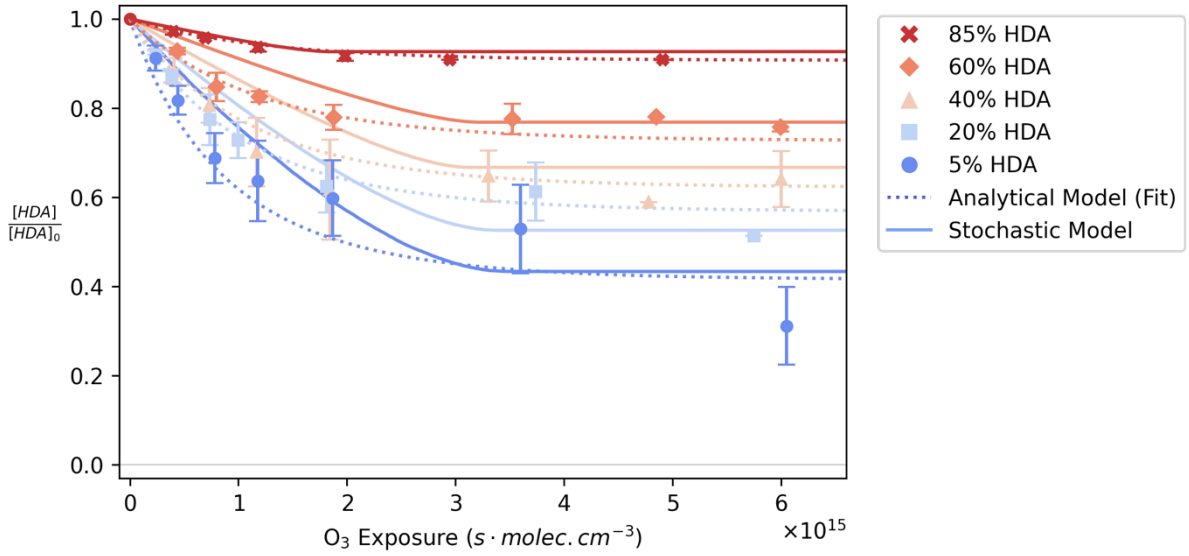

Figure 2.4. The decay of the HDA signal intensity with ozone exposure, normalized to unreacted HDA signal for aerosols having HDA mole fractions (from top to bottom) of 85%, 60%, 40%, 20%, and 5%. Symbols represent the mean of data from at least three experiments for each

condition, and error bars represent ±1 standard deviation from the mean. Dotted lines represent fits of Eq. 2.6 to the experimental data, as described further in Section 4.2. Solid lines represent the results of explicit stochastic kinetic simulations under Scenario A, as described in Section 4.3.

The decay of HDA with increasing ozone exposure reveals additional information about the reactivity of sCI in this matrix. In Fig. 2.4, the normalized intensity of the HDA signal is shown as a function of ozone exposure for each reaction mixture outlined in Table 2.S1. In each experiment, the amount of HDA remaining approaches a limiting value that depends upon the initial HDA and Tri concentrations. For example, for an aerosol that is comprised of 85% HDA, nearly 90% of the HDA remains at the end of the reaction, while the mixture composed of only 5% HDA reaches a limiting value of roughly 30% after ozonolysis. As there are no other reactive sinks for HDA, this decay in the HDA concentration arises from its reaction with sCIs. It is apparent from this data that HDA is not a limiting reactant in the sCI+RCOOH reaction, as HDA is not entirely consumed in mixtures where $X_{HDA} << 0.5$. Instead, a non-zero limiting value of HDA is found at high ozone exposures, once most of the Tri has been consumed and sCIs are no longer being produced directly from ozonolysis. This indicates that the reaction between the sCIs and HDA (R2, Scheme 2.1B) must be slow enough to allow the other sinks for the sCI (R3-R6) to compete. Since the range of relevant reactions of the sCI is sufficiently constrained in this system, it is possible to quantify this competition in terms of the rate constants governing each pathway, as described below.

2.4 Discussion

2.4.A. Analytical Kinetic Model

An analytical kinetic model for the decay of HDA can be used to quantify the competitive sCI reaction pathways in this system. The rate law for [HDA] is,

$$\frac{d[\mathrm{HDA}]}{dt} = -k_{\mathrm{AAHP}}[\mathrm{HDA}][\mathrm{sCI}] \qquad \text{Eq. (2.1)}$$

where k_{AAHP} is the bimolecular rate constant for the sCI + HDA reactions that forms AAHP products. The corresponding rate law that describes the time dependence of [sCI] is,

$$\frac{d[\mathrm{sCI}]}{dt} = k_{\mathrm{O3}}[\mathrm{Tri}][\mathrm{O_3}] - [\mathrm{sCI}](k_{\mathrm{iso}} + k_{\mathrm{VHP}} + k_{\mathrm{H2O}}[\mathrm{H_2O}] + k_{\mathrm{AAHP}}[\mathrm{HDA}]) \qquad \text{Eq. (2.2)}$$

where k_{O3} is the bimolecular rate constant for alkene ozonolysis assuming that POZ decomposition is not rate-limiting (R1, Scheme 2.1A). k_{iso} and k_{VHP} (R3–R4, Scheme 2.1B) are the unimolecular rate constants for isomerization to the carboxylic acid and the VHP intermediate, respectively, and k_{H2O} is the bimolecular rate constant for reaction with water to form HHPs (R5). As mentioned in the previous section, some potential sinks for HDA and sCI, as well as the effects of volatile product evaporation, are assumed here to be negligible for the sake of simplicity. A more complete mechanism, derived from Zeng's previous work,[12] is implemented in the stochastic kinetic simulations discussed in Section 4.3 and accounts for radical chain reactions and the

evaporation of volatile products. The agreement between the stochastic kinetic simulations and the predictions of the model derived here is discussed in Section 4.4.

To find an expression for the [sCI], a steady-state approximation is made (e.g., that [sCI] will remain small and roughly constant for the duration of the reaction) which yields the following expression:

$$[\mathrm{sCI}]_{\mathrm{ss}} = \frac{k_{\mathrm{O3}}[\mathrm{Tri}][\mathrm{O_3}]}{k_{\mathrm{uni}}+k_{\mathrm{H2O}}[\mathrm{H_2O}]+k_{\mathrm{AAHP}}[\mathrm{HDA}]} \qquad \text{Eq. (2.3)}$$

where the two unimolecular rate constants are combined such that $k_{\mathrm{uni}} = k_{\mathrm{iso}} + k_{\mathrm{VHP}}$. Although the steady state assumption breaks down when there is a strong time-dependence to the intermediate concentration, the steady-state approach taken here can be justified by pseudo-first order rate analysis. For the case of neat Tri + O_3, the production rate governed by ozonolysis of the alkene (first term of Eq. 2.2) can be calculated via Eq. 2.5 below to be approximately 0.01 s^{-1}. As this is several orders of magnitude smaller than the combined sCI loss rate (second term of Eq. 2.2), thought to be on the order of 10^2 s^{-1},[20] the sCI are expected to reach their maximum concentration rapidly. Recent experimental evidence[28] has indicated that sCI remain detectable for minutes after their formation in viscous secondary organic aerosol, longer than the 39 sec. flow tube residence time in this work, suggesting that the sCI population may not deviate far from a steady state concentration over the duration of the measurements reported here. In addition, as discussed in Section 4.3, the results of this simple kinetic model agree with explicit kinetic simulations where no such steady-state assumptions are made.

The term describing the reaction with HDA in Eq. 2.3 can then be considered a perturbation to the equilibrium concentration of sCI, and the system of equations can be solved self-consistently. Substitution of Eq. 2.3 into Eq. 2.1 yields,

$$\frac{d[\mathrm{HDA}]}{dt} = \frac{-k_{\mathrm{AAHP}}[\mathrm{HDA}]\cdot k_2[\mathrm{Tri}][\mathrm{O_3}]}{k_{\mathrm{uni}}+k_{\mathrm{H2O}}[\mathrm{H_2O}]+k_{\mathrm{AAHP}}[\mathrm{HDA}]} \qquad \text{Eq. (2.4)}$$

For simplicity, the decay of Tri is approximated as an exponential function (i.e. $e^{-k_{rxn}\cdot t}$). Although the decay of Tri is generally non-exponential (see Fig. 2.S7), an exponential approximation holds sufficiently well for small ozone exposures and is used to calculate uptake coefficients. Since the ozone concentration is constant during the reaction, the heterogeneous rate constant (k_{rxn}) can be expressed as,

$$k_{\mathrm{rxn}} = k_{O3}[\mathrm{O_3}] = \frac{6\cdot\gamma\cdot\bar{c}\cdot M}{4\cdot D_p\cdot\rho_0\cdot N_A}[\mathrm{O_3}] \qquad \text{Eq. (2.5)}$$

where $\bar{c}$ is the mean speed of ozone, M is the molar mass of Tri (322 g/mol), D_p is the particle diameter, ρ_0 is the density of Tri (~1.5x10^{21} molec./cm^3), and N_A is Avogadro's number. Integrating Eq. 2.4 then yields the following expression for the time-dependence of HDA:

$$[\mathrm{HDA}](t) = \left(\frac{1}{k'}\right) \cdot W_0\left\{k'[\mathrm{HDA}]_0 \cdot exp\left(k' \cdot \left([\mathrm{HDA}]_0 + [\mathrm{Tri}]_0(e^{-k_{\mathrm{rxn}} \cdot t} - 1)\right)\right)\right\} \quad \text{Eq. (2.6)}$$

$$k' = \frac{k_{\mathrm{AAHP}}}{k_{\mathrm{uni}} + k_{\mathrm{H2O}}[H_2O]} \quad \text{Eq. (2.7)}$$

where $[\mathrm{HDA}]_0$ and $[\mathrm{Tri}]_0$ are the initial concentrations of HDA and Tri, respectively, and $W_0\{x\}$ is the principal branch of the Lambert W-function. The Lambert W-Function is a non-elementary function that has been used to provide analytical solutions to differential equations in chemical kinetics, notably in enzyme kinetics, and its implementations are readily available in Mathematica, Python, Matlab, and other platforms. Eq. 2.6 suggests that the relevant kinetic parameter controlling the decay of HDA is k', the ratio of the sCI + RCOOH bimolecular rate constant to the sum of the first-order loss rates for the sCI.

2.4.B. Fitting Analytical Model to HDA Decay

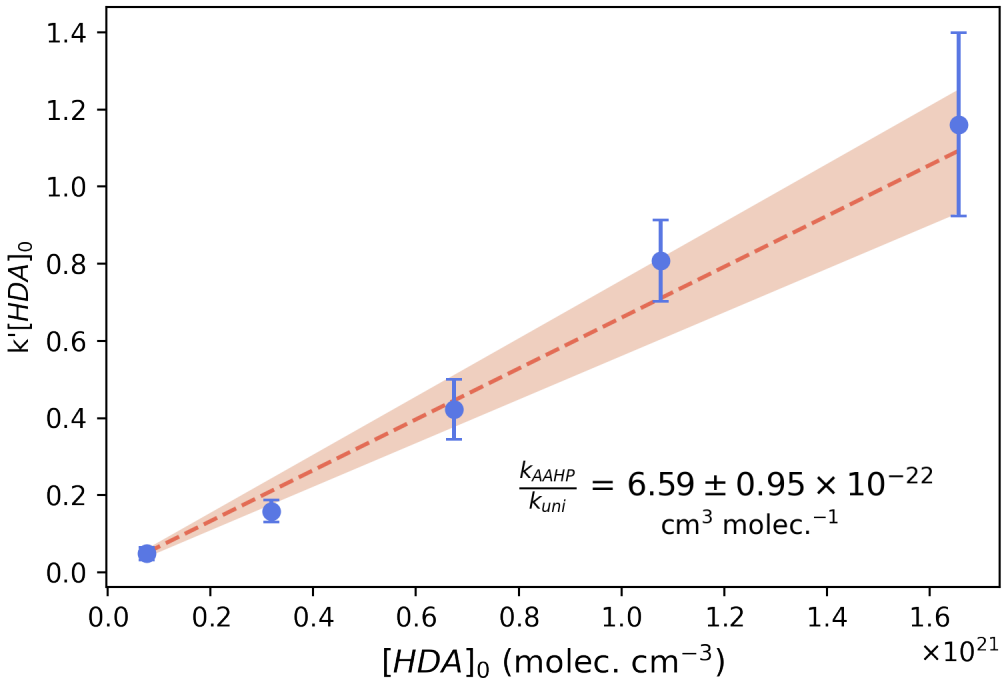

Figure 2.5. Pseudo-first order plot of fitted k'$[\mathrm{HDA}]_0$ values (unitless) versus initial HDA concentration in each aerosol mixture. Points represent the mean value of k'$[\mathrm{HDA}]_0$ obtained from fits to the experimental data in Fig. 2.4. Error bars represent ±1 standard deviation from the mean. The dashed line represents a linear fit to these points, with the slope of the line estimating the value of k' to be 6.59 ± 0.95 x 10^{-22} cm^3 $molec.^{-1}$. The shaded region represents fits to the upper and lower bounds of the error, from which the error in the slope was obtained.

By normalizing the expression in Eq. 2.6 to $[HDA]_0$, the equation can be directly compared to the experimental data in Fig. 2.4. Of the four parameters in Eq. 2.6, $[Tri]_0$ and $[HDA]_0$ are related by the bulk densities and mole fractions of the organic mixture, and k_{rxn} is obtained from the observed decay of Tri, leaving *k'* as the sole adjustable parameter. The quantity $k'[HDA]_0$ is extracted from each experimental dataset in Fig. 2.4 through non-linear fitting, implemented in Python with the *scipy.optimize.curve_fit* function. The corresponding best fits to the aggregated experimental data are shown in Fig. 2.4 as dotted lines. The average values of $k'[HDA]_0$ retrieved from each fit are plotted in Fig. 2.5 as a function of $[HDA]_0$ and exhibit a linear relationship. Analogous to a pseudo-first order method of determining a rate constant, the slope of the best fit line through the points in Fig. 2.5 is found yielding $k' = 6.59 \pm 0.95 \times 10^{-22}$ cm^3 molec.$^{-1}$

Despite its rather simple assumptions, the analytical model provides an excellent fit to the experimental data. Although the value of k' fixes only a ratio of rate constants and not their absolute value, the k' derived from the fit in Fig. 2.5 may be combined with theoretical estimates of the unimolecular and sCI-water rate constants to make a prediction about the magnitude of k_{AAHP}. The structure activity relationships (SAR) of Vereecken et al.[20] show that for primary ethyl or propyl sCI in the *anti* conformation, the isomerization channel to produce acids (R4, Scheme 2.1B) has a rate constant of 74 s^{-1}, whereas for the *syn* conformation, the isomerization to the VHP intermediate (R3) has a rate constant of 205 s^{-1}. Since the experiments are conducted using dry gases without introducing water vapor, the loss of sCI to water (R5) is assumed to be negligible. Zeng assumed a small but non-zero RH value (~3%) in dry experiments to account for the potential of ambient water in the flow system and, using the k_{H2O} calculated by Vereecken,[20] estimated the $k_{H2O}[H_2O]$ term to be roughly 2 s^{-1}.[12] Combining the first-order loss rates yields $k_{uni} + k_{H2O}[H_2O]$ as 281 s^{-1}, and multiplying this value by k' yields $k_{AAHP} = 1.85 \pm 0.27 \times 10^{-19}$ cm^3 molec.$^{-1}$ sec^{-1}.

Compared to the gas phase, where k_{AAHP} has been measured to exceed 10^{-10} cm^3 molec.$^{-1}$ sec.$^{-1}$, the value of the rate constant derived here is quite small, but not without precedent. Interestingly, although they allow the value of k_{AAHP} to vary between datasets in their model of oleic acid ozonolysis, Gallimore and co-workers report a ratio k_{AAHP}/k_{uni} of 5×10^{-22} cm^3 mol.$^{-1}$ (0.3 M^{-1}), and fix k_{uni} at 500 s^{-1} based on empirical measurements, a factor of 2 greater than the k_{uni} determined here.[10] Using Gallimore's parameters, the resulting value of k_{AAHP} is 2.5×10^{-19} cm^3 molec.$^{-1}$ sec.$^{-1}$, in excellent agreement with the estimate provided above. In Berkemeier *et al.*, although a specific value of k_{AAHP} was not reported, k_{AAHP} was allowed to vary between 10^{-18}–10^{-12} cm^3 molec.$^{-1}$ sec.$^{-1}$, the lower bound lying just above the empirical estimate derived from Fig. 2.5.[11]

2.4.C. Stochastic Kinetic Simulations

To test the assumptions made in the derivation of Eq. 2.6, we use a stochastic kinetic simulation using the explicit mechanism developed by Zeng.[12] This mechanism includes ·OH production during multiphase ozonolysis, which is neglected in the derivation of Eq. 2.6. The production of ·OH and other radicals were identified as significant reactive sink for Tri during multiphase ozonolysis. As shown by Zeng, the ·OH radical produced by the decomposition of the sCI can add to a C=C bond to form a β-hydroxy RO_2 radical.[18] As first reported by Beauchamp and coworkers,[29] this β-hydroxy RO_2 radical can, in turn, reform sCIs, via a mechanism that is currently unclear.[30] While the empirical decay rate of Tri employed in this model should partially account for additional Tri consumption by ·OH radicals, Eq. 2.6 does not account for the production of sCI via the β-RO_2 pathway. Additionally, other potentially important reactive sinks

for sCI, such as its direct reaction with ozone are also not included in the derivation of Eq. 2.6. (These reactions are not shown in Scheme 2.1 but are detailed in Table 2.S2 in the Supporting Information.) To evaluate the reasonableness of the model derived in Section 4.1 and the corresponding estimate of k_{AAHP}, explicit stochastic simulations of the system are run in Kinetiscope,[31] an open-source software package that implements a kinetic Monte Carlo algorithm for a user-defined reaction mechanism. Multiple previous studies have used models built in Kinetiscope to accurately describe heterogeneous chemistry in aerosols, including Tri ozonolysis in the presence of a sCI scavenger.[12,32,33]

The previously-developed simulation framework has been adapted to the current reaction and the full mechanism is described Table 2.S2 (Supporting Information). In particular, the isomerization of sCI to form acids (R4) is included, to explain the product acids observed in Fig. 2.2. The reaction between HDA and the ·OH radicals produced from sCI decomposition makes a small contribution to the decay kinetics of HDA, and so is also included. Following Zeng's previous studies of Tri ozonolysis,[12,18] the formation of secondary ozonide (SOZ) products (Scheme 2.1B, R6) is not included as they were not observed under multiple ionization methods. Although equilibrium partitioning calculations[13] predict that some tetradecanal may remain in the particle available for reaction, model sensitivity tests including this pathway are out of agreement with experimental results, as detailed in Fig. 2.S5 of the Supporting Information. Finally, the evaporation of nonanal (R14) is allowed in the simulation to account for the slight change in particle diameter observed over the course of the reaction. As discussed by Müller et al. in the context of oleic acid ozonolysis,[34] reaction time and oxidant exposure may not be equivalent measures of reaction progress in experiments involving high oxidant concentrations, owing to the evaporation of volatile products. Since the experimental kinetic data presented here is measured in terms of oxidant exposure and involves high (ppm) oxidant concentrations, the inclusion of evaporation steps in the stochastic model is important for validating the value of k_{AAHP} derived from experiment. A comparison of the simulated and observed particle diameter for neat Tri aerosol and for each of the binary mixtures in this study is shown in Fig. 2.S6, and the agreement between stochastic model predictions and other experimental observations is discussed below.

The value of k_{AAHP} is treated as the sole adjustable parameter in the model, allowing for direct evaluation of the reasonableness of the rate constant derived from Eq. 2.6. Shown in Fig. 2.3 are two modeling scenarios using two different values for k_{AAHP}. In Scenario A, the value of k_{AAHP} is chosen to be 2.2×10^{-19} cm^3 molec.$^{-1}$ sec.$^{-1}$, which lies just beyond one standard deviation from the mean of the empirical estimate given in the previous section. This value was chosen to produce the best qualitative agreement with the data in Fig. 2.4. The uptake coefficients predicted under Scenario A are represented by the vertices of the solid line in Fig. 2.3. Scenario A closely reproduces both the observed uptake coefficients and the decay kinetics of Tri (Fig. 2.S7).

By contrast, k_{AAHP} is fixed at 1×10^{-13} cm^3 molec.$^{-1}$ sec.$^{-1}$ in Scenario B, to represent the sCI+RCOOH reaction occurring at a rate near the diffusion limit. Uptake coefficients corresponding to this scenario are represented by the dashed line in Fig. 2.3, which deviates sharply from the experimental results at low HDA fractions and flattens once X_{HDA} exceeds 50%. Fig. 2.S8 shows the Tri decay kinetics corresponding to these predictions, which exhibit a linear initial consumption rate of Tri, followed by sharp transition to a region of non-linear decay. The simulated decay of HDA in Fig. 2.S9 explains these unphysical predictions: when X_{HDA} is below 50%, a sCI + RCOOH reaction occurring at the diffusion limit far outcompetes all other sCI sinks, resulting in a zero-order (linear) decay of HDA until it is consumed. Once X_{HDA} exceeds 50%, the uptake is

limited primarily by the amount of Tri available, and further increases in HDA have minimal impact on the uptake coefficient. As scenario B clearly does not describe the observed trend in γ_{eff} or in the decay of HDA, a rate constant near the diffusion limit can be ruled out. Additionally, to ensure that the simulation results were sufficiently sensitive to allow specification of k_{AAHP}, simulations were run with values of k_{AAHP} both an order of magnitude greater and an order of magnitude smaller than the value specified in Scenario A. The resulting values of γ_{eff} and simulated decay traces for X_{HDA} = 20%can be seen in Fig. 2.S10.

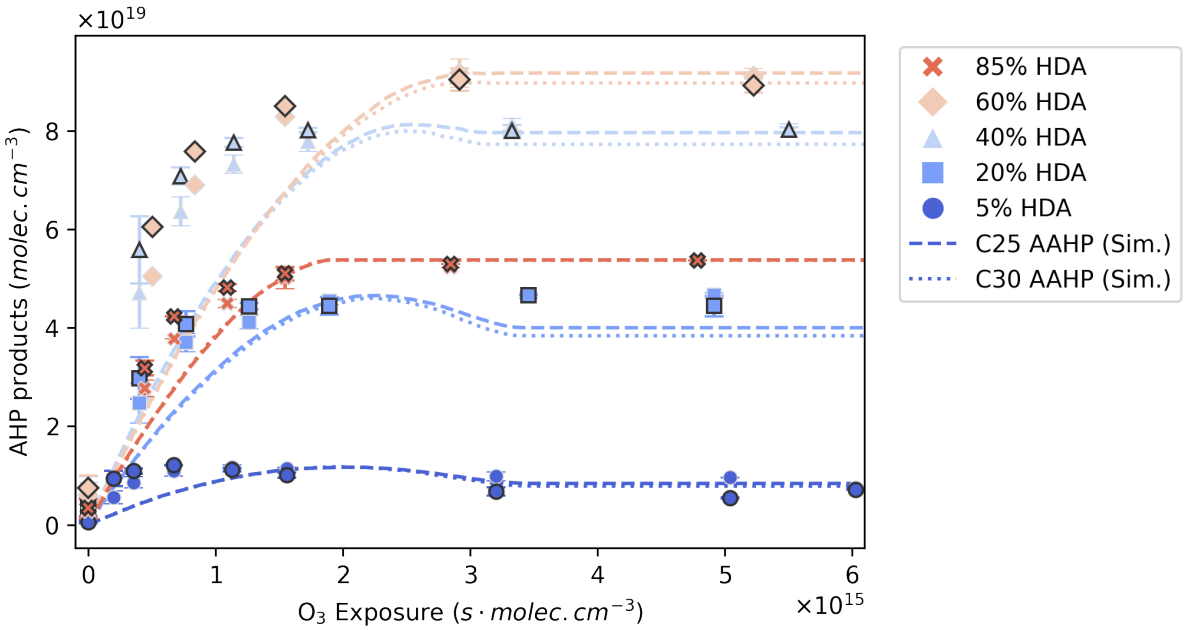

Figure 2.6. The kinetic evolution of AAHP reaction products at each HDA mole fraction, comparing experimental observations (points) to the results of explicit kinetic simulations under Scenario A (solid lines). Observations correspond to integrated intensities of mass spectral peaks corresponding to AAHP products. Light-outlined points correspond to C25 AAHPs (m/z = 397 in positive ion mode and m/z = 669 in negative ion mode), and dark-outlined points correspond to C30 AAHPs (m/z = 467 in positive ion mode and m/z = 739 in negative ion mode); see Section 3.1. Experimental data is scaled to match the maximum product concentration of each simulation result.

Further supporting the choice of rate constant in Scenario A, Fig. 2.6 shows the observed kinetics of the AAHP products overlaid with the kinetics predicted by Scenario A. At the lowest HDA mole fraction (5%), the experimental observation shows the AAHP products reach a peak concentration before then decaying gradually. This behavior is captured in the corresponding simulation results, where once the AAHP products form they are consumed by radicals. Agreement between this simulation and experimental results is acceptable for the scenarios where X_{HDA} is less than 50%, and is generally better than the corresponding prediction by Scenario B (Fig. 2.S11). When X_{HDA} is greater than 50%, a larger discrepancy between the experimental data and the model prediction arises and is evident for the 85% X_{HDA} case. This discrepancy seems to arise from the description of Tri decay kinetics (Fig. 2.S7). One potential explanation for this discrepancy is the

implicit assumptions governing ozone adsorption in the model. The current framework assumes that the number of adsorption sites on the surface of the particle is proportional solely to the mole fraction of Tri in the mixture. As more HDA is incorporated in an aerosol particle, fewer and fewer ozone adsorption sites are allowed, up to the limit that no adsorption sites are allowed for a pure HDA particle. The agreement between simulation and experiment at high X_{HDA} could be improved by allowing HDA to contribute adsorption sites, consistent with studies that suggest significant amounts of ozone adsorb to nonreactive fatty acid aerosols.[35,36] However, this modification has not been implemented in the present study to allow for ease of comparison with previously published modeling results.[12]

2.4.D. Comparison of Analytical & Stochastic Models

Both the explicit simulations and the analytical model indicate that the sCI + RCOOH rate constant is on the order of 10^{-19} cm^3 $molec.^{-1}$ $sec.^{-1}$, 9 orders of magnitude smaller than the gas phase rate constant. Assuming that the rate were limited only by reactant diffusion in the condensed phase, the expected rate constant would be 3.6×10^{-13} cm^3 $molec.^{-1}$ $sec.^{-1}$, given an organic liquid with viscosity of 15 mPa·s and reactant collisional radii of 2 nm. This diffusion-controlled rate coefficient is still significantly faster than the rate estimated by the kinetic analysis in this study. Several theoretical studies of this reaction in the gas phase concur that the prevailing entrance channel for the two reactants is barrierless, and leads to direct formation of the AAHP product via 1,4 addition, with formation of a pre-reactive complex not significantly contributing to the overall kinetics of the reaction.[19,37] Thus, it seems likely that entropic effects are significant in limiting this reaction in the condensed-phase. In particular, Vereecken reported that the approach geometry is a significant factor in determining reaction favorability, with preferred geometries having both molecules coplanar.[19]

This apparent deceleration of a rapid gas phase bimolecular sCI reaction when conducted in an aerosol is not without precedent. Heine and co-workers discussed a similar discrepancy between observations and gas-phase estimates for sCI cycloaddition to carbonyl (C=O) functionalities to form secondary ozonides during a modeling study of squalene ozonolysis.[32] There, sCI + C=O reaction rates were optimized to reproduce the observed SOZ formation kinetics, converging on two values for the rate constant: 6.7×10^{-19} cm^3 $molec.^{-1}$ $sec.^{-1}$ in cases where the sCI and C=O reactants are formed from different POZs, and a rate two times faster when the reactants are formed from decomposition of the same POZ. This effect is analogous to that observed for peroxy radical recombination rates,[38] where the organic matrix forms a "solvent cage" that increases the interaction time of reactants formed in proximity to one another, while reactants formed in separate cages must overcome a barrier before encountering another reactant by diffusion. The lipidic chains of Tri and HDA likely provide a similar solvation environment in the present system, forming an aliphatic shell that nascent sCIs must disrupt before encountering and reacting with a nearby HDA molecule.

2.5 Conclusion

The experimental data and modeling results presented here suggest that a reasonable rate constant for the sCI + RCOOH reaction in the condensed phase of an organic aerosol should be much slower than the diffusion limit in the condensed phase. The monotonic decrease in the reactive uptake coefficient of O_3 by Tri as more HDA is incorporated into the aerosol indicates that the sCI + RCOOH reaction behaves as a sCI scavenger, outcompeting the unimolecular decay process by which sCIs produce ·OH radicals and initiate radical chain chemistry. Direct

observations of the decay of HDA in the presence of Tri and O_3 confirm this hypothesis and show that HDA is not a limiting reactant over the range of mole fractions studied here. The decay kinetics of HDA are governed by the production and multifaceted consumption of sCI from ozonolysis, which lends itself to a simple kinetic model from which the ratio k_{AAHP}/k_{uni} can be extracted. Multiplying by a theoretical estimate of the unimolecular decay rate of sCI, the sCI + RCOOH rate constant is found to be $1.85 \pm 0.27 \times 10^{-19}$ cm^3 $molec.^{-1}$ $sec.^{-1}$. Explicit kinetic simulations using a value in this range agree well with experimental data.

Given the large difference between this rate coefficient and gas-phase measurements, further condensed-phase kinetic studies, such as in aqueous environments, may be valuable in understanding how this rate depends upon the solvation environment and the ultimate relevance of this reaction to the processing of atmospheric aerosol. In contrast to the gas phase, where the sCI + RCOOH reaction is expected to be a major reactive sink of sCI, acids may not outcompete other sCI reaction partners in more viscous condensed phases. As a result, careful measurements of other slow bimolecular reactions of sCI in non-aqueous condensed phases may be of value. The similarity of the rate constant estimated here for the sCI + RCOOH reactions to the rate constants adopted for sCI + alcohols and sCI + carbonyls in previous organic systems suggests that the composition of the condensed phase could be the most important factor in determining the rates of bimolecular reactions of sCI in organic aerosol. Finally, the formation of oligomeric AAHP species as a mechanism for particle growth should be analyzed more carefully, as heterogeneous reactions between sCI and acids may kinetically outcompete the corresponding homogeneous process.

2.6 Supporting Information

Table 2.S1. Experimental conditions and observations. D_p is average diameter and σ_g is the geometric standard deviation of the particle size distribution.

X_{Tri}	X_{HDA}	HDA:Tri	D_p (nm)	σ_g	k_{rxn} (cm^{-3} $molec.^{-1}$ $sec.^{-1}$)
100%	0	0	480, 434	1.29, 1.29	$6.74x10^{-4}$, $5.20x10^{-4}$
95%	5%	0.052	382, 309, 369, 268, 256	1.33, 1.37, 1.35, 1.38, 1.37	$6.43x10^{-4}$, $5.29x10^{-4}$, $6.21x10^{-4}$, $4.87x10^{-4}$, $3.92x10^{-4}$
80%	20%	0.25	279, 269, 255	1.39, 1.39, 1.38	$4.12x10^{-4}$, $5.33x10^{-4}$, $4.15x10^{-4}$
60%	40%	0.67	268, 253, 282, 247	1.53, 1.68, 1.67, 1.39	$3.16x10^{-4}$, $4.19x10^{-4}$, $3.73x10^{-4}$, $3.13x10^{-4}$
40%	60%	1.50	293, 271, 315	1.58, 1.56, 1.44	$2.47x10^{-4}$, $2.10x10^{-4}$, $2.15x10^{-4}$
15%	85%	5.67	266, 267, 265, 263	1.39, 1.42, 1.47, 1.39	$6.56x10^{-5}$, $6.79x10^{-5}$, $9.72x10^{-5}$, $6.26x10^{-5}$

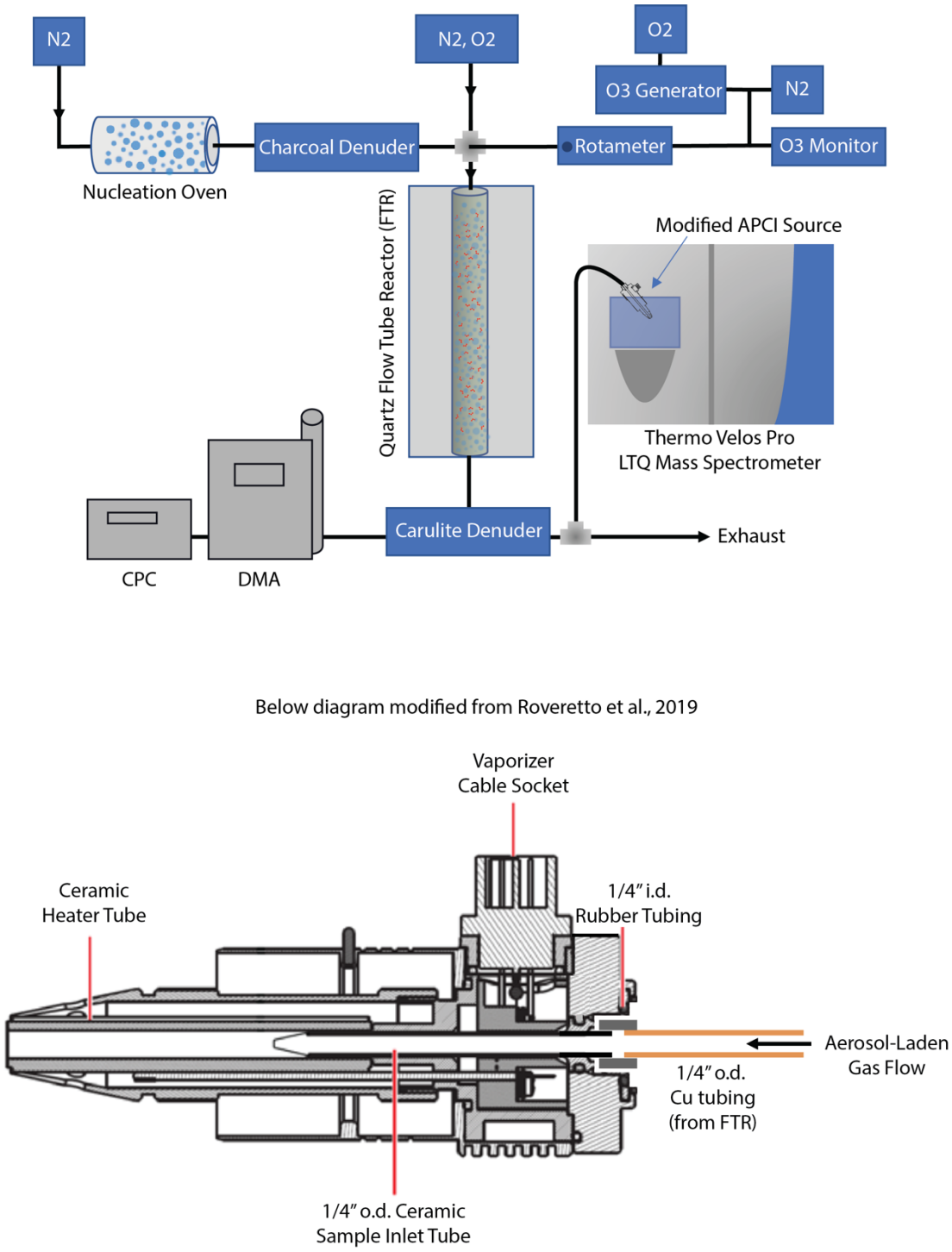

Figure 2.S1. (*Above*) Diagram of experimental setup for all flow tube studies reported in Table 2.S1 and the main text. (*Below*) Diagram of modified APCI source. Figure adapted from ThermoFisher LTQ Manual and the Supplementary Information of Roveretto et al., 2019.[14]

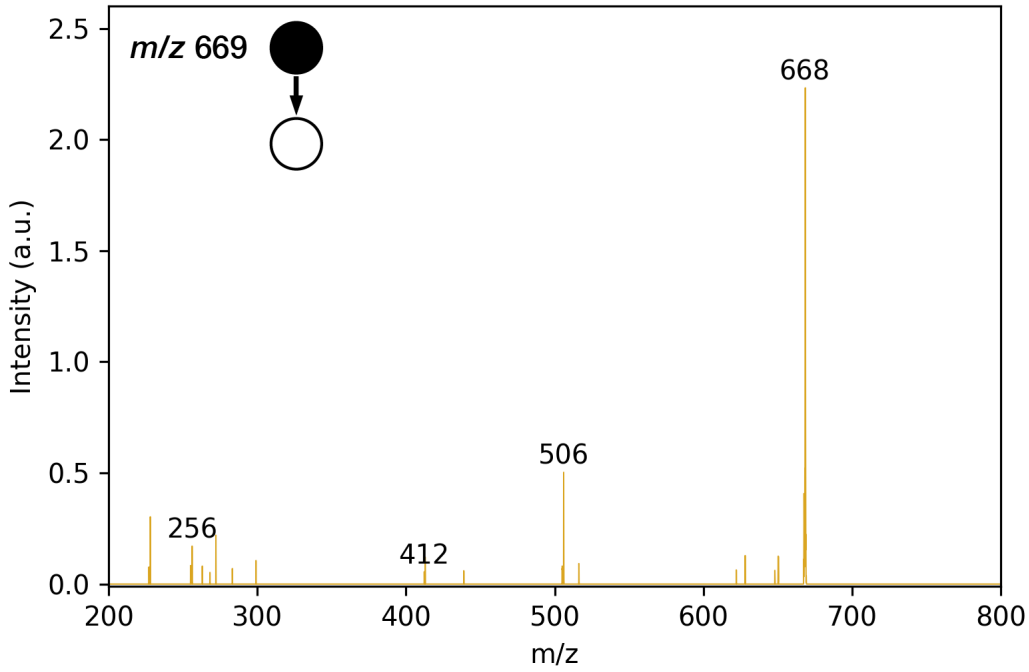

Figure 2.S2. Collision-induced Dissociation (CID) of m/z 669 cluster peak in negative ion mode, showing evolution of an HDA molecule (m/z 256) and a reduced fragment corresponding to the AAHP (m/z 412, MW 414).

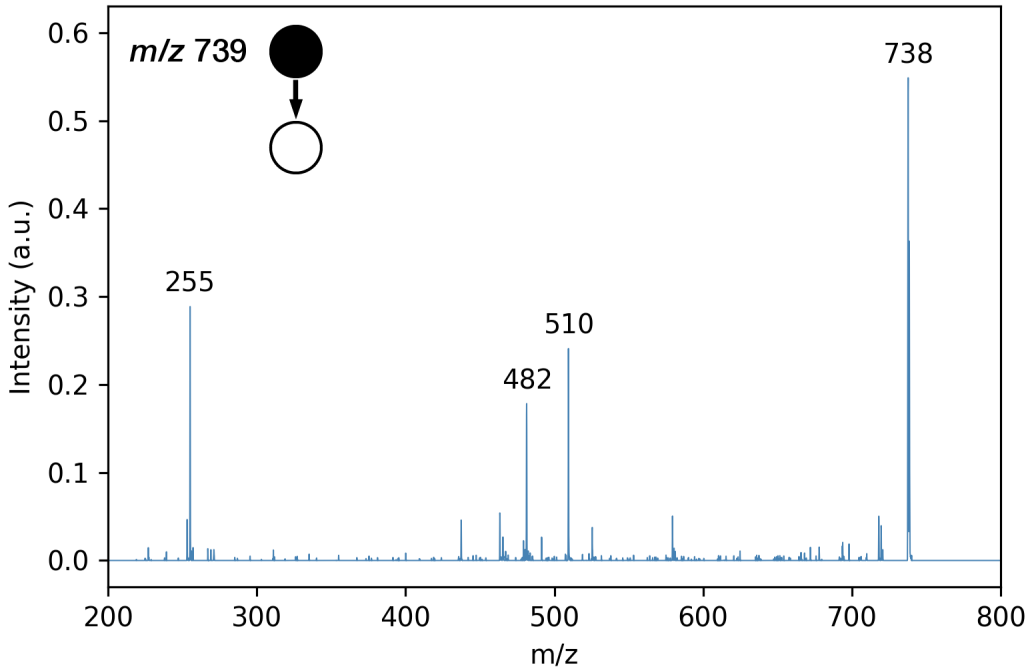

Figure 2.S3. Collision-induced Dissociation (CID) of m/z 739 cluster peak in negative ion mode, showing evolution of an HDA molecule (m/z 255) and a reduced fragment corresponding to the AAHP (m/z = 482, MW 484).

Table 2.S2. Reaction Mechanism.

Step No.	Reaction Step	Label (Analytical Model)	Value	Units	Reference (Notes)
	O_3 (g) -> O_3 (ads)		0.37	sec.$^{-1}$ (pseudo-first order, $[O_3]_g$=1ppm)	Calculated, see Ref.[32]
R1	O_3 (ads) + Tri -> sCI + C=O		2x10^{-16}	cm^3 molec.$^{-1}$ sec.$^{-1}$	[32]
R3	sCI -> RO· + ·OH	k_{VHP}	205	sec.$^{-1}$	[20]
R4	sCI -> RCOOH	k_{iso}	74	sec.$^{-1}$	[20]
R2	sCI + HDA -> AAHP	k_{AAHP}	2.1x10^{-19} *or* 1.0x10^{-13} (see text)	cm^3 molec.$^{-1}$ sec.$^{-1}$	This work
R5	sCI + H2O -> HHP	$k_{\mathrm{H2O}}[\mathrm{H_2O}]$	2.17	sec.$^{-1}$ (pseudo-first order, RH = 3%)	[20]
(R6)	sCI + RC=O -> SOZ	k_{SOZ}	n/a	n/a	[32] *(Not observed in this study)*
**	sCI + O_3 (ads) -> C=O		1.0x10^{-13}	cm^3 molec.$^{-1}$ sec.$^{-1}$	[32] *(Only in explicit simulations)*
R7	·OH + Tri -> Tri-R· + H_2O		2.0x10^{-11}	cm^3 molec.$^{-1}$ sec.$^{-1}$	[27,39]
R8a	Tri-R· + O_2 -> Tri-ROO·		1.1x10^{6}	sec.$^{-1}$ (pseudo-first order)	[40,41]
R9	2 Tri-ROO· -> 2 RC=O + ROH		4.0x10^{-15}	cm^3 molec.$^{-1}$ sec.$^{-1}$	[40]
R10	2 Tri-ROO· -> 2 Tri-RO· + O_2		1x10^{-16}	cm^3 molec.$^{-1}$ sec.$^{-1}$	[40]
R11	RO· + RH -> R· + ROH		1.66x10^{-15}	cm^3 molec.$^{-1}$ sec.$^{-1}$	[40]
R12	·OH + Tri -> Tri-OH·		6.60x10^{-11}	cm^3 molec.$^{-1}$ sec.$^{-1}$	[42]
R8b	Tri-OH· + O_2 -> β-ROO·		1.1x10^{6}	sec.$^{-1}$ (pseudo-first order)	[40,41]
R9b	2 β-ROO· -> 2 RC=O + ROH		4.0x10^{-15}	cm^3 molec.$^{-1}$ sec.$^{-1}$	[40]
R13	β-ROO· -> sCI + ROH		120	sec.$^{-1}$	[12]
R14a	C9_aldehyde (bulk) => C9_aldehyde_des		1x10^{4}	sec.$^{-1}$	*
R14b	C9_aldehyde_des => C9_aldehyde (g)		4.12x10^{5}	sec.$^{-1}$	**

Ozonolysis reaction mechanism adapted from Zeng & Wilson.[12]

* Estimated diffusion time across a 200 nm distance with a diffusion coefficient corresponding to that of Tri (D ≅ 7.15x10^{-7} cm^2 sec.$^{-1}$)

** Estimated from nonanal vapor pressure (~0.3 torr at 25 ˚C) according to the method described in the Supporting Information of Heine, et. al.[32]

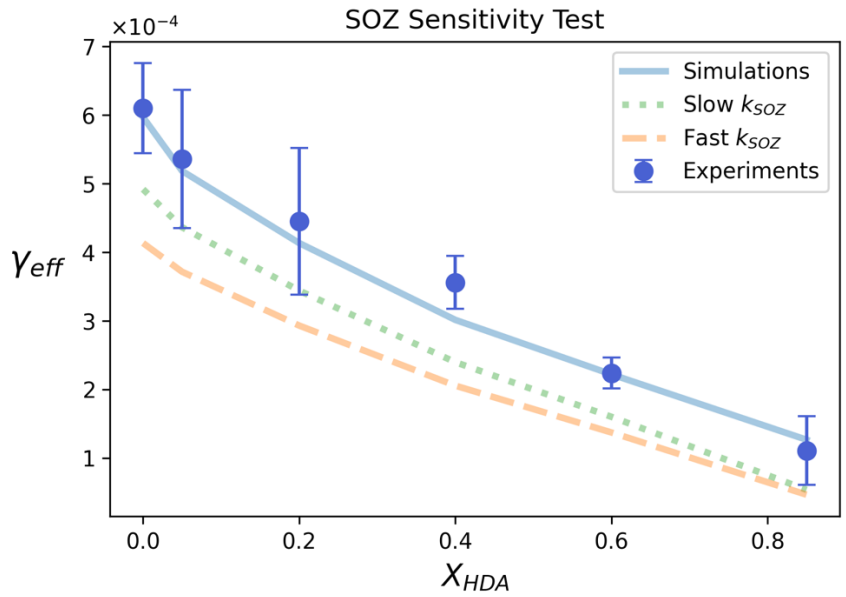

Figure 2.S5A. Effective uptake coefficients predicted by stochastic model, with sensitivity tests of SOZ formation pathway involving C14 aldehyde species. Two rate constants k_{SOZ} for reaction R6 were used: the rate coefficient used in stochastic kinetic simulations reported by Heine et. al[2] (denoted "Slow k_{SOZ}," 1.3×10^{-18} cm^3 $molec.^{-1}$ $sec.^{-1}$) and the rate reported used in flux-based simulations as reported by Müller et al.[10] (denoted "Fast k_{SOZ}," 10^{-15} cm^3 $molec.^{-1}$ $sec.^{-1}$).

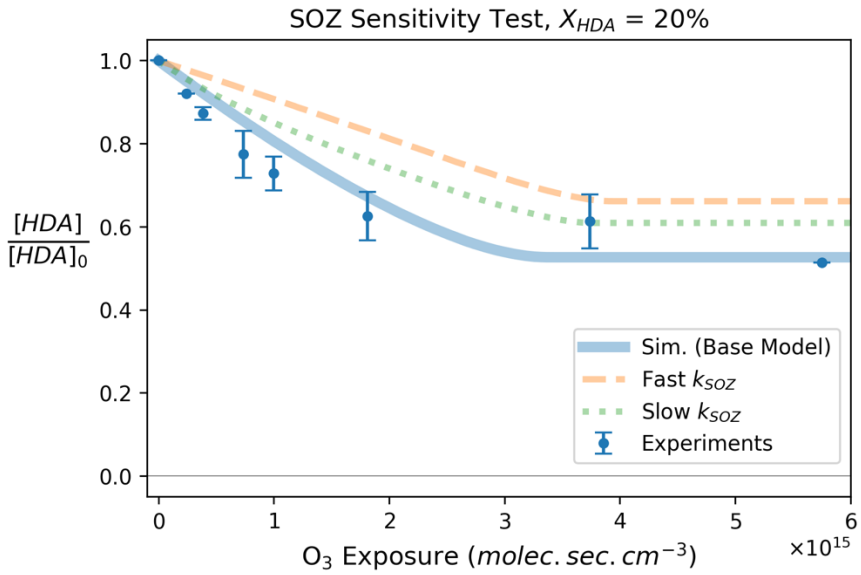

Figure 2.S5B. Simulated decay traces of HDA for 20% mole fraction HDA conditions, under the base model (Scenario A from main text, with no SOZ formation pathway) and SOZ formation sensitivity test scenarios described in 2.S5A above.

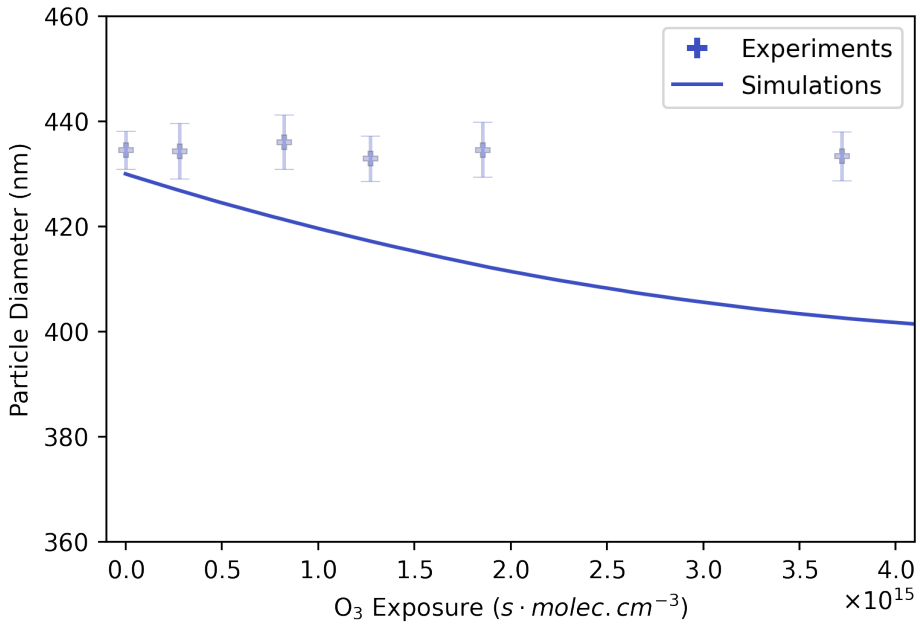

Figure 2.S6A. Diameter changes observed in experiments (points, error bars are ±1σ of three measurements) and those predicted by explicit kinetic simulation (solid lines) accounting for the evaporation of nonanal from neat Tri aerosol during ozonolysis.

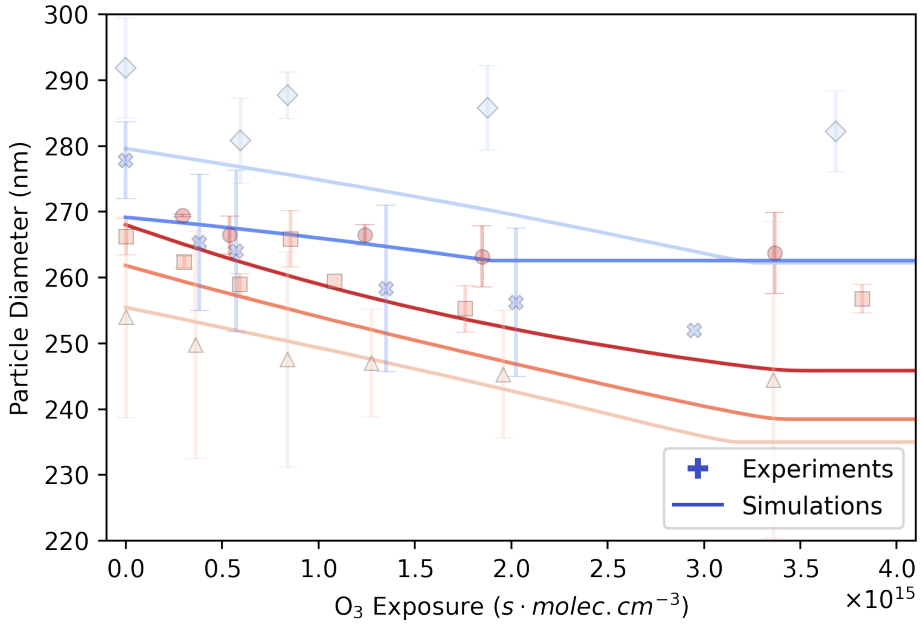

Figure 2.S6B. Diameter changes observed in experiments (points, error bars are ±1σ of at least three measurements) and those predicted by explicit kinetic simulation (solid lines) accounting for the evaporation of nonanal from aerosol binary mixtures of Tri/HDA having the mole fractions described in Table 2.S1.

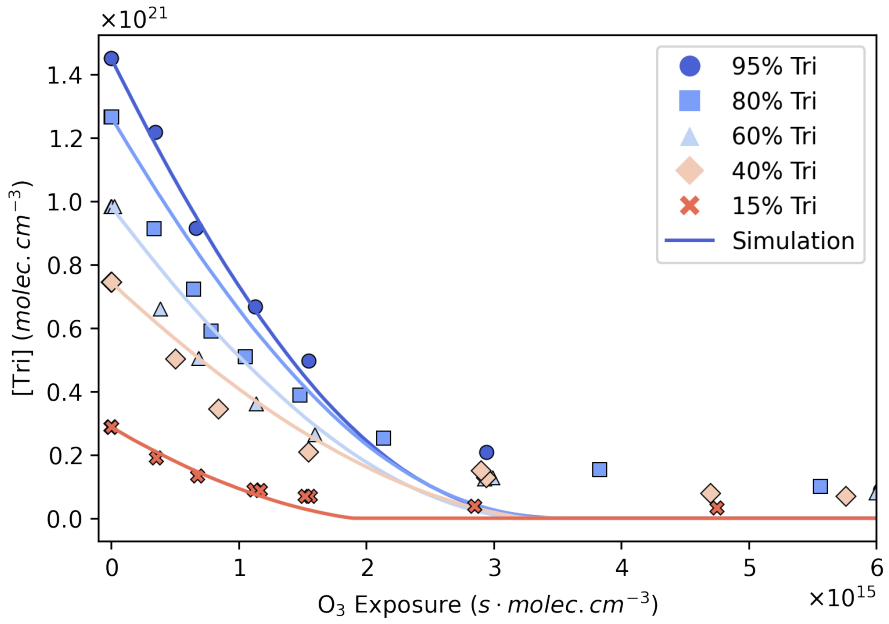

Figure 2.S7. Decay kinetics of Tri at each HDA mole fraction, comparing experimental observations (points) and explicit kinetic simulations under modeling Scenario A (solid lines), where $k_{AAHP} = 2.2x10^{-19}$ cm^3 molec.$^{-1}$ sec.$^{-1}$

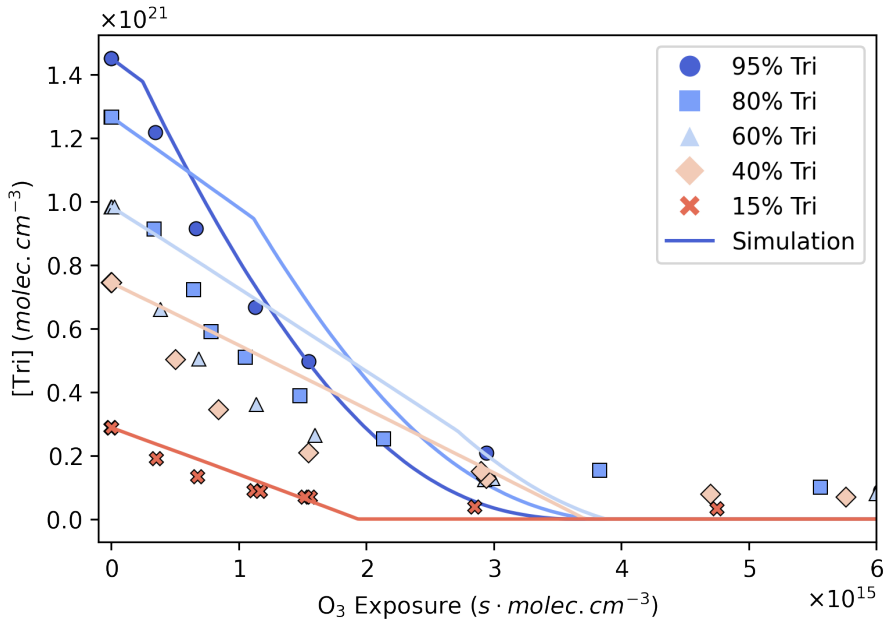

Figure 2.S8. Decay kinetics of Tri at each HDA mole fraction, comparing experimental observations (points) and explicit kinetic simulations under modeling Scenario B (solid lines). In Scenario B, k_{AAHP} is set to $1x10^{-13}$ cm^3 molec.$^{-1}$ sec.$^{-1}$ representing the diffusion limit in an organic matrix.

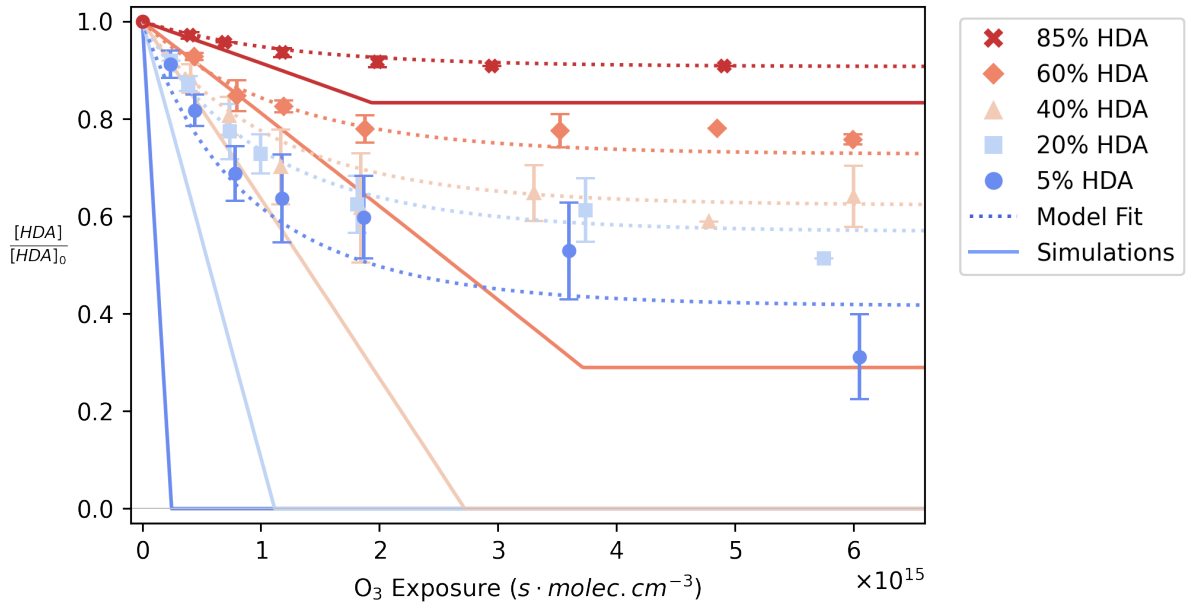

Figure 2.S9. The decay of the HDA signal intensity with ozone exposure, normalized to unreacted HDA signal for aerosols having HDA mole fractions (from top to bottom) of 85%, 60%, 40%, 20%, and 5%. Solid lines represent the results of explicit kinetic simulations under Scenario B, where k_{AAHP} = 1x10^{-13} cm3 molec.$^{-1}$ sec.$^{-1}$, as described in Section 4.3 of the main text.

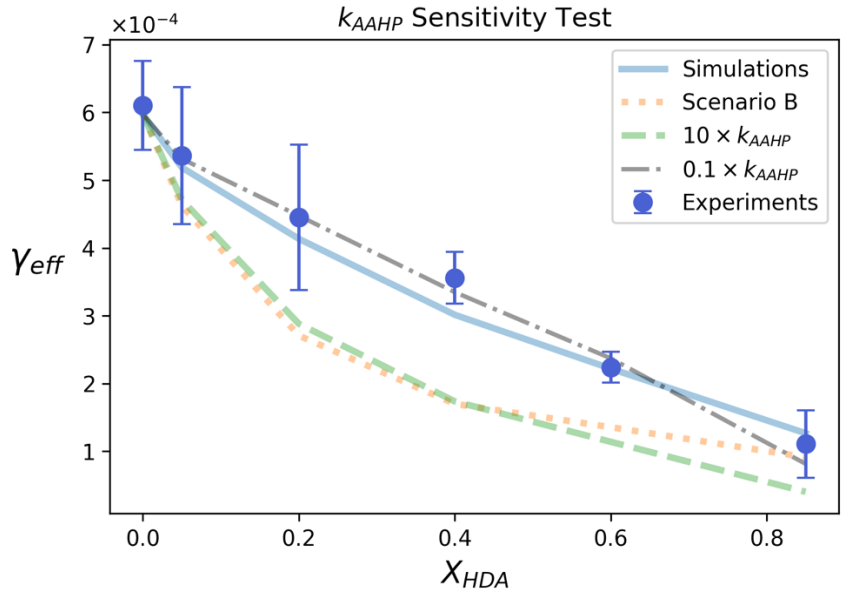

Figure 2.S10A. Effective uptake coefficients (γ_{eff}) predicted by the stochastic kinetic model under different modeling assumptions: Scenario A (base model, labeled "Simulations") and Scenario B as described in the main text, and values of k_{AAHP} one order of magnitude faster (10 x k_{AAHP}) and slower (0.1 x k_{AAHP}) than the optimal value adopted in the base model.

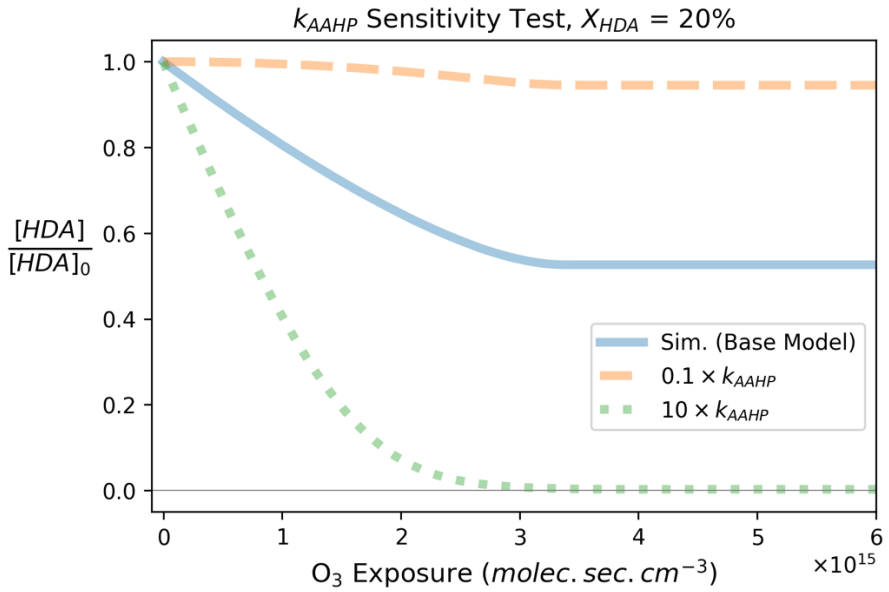

Figure 2.S10B. Decay traces of HDA for 20% mole fraction HDA conditions, under the base model (Scenario A from main text) and ±1 order of magnitude rate k_{AAHP} rate constants as described above, illustrating the sensitivity of the predicted HDA kinetics to the specification of k_{AAHP} in the model.

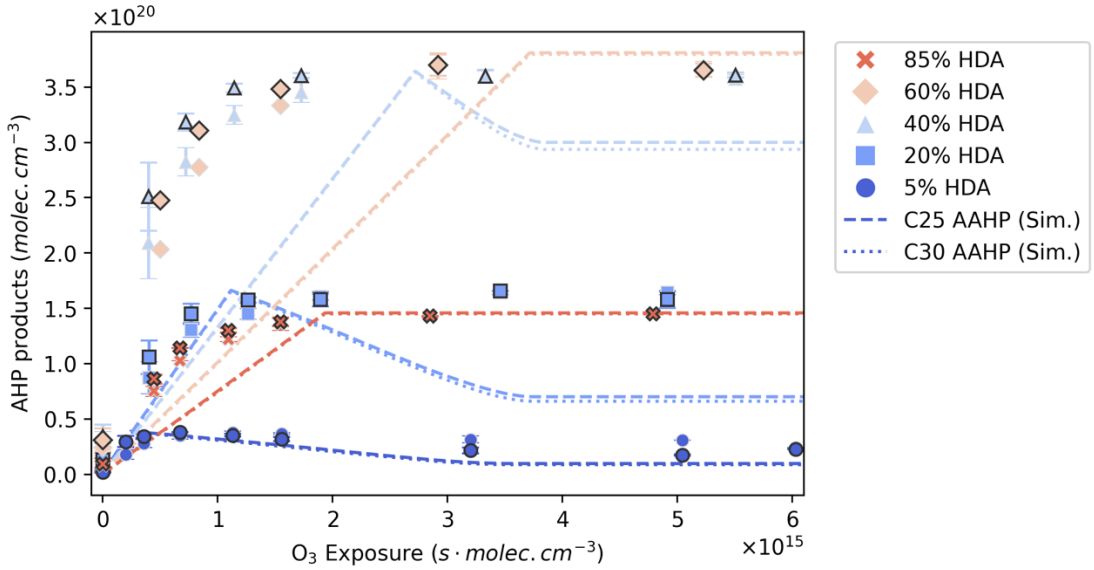

Figure 2.S11. The kinetic evolution of AAHP reaction products at each HDA mole fraction, comparing experimental observations (points) to the results of explicit kinetic simulations under Scenario B (solid lines). Observations correspond to integrated intensities of mass spectral peaks corresponding to AAHP products. Light-outlined points correspond to C25 AAHPs (m/z = 397 in positive ion mode and m/z = 669 in negative ion mode), and dark-outlined points correspond to C30 AAHPs (m/z = 467 in positive ion mode and m/z = 739 in negative ion mode); see Section 3.1. Experimental data is scaled to match the maximum product concentration of each simulation result.

2.7 References

(1) Taatjes, C. A. Criegee Intermediates: What Direct Production and Detection Can Teach Us About Reactions of Carbonyl Oxides. *Annu. Rev. Phys. Chem.* **2017**, *68* (1), 183–207. https://doi.org/10.1146/annurev-physchem-052516-050739.

(2) Taatjes, C. A.; Welz, O.; Eskola, A. J.; Savee, J. D.; Scheer, A. M.; Shallcross, D. E.; Rotavera, B.; Lee, E. P. F.; Dyke, J. M.; Mok, D. K. W.; Osborn, D. L.; Percival, C. J. Direct Measurements of Conformer-Dependent Reactivity of the Criegee Intermediate CH3CHOO. *Science* **2013**, *340* (6129), 177–180. https://doi.org/10.1126/science.1234689.

(3) Taatjes, C. A.; Welz, O.; Eskola, A. J.; Savee, J. D.; Osborn, D. L.; Lee, E. P. F.; Dyke, J. M.; Mok, D. W. K.; Shallcross, D. E.; Percival, C. J. Direct Measurement of Criegee Intermediate (CH 2 OO) Reactions with Acetone , Acetaldehyde , and Hexafluoroacetone. *Physical Chemistry Chemical Physics* **2012**, *14* (30), 10391–10400. https://doi.org/10.1039/C2CP40294G.

(4) Welz, O.; Eskola, A. J.; Sheps, L.; Rotavera, B.; Savee, J. D.; Scheer, A. M.; Osborn, D. L.; Lowe, D.; Murray Booth, A.; Xiao, P.; Anwar H. Khan, M.; Percival, C. J.; Shallcross, D. E.; Taatjes, C. A. Rate Coefficients of C1 and C2 Criegee Intermediate Reactions with Formic and Acetic Acid Near the Collision Limit: Direct Kinetics Measurements and Atmospheric Implications. *Angewandte Chemie* **2014**, *126* (18), 4635–4638. https://doi.org/10.1002/ange.201400964.

(5) Chhantyal-Pun, R.; Welz, O.; Savee, J. D.; Eskola, A. J.; Lee, E. P. F.; Blacker, L.; Hill, H. R.; Ashcroft, M.; Khan, M. A. H.; Lloyd-Jones, G. C.; Evans, L.; Rotavera, B.; Huang, H.; Osborn, D. L.; Mok, D. K. W.; Dyke, J. M.; Shallcross, D. E.; Percival, C. J.; Orr-Ewing, A. J.; Taatjes, C. A. Direct Measurements of Unimolecular and Bimolecular Reaction Kinetics of the Criegee Intermediate (CH_3)$_2$COO. *J. Phys. Chem. A* **2017**, *121* (1), 4–15. https://doi.org/10.1021/acs.jpca.6b07810.

(6) Katrib, Y.; Biskos, G.; Buseck, P. R.; Davidovits, P.; Jayne, J. T.; Mochida, M.; Wise, M. E.; Worsnop, D. R.; Martin, S. T. Ozonolysis of Mixed Oleic-Acid/Stearic-Acid Particles: Reaction Kinetics and Chemical Morphology. *J. Phys. Chem. A* **2005**, *109* (48), 10910–10919. https://doi.org/10.1021/jp054714d.

(7) Zhou, S.; Joudan, S.; Forbes, M. W.; Zhou, Z.; Abbatt, J. P. D. Reaction of Condensed-Phase Criegee Intermediates with Carboxylic Acids and Perfluoroalkyl Carboxylic Acids. *Environ. Sci. Technol. Lett.* **2019**, *6* (4), 243–250. https://doi.org/10.1021/acs.estlett.9b00165.

(8) Katrib, Y.; Martin, S. T.; Hung, H.-M.; Rudich, Y.; Zhang, H.; Slowik, J. G.; Davidovits, P.; Jayne, J. T.; Worsnop, D. R. Products and Mechanisms of Ozone Reactions with Oleic Acid for Aerosol Particles Having Core−Shell Morphologies. *J. Phys. Chem. A* **2004**, *108* (32), 6686–6695. https://doi.org/10.1021/jp049759d.

(9) Ziemann, P. J. Aerosol Products, Mechanisms, and Kinetics of Heterogeneous Reactions of Ozone with Oleic Acid in Pure and Mixed Particles. *Faraday Discuss.* **2005**, *130* (0), 469–490. https://doi.org/10.1039/B417502F.

(10) Gallimore, P. J.; Griffiths, P. T.; Pope, F. D.; Reid, J. P.; Kalberer, M. Comprehensive Modeling Study of Ozonolysis of Oleic Acid Aerosol Based on Real-Time, Online Measurements of Aerosol Composition. *Journal of Geophysical Research: Atmospheres* **2017**, *122* (8), 4364–4377. https://doi.org/10.1002/2016JD026221.

(11) Berkemeier, T.; Mishra, A.; Mattei, C.; Huisman, A. J.; Krieger, U. K.; Pöschl, U. Ozonolysis of Oleic Acid Aerosol Revisited: Multiphase Chemical Kinetics and Reaction Mechanisms. *ACS Earth Space Chem.* **2021**, *5* (12), 3313–3323. https://doi.org/10.1021/acsearthspacechem.1c00232.

(12) Zeng, M.; Wilson, K. R. Efficient Coupling of Reaction Pathways of Criegee Intermediates and Free Radicals in the Heterogeneous Ozonolysis of Alkenes. *J. Phys. Chem. Lett.* **2020**, *11* (16), 6580–6585. https://doi.org/10.1021/acs.jpclett.0c01823.

(13) Pankow, J. F. An Absorption Model of Gas/Particle Partitioning of Organic Compounds in the Atmosphere. *Atmospheric Environment* **1994**, *28* (2), 185–188. https://doi.org/10.1016/1352-2310(94)90093-0.

(14) Roveretto, M.; Li, M.; Hayeck, N.; Brüggemann, M.; Emmelin, C.; Perrier, S.; George, C. Real-Time Detection of Gas-Phase Organohalogens from Aqueous Photochemistry Using Orbitrap Mass Spectrometry. *ACS Earth Space Chem.* **2019**, *3* (3), 329–334. https://doi.org/10.1021/acsearthspacechem.8b00209.

(15) Adas, F.; Picart, D.; Berthou, F.; Simon, B.; Amet, Y. Liquid Chromatography–Mass Spectrometry and Gas Chromatography–Mass Spectrometry of v- and (v-1)-Hydroxylated Metabolites of Elaidic and Oleic Acids in Human and Rat Liver Microsomes. *J. Chromatogr. B* **1998**, 12.

(16) Byrdwell, W. C. Atmospheric Pressure Chemical Ionization Mass Spectrometry for Analysis of Lipids. *Lipids* **2001**, *36* (4), 327–346. https://doi.org/10.1007/s11745-001-0725-5.

(17) Bell, S. E.; Ewing, R. G.; Eiceman, G. A.; Karpas, Z. Atmospheric Pressure Chemical Ionization of Alkanes, Alkenes, and Cycloalkanes. *J. Am. Soc. Mass Spectrom.* **1994**, *5* (3), 177–185. https://doi.org/10.1016/1044-0305(94)85031-3.

(18) Zeng, M.; Heine, N.; Wilson, K. R. Evidence That Criegee Intermediates Drive Autoxidation in Unsaturated Lipids. *PNAS* **2020**. https://doi.org/10.1073/pnas.1920765117.

(19) Vereecken, L. The Reaction of Criegee Intermediates with Acids and Enols. *Phys. Chem. Chem. Phys.* **2017**, *19* (42), 28630–28640. https://doi.org/10.1039/C7CP05132H.

(20) Vereecken, L.; Novelli, A.; Taraborrelli, D. Unimolecular Decay Strongly Limits the Atmospheric Impact of Criegee Intermediates. *Phys. Chem. Chem. Phys.* **2017**, *19* (47), 31599–31612. https://doi.org/10.1039/C7CP05541B.

(21) Enami, S. Fates of Organic Hydroperoxides in Atmospheric Condensed Phases. *J. Phys. Chem. A* **2021**. https://doi.org/10.1021/acs.jpca.1c01513.

(22) Zeng, M.; Wilson, K. R. Experimental Evidence That Halogen Bonding Catalyzes the Heterogeneous Chlorination of Alkenes in Submicron Liquid Droplets. *Chem. Sci.* **2021**, *12* (31), 10455–10466. https://doi.org/10.1039/D1SC02662C.

(23) Wilson, K. R.; Smith, J. D.; Kessler, S. H.; Kroll, J. H. The Statistical Evolution of Multiple Generations of Oxidation Products in the Photochemical Aging of Chemically Reduced Organic Aerosol. *Phys. Chem. Chem. Phys.* **2012**, *14* (4), 1468–1479. https://doi.org/10.1039/C1CP22716E.

(24) Smith, J. D.; Kroll, J. H.; Cappa, C. D.; Che, D. L.; Liu, C. L.; Ahmed, M.; Leone, S. R.; Worsnop, D. R.; Wilson, K. R. The Heterogeneous Reaction of Hydroxyl Radicals with Sub-Micron Squalane Particles: A Model System for Understanding the Oxidative Aging of Ambient Aerosols. *Atmos. Chem. Phys.* **2009**, 14.

(25) Liu, C.-L.; Smith, J. D.; Che, D. L.; Ahmed, M.; Leone, S. R.; Wilson, K. R. The Direct Observation of Secondary Radical Chain Chemistry in the Heterogeneous Reaction of Chlorine Atoms with Submicron Squalane Droplets. *Phys. Chem. Chem. Phys.* **2011**, *13* (19), 8993. https://doi.org/10.1039/c1cp20236g.

(26) Wells, J. R.; Morrison, G. C.; Coleman, B. K.; Spicer, C.; Dean, S. W. Kinetics and Reaction Products of Ozone and Surface-Bound Squalene. *J. ASTM Int.* **2008**, *5* (7), 101629. https://doi.org/10.1520/JAI101629.

(27) Atkinson, R. Estimations of OH Radical Rate Constants from H-Atom Abstraction from C–H and O–H Bonds over the Temperature Range 250-1000 K. *International Journal of Chemical Kinetics* **1986**, *18* (5), 555–568. https://doi.org/10.1002/kin.550180506.

(28) Campbell, S. J.; Wolfer, K.; Gallimore, P. J.; Giorio, C.; Häussinger, D.; Boillat, M.-A.; Kalberer, M. Characterization and Quantification of Particle-Bound Criegee Intermediates in Secondary Organic Aerosol. *Environ. Sci. Technol.* **2022**, *56* (18), 12945–12954. https://doi.org/10.1021/acs.est.2c04101.

(29) Zhang, X.; Barraza, K. M.; Beauchamp, J. L. Cholesterol Provides Nonsacrificial Protection of Membrane Lipids from Chemical Damage at Air–Water Interface. *PNAS* **2018**, *115* (13), 3255–3260. https://doi.org/10.1073/pnas.1722323115.

(30) Wagner, J. P. Criegee Intermediates in Autoxidation Reactions: Mechanistic Considerations. *J. Phys. Chem. A* **2021**, *125* (1), 406–410. https://doi.org/10.1021/acs.jpca.0c09971.

(31) Hinsberg, W. D.; Houle, F. A. Kinetiscope – A Stochastic Kinetics Simulator, 2020. http://hinsberg.net/kinetiscope.

(32) Heine, N.; Houle, F. A.; Wilson, K. R. Connecting the Elementary Reaction Pathways of Criegee Intermediates to the Chemical Erosion of Squalene Interfaces during Ozonolysis. *Environ. Sci. Technol.* **2017**, *51* (23), 13740–13748. https://doi.org/10.1021/acs.est.7b04197.

(33) A. Wiegel, A.; R. Wilson, K.; D. Hinsberg, W.; A. Houle, F. Stochastic Methods for Aerosol Chemistry: A Compact Molecular Description of Functionalization and Fragmentation in the Heterogeneous Oxidation of Squalane Aerosol by OH Radicals. *Physical Chemistry Chemical Physics* **2015**, *17* (6), 4398–4411. https://doi.org/10.1039/C4CP04927F.

(34) Müller, M.; Mishra, A.; Berkemeier, T.; Hausammann, E.; Peter, T.; Krieger, U. K. Electrodynamic Balance–Mass Spectrometry Reveals Impact of Oxidant Concentration on Product Composition in the Ozonolysis of Oleic Acid. *Phys. Chem. Chem. Phys.* **2022**, *24* (44), 27086–27104. https://doi.org/10.1039/D2CP03289A.

(35) Kwamena, N.-O. A.; Staikova, M. G.; Donaldson, D. J.; George, I. J.; Abbatt, J. P. D. Role of the Aerosol Substrate in the Heterogeneous Ozonation Reactions of Surface-Bound PAHs. *J. Phys. Chem. A* **2007**, *111* (43), 11050–11058. https://doi.org/10.1021/jp075300i.

(36) Renbaum, L. H.; Smith, G. D. Artifacts in Measuring Aerosol Uptake Kinetics: The Roles of Time, Concentration and Adsorption. *Atmospheric Chemistry and Physics* **2011**, *11* (14), 6881–6893. https://doi.org/10.5194/acp-11-6881-2011.

(37) Long, B.; Cheng, J.-R.; Tan, X.; Zhang, W. Theoretical Study on the Detailed Reaction Mechanisms of Carbonyl Oxide with Formic Acid. *Journal of Molecular Structure: THEOCHEM* **2009**, *916* (1–3), 159–167. https://doi.org/10.1016/j.theochem.2009.09.028.

(38) Pryor, W. A.; Smith, K. Viscosity Dependence of Bond Homolysis. Qualitative and Semiquantitative Test for Cage Return. *J. Am. Chem. Soc.* **1970**, *92* (18), 5403–5412. https://doi.org/10.1021/ja00721a019.

(39) Vereecken, L.; Peeters, J. H-Atom Abstraction by OH-Radicals from (Biogenic) (Poly)Alkenes: C–H Bond Strengths and Abstraction Rates. *Chemical Physics Letters* **2001**, *333* (1), 162–168. https://doi.org/10.1016/S0009-2614(00)01347-6.

(40) Denisov, E. T.; Afanas'ev, I. B. *Oxidation and Antioxidants in Organic Chemistry and Biology.*; Taylor & Frances: Oxford, 2005.

(41) Houle, F. A.; Hinsberg, W. D.; Wilson, K. R. Oxidation of a Model Alkane Aerosol by OH Radical: The Emergent Nature of Reactive Uptake. *Phys. Chem. Chem. Phys.* **2015**, *17* (6), 4412–4423. https://doi.org/10.1039/C4CP05093B.

(42) Peeters, J.; Boullart, W.; Pultau, V.; Vandenberk, S.; Vereecken, L. Structure−Activity Relationship for the Addition of OH to (Poly)Alkenes: Site-Specific and Total Rate Constants. *J. Phys. Chem. A* **2007**, *111* (9), 1618–1631. https://doi.org/10.1021/jp066973o.

Chapter 3. The Temperature-Dependent Kinetics of Criegee Intermediates During Ozonolysis

Figures and content in this chapter are adapted from "Reynolds, R.S.; Wilson, K.R. A Balance of Unimolecular and Bimolecular Pathways Control the Temperature-Dependent Kinetics of Ozonolysis in Aerosols. J. Phys. Chem. A. **2024, Under review."*

3.1 Introduction

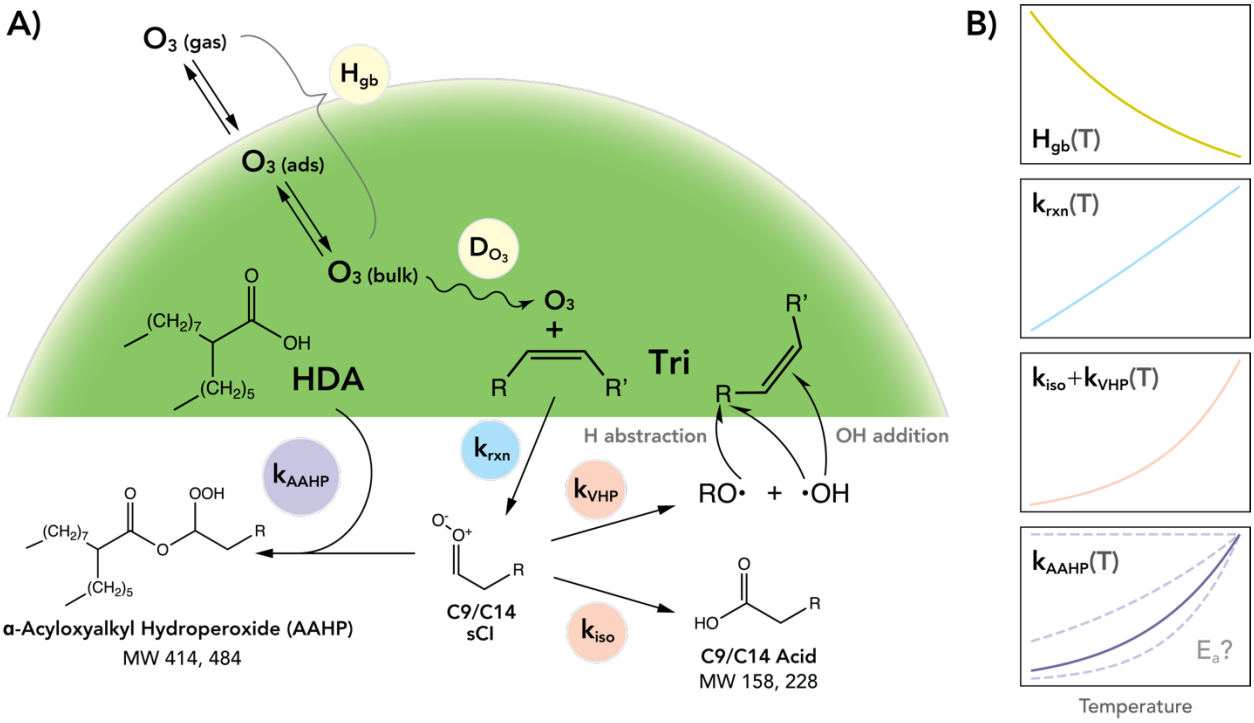

Figure 3.1. (A) Illustrated mechanism of the key chemical reactions considered in this study. (B) Depictions of the temperature dependence of the most important parameters controlling the heterogeneous reaction kinetics in this study.

Reactions between trace gases and aerosol particles are controlled by multiple physical and chemical processes, as illustrated in Figure 3.1A. These include adsorption and desorption of the trace gas from the particle surface, the transfer of the trace gas from the surface into the particle bulk and the reaction rate of the trace gas with particle-phase reactants.[1–3] The rates of each of these individual steps depend on the identity of the trace gas and the chemical composition of the particle, as well as its physical properties such as viscosity and phase state.[4–7] The coupling of these system-dependent transport and reaction processes can make predictions of chemical kinetics in these systems difficult and computationally intensive, especially when the reaction mechanism in the particle phase is complex.[8,9] In particular, reactions involving organic molecules, such as the ozonolysis of alkenes, can initiate a wide variety of secondary reaction steps and reaction products,

driven by short-lived reactive intermediates embedded in complex reaction networks.[10–13] Thus, it is desirable to find a way of disentangling these various processes in order to understand how these complex kinetics dynamically evolve during the course of reaction.

While many measurements of heterogeneous kinetics in aerosols have been conducted at a single ambient temperature, the number of variable-temperature measurements has grown in recent years.[7,14,15] These studies are often motivated by an effort to better understand aging kinetics of organic aerosol in cold regions of the atmosphere, such as in the artic, where organic aerosols constitute up to 40% of observed particulate mass.[16,17] However, the key parameters controlling the heterogeneous reactivity often have differing responses to temperature, as illustrated in Figure 3.1B. For example, while gas solubility in liquids, described by the Henry's law constant between gas and bulk phases, $\mathbf{H_{gb}}$ in Fig. 3.1, tends to increase with decreasing temperature,[18–20] the primary ozonolysis step, described by the rate constant ($\mathbf{k_{rxn}}$, Fig. 3.1) is expected to exhibit a positive temperature dependence due to the activation energy for the reaction.[21] Additionally, unimolecular chemical reactions of the stabilized Criegee Intermediates (hereafter referred to as sCI) generated by ozonolysis, such as isomerization to form carboxylic acids ($\mathbf{k_{iso}}$, Fig. 3.1B) or decomposition into an alkoxy and an OH radical ($\mathbf{k_{VHP}}$, Fig. 3.1B), have rates that depend strongly on both temperature and the molecular structure of the intermediate.[22–25] Although there are many experimental or theoretical estimates for the temperature dependence of many of the rate constants in the gas-phase listed above, there is a need for more precise kinetic measurements in the particle phase as emphasized in recent work.[8,26] In particular, the reaction rate constant for sCI and carboxylic acids in the particle phase, denoted here by $\mathbf{k_{AAHP}}$, has been shown to be significantly slower in the particle phase than in the gas phase.[27–29] This result could be an indication of an energetic barrier to reaction in the condensed phase, in contrast to the barrierless mechanism in the gas phase.[28,29] Temperature-dependent measurements of this rate can aid in uncovering the mechanism of this reaction, as well as inform estimates of the branching ratio between bimolecular and unimolecular reactions of the sCI, which is key to understanding ozonolysis kinetics in model aerosols.

To better understand these facets of heterogeneous reactions in the particle phase, this study builds on previous work by examining the ozonolysis kinetics of organic aerosols composed of binary mixtures of *cis*-9-Tricosene (**Tri**, $C_{23}H_{46}$) and 2-hexyldecanoic acid (**HDA**, $C_{16}H_{32}O_2$) as a function of temperature (253 to 293 K). This study aims to quantify the contributions of the competing processes outlined above to the total reactivity in this heterogeneous reaction, and to identify the relative importance of reactant transport and primary and secondary chemical reactions to the temperature-dependent behavior of the reactive uptake of ozone. To this end, a detailed reaction-diffusion model is developed to compare with the experimental results, first for the pure alkene aerosol to probe the effects of temperature on the network of secondary reactions initiated by ozonolysis, and second in the presence of varying amounts of HDA, to probe the temperature-dependent branching ratio between bimolecular and unimolecular sinks of particle-bound sCI. Where necessary, estimates are made of thermodynamic parameters, such as the activation energy (E_a) for the reaction of sCI with a carboxylic acid ($\mathbf{k_{AAHP}}$), with the parameter choice evaluated against experimental results. Together, experimental and modeling results reveal how the observed kinetics are the result of competitions between unimolecular and bimolecular reaction steps, which are in a delicate balance across the temperature range studied here. These results highlight the crucial role that reactive intermediates can play in aerosol aging at low temperatures.

3.2 Methods

3.2.A Experimental Setup

The experimental setup is modified slightly from that described in previous work and is diagrammed in detail in Figure 3.S1 (Supporting Information). Briefly, a jacketed quartz flow tube reactor is used to measure the ozonolysis kinetics on aerosols composed of binary mixtures of Tri and HDA. The temperature of the flow tube is controlled by a recirculating chiller (VWR, AD15R), which flows a mixture of equal parts water and ethylene glycol (Macron Fine Chemicals) through the outer jacket of the flow tube. Experiments are conducted at temperatures in 10 degree intervals from 253 K to 293 K as measured by the chiller's internal thermostat. The reactor temperature is allowed to equilibrate to within ±1˚C of the nominal temperature before each experiment.

Particles are generated *via* homogeneous nucleation by passing 0.3 SLM room temperature (~20˚C) dry nitrogen through heated organic vapor in a Pyrex tube inserted into an annular furnace (Carbolite) held at 115–120 ˚C. A narrow particle size is then selected from the resulting polydisperse particle distribution using an Aerodynamic Aerosol Classifier (AAC, Cambustion Instruments) set to 370 nm diameter, with a sheath flow of 3 LPM. To allow the particle-laden flow additional time to equilibrate to the temperature, the flow is passed through a length of ½ in. copper tubing submerged in the bath of the chiller prior to entering the flow tube. The particle size distribution is measured at the exit of the flow tube before and after reaction using a Scanning Mobility Particle Spectrometer (SMPS) comprised of a condensation particle counter (CPC 3025A, TSI Inc.) and a differential mobility analyzer (DMA 3071, TSI Inc.).

3.2.B. Mass Spectrometry

Mass spectra were recorded using Vacuum Ultraviolet (VUV) photoionization Aerosol Mass Spectrometer (VUV-AMS) endstation at the Chemical Dynamics Beamline (9.0.2) at the Advanced Light Source, Berkeley, CA. The instrument has been described in detail previously,[30] and a schematic overview is available in the supporting information (Figure 3.S2). Spectra were obtained at photon energies between 9.8–10.2 eV, above the photoionization threshold for both Tri and HDA. Aerosols sampled by the AMS were flash vaporized at a temperature of 145–155 ˚C before photoionization, and each spectrum collected is the average of at least 10,000 detector sweeps. The mass spectrum of the unreacted aerosol is shown in Figure 3.2. Photoionization of Tri primarily produces a molecular ion at m/z = 322, as well as a series of lower-intensity peaks corresponding to fragments produced by alkyl loss. Photoionization of HDA at the same photon energy yields a molecular ion at m/z = 256, however the branched structure of HDA facilitates further fragmentation at the carbon adjacent to its carboxylic acid head group. The resulting fragments correspond to loss either of the hexyl group, yielding a 10-carbon fragment with m/z = 172, or the octyl group, resulting in an 8-carbon fragment at m/z = 144. Reaction kinetics are monitored as a function of ozone exposure by varying the ozone concentration in the flow tube and recording the changes in integrated intensity of the reactant and product peaks from the VUV-AMS.

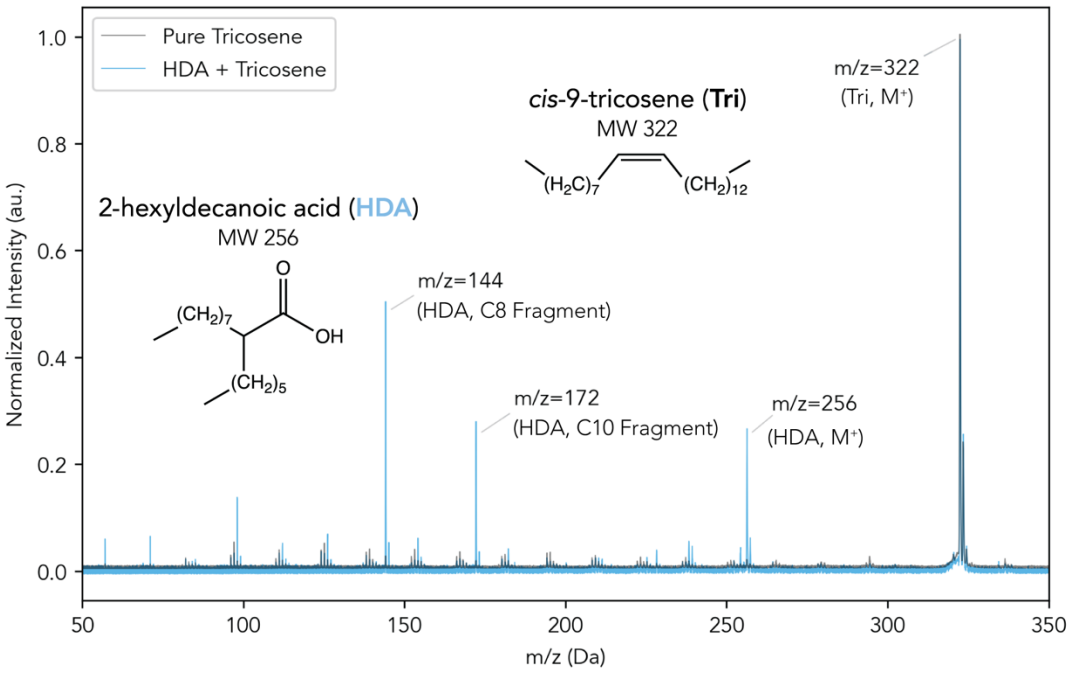

Figure 3.2. VUV Photoionization spectrum of pure Tri aerosols (black spectrum) or mixed HDA and Tri aerosols (blue spectrum) before ozone exposure. Intensities are normalized to the molecular ion of Tri (*m/z* = 322), apparent in both spectra. Labeled peaks in the blue spectrum (*m/z* = 256, 172, and 144) are identified as unique to HDA, with peak assignments described in the text.

3.2.C. Kinetic Model Description

Due to the complexity of the coupled chemical reaction and transport network described in Figure 3.1A, a reaction-diffusion model was developed to simulate the expected temperature-dependent heterogeneous kinetics of the ozonolysis reaction in this system. This is done using Kinetiscope (https://hinsberg.net/kinetiscope/), a stochastic reaction-diffusion simulator.[31] Previously, Kinetiscope has been used to model this reaction at room temperature using a single, well-mixed compartment description.[29,32] In order to properly model the temperature dependence of the chemical transport processes, the previous framework has been adapted to a two-compartment description with explicit surface and bulk regions connected by diffusion pathways, similar to the framework described by Willis and Wilson.[9]

Following the approach of previous work modeling aqueous droplets,[3,9] the adsorption, desorption and solvation kinetics of ozone at the gas-particle interface are determined according to a coupled-equilibrium model, with the equilibrium constants (*e.g.*, H_{gb}) constrained by experimental measurements and the results of Molecular Dynamics (MD) simulations, as described in the *Supporting Information*. Rate constants for chemical reaction steps are assumed to have Arrhenius-like temperature dependence, with parameters taken from experimental measurements (or those of the analogous gas-phase reactions) given in literature. In the case of the

primary ozonolysis rate (k_{rxn}), a solution-phase measurement is used to determine the magnitude of the reaction rate constant at room temperature, while the activation energy is chosen within a range constrained by tabulated gas phase data, as described in the *Supporting Information*. The activation energy (E_a) for k_{AAHP} is a key parameter in need of constraint; in this study, several possible values of E_a are chosen and evaluated for their agreement with the experimental data describing the decay of HDA, as discussed in subsequent sections. The complete reaction mechanism employed in the final simulations, including the Arrhenius parameters describing the rate constant for each step, is given in Table S1 (*Supporting Information*).

3.3 Results

3.3.A. Tri Decay Kinetics

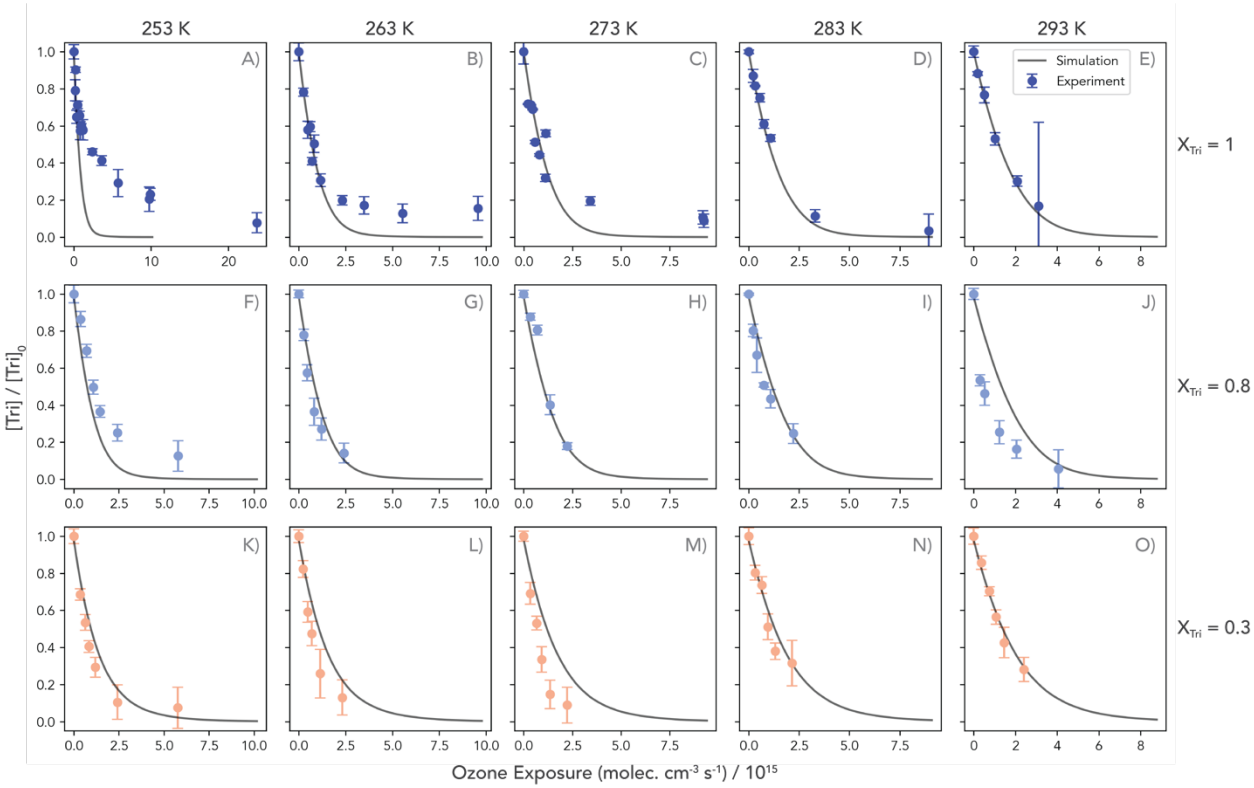

Figure 3.3. Decay kinetics of Tri (*m/z* = 322) from VUV-AMS experiments and kinetic simulations across all experimental conditions of this study, normalized to initial Tri signal intensity (experiments, points) or concentration (simulations, lines). Initial mole fractions of Tri (X_{Tri}) are constant across rows, as labeled at the right hand side of the figure: X_{Tri}=1 (panels A–E), X_{Tri}=0.8 (F–J), and X_{Tri}=0.3 (K–O). Data points are colored according to initial X_{Tri} for additional emphasis. Columns denote constant temperatures, as labeled at the top of the figure. Error bars on points correspond to relative (percent) error of ±1 standard deviation from the mean of the signal intensity measured by the VUV-AMS.

The normalized decay kinetics of Tri vs. ozone exposure (i.e. [O_3] x time) are shown in Figure 3.3. As seen from the changing scale of the ozone exposure axis, the rate of decay of Tri generally increases with decreasing temperature (proceeding right to left along a row), and with

increasing initial X_{Tri} (proceeding from the top to the bottom panel). Lines represent the output of kinetic simulations.

For pure Tri aerosols (panels A-E in Figure 3.3), an initial region of decay is apparent at small ozone exposures and generally in agreement with the simulated kinetics, with several exceptions. A fraction of Tri remaining unreacted begins to be apparent below 273 K (panels A-C), and at 253 K (panel A), and a distinct shift towards slower decay kinetics can be observed at large exposures. This change in kinetics is taken as an indication of the onset of a phase transition in the aerosols that is induced during the course of reaction. Since the freezing point of Tri has been reported as -0.6 ˚C (272.5 K) by FTIR measurements, the onset of this apparent phase change below 263 K does not directly correspond to the bulk freezing transition.[33] However, supercooling of organic aerosols by more than 30˚C below the bulk freezing points of their constituents has been observed in other studies where particles are produced *via* homogeneous nucleation.[34,35,7] As such, it seems likely that the biexponential behavior observed in panel A is the onset of a phase transition, and, by extension, that the kinetics observed at 263 K and above (panels B-E) correspond to supercooled liquid particles. Similarly, as the bulk freezing temperature of HDA is reported to be 18 ˚C (291 K),[36] the onset of bi-exponential kinetics in panel F, where X_{Tri}=0.8, could also correspond to the onset of freezing of supercooled aerosol particles, accounting for the discrepancy between simulation and experiment at 253 K. Similar behavior was observed by Katrib *et al.* for room temperature ozonolysis of mixed oleic and stearic acid particles, and was attributed to the complex phase behavior of the mixture of the two lipids.[35] Composition- and temperature-dependent phase behavior, such as differing particle morphologies forming at low temperatures due to the interaction of the aerosol components, could be responsible for the discrepancy between the trends in kinetics for X_{Tri}=0.8 and X_{Tri}=0.3.

3.3.A.i. Effective Uptake Coefficients (γ_{eff}) vs. Temperature

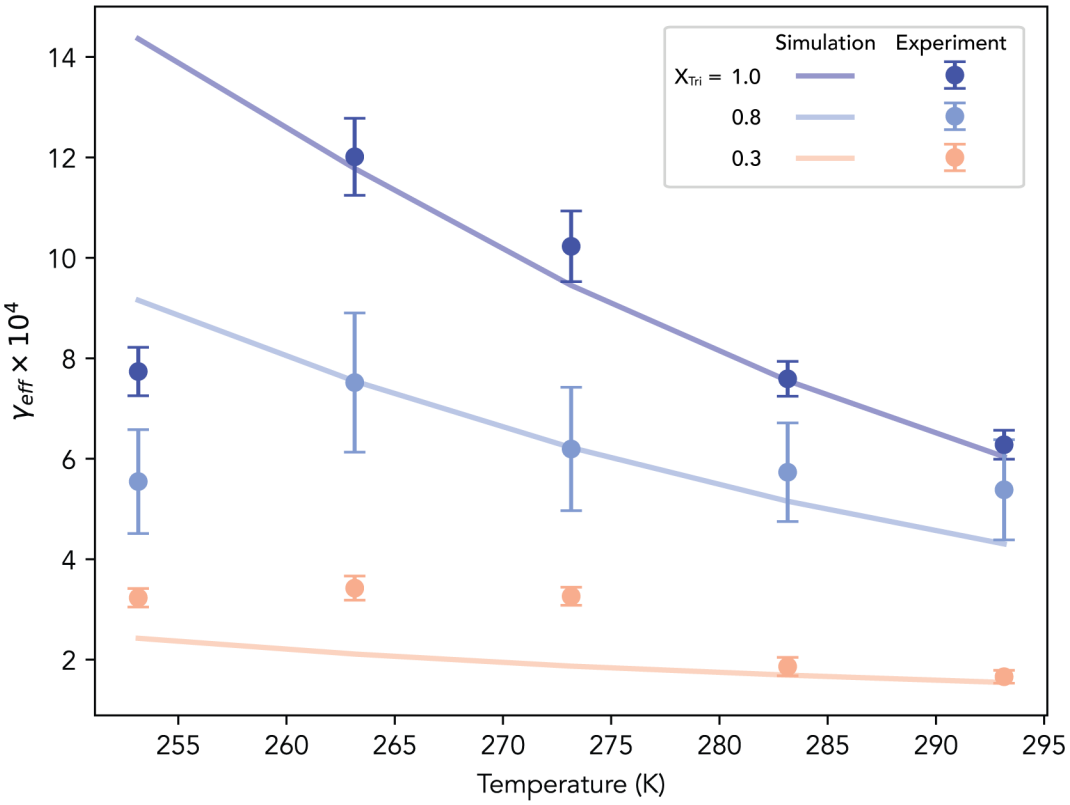

Figure 3.4. Effective uptake coefficients (γ_{eff}) of Tri calculated from experiment (points) and simulation (lines) as a function of temperature. Initial X_{Tri} is denoted by color, decreasing top to bottom, from X_{Tri}=1 to X_{Tri}=0.3. Error bars on points correspond to Tri decay constant fits assuming ±1 standard deviation from the mean.

In order to evaluate the kinetics of Tri decay quantitatively across experimental conditions, the effective uptake coefficient (γ_{eff}) was calculated for each experiment,

$$\gamma_{eff} = \frac{4 \cdot D_p [Tri]_0 k_{obs}}{6\bar{c}} \cdot X_{Tri} \qquad Eq.\,(3.1)$$

where D_p is the particle diameter in cm, $[Tri]_0$ is the number density of liquid Tri in molec. cm^{-3}. X_{Tri} is the initial mole fraction of Tri in the aerosol, and $\bar{c}$ is the mean speed of ozone in cm s^{-1}. The initial region of each Tri decay curve in Figure 3.3 was fit by an exponential function, from which the decay constant k_{obs} (in cm^3 molec.$^{-1}$ s^{-1}) is obtained from each experiment. The resulting trends in γ_{eff} for each experimental condition are shown in Figure 3.4.

As discussed previously,[29,32] γ_{eff} differs from a traditional uptake coefficient measured *via* the consumption of a gas-phase reactant as it includes all reactions that consume the condensed-phase reactant, including secondary radical reactions. Zeng *et al.* found that the γ_{eff} was 6x10^{-4} for ozonolysis of polydisperse Tri aerosols at 298 K, [32] consistent with the values at 293 K reported

here. [29] This is roughly an order of magnitude higher than the traditional uptake coefficient of O_3 on Tri measured by Wells,[37] and the discrepancy between these values is evidence that radical secondary chemistry is involved in the underlying mechanism.

The trends in γ_{eff} vs. temperature and X_{Tri}, shown in Figure 3.4, exhibit interesting behavior: for pure Tri aerosol (dark blue points, Figure 3.4), γ_{eff} increases monotonically by roughly a factor of 2 as temperature decreases from 293 to 263 K. As discussed in the previous section, the experiment then shows a marked drop from 263 to 253 K not predicted by simulations, attributed to changes in particle phase. As the initial HDA concentration is increased in Figure 3.4 (X_{Tri}=0.8, light blue points; and X_{Tri}=0.3, light orange points), γ_{eff} decreases. At 293 K, the uptake falls to $5x10^{-4}$ and $2x10^{-4}$ for aerosols with X_{Tri}=0.8 and 0.3, respectively, consistent with previous measurements of these kinetics *via* APCI-MS.[29] The trend with X_{Tri} generally holds as temperature decreases, however the slope of γ_{eff} with temperature is less steep at high HDA concentrations. The trend for X_{Tri}=0.8 (X_{HDA}=0.2) looks nearly identical to that for pure Tri aerosol, with γ_{eff} nearly doubling from 293 to 263 K, followed by a drop at 253 K, attributed to the onset of particle freezing. Finally, when HDA is 70% of the initial aerosol composition (X_{Tri}=0.3), values of γ_{eff} plateau at $3x10^{-4}$ at 273 K, exhibiting no sharp decrease at the lowest temperature.

3.3.B. HDA Decay Kinetics

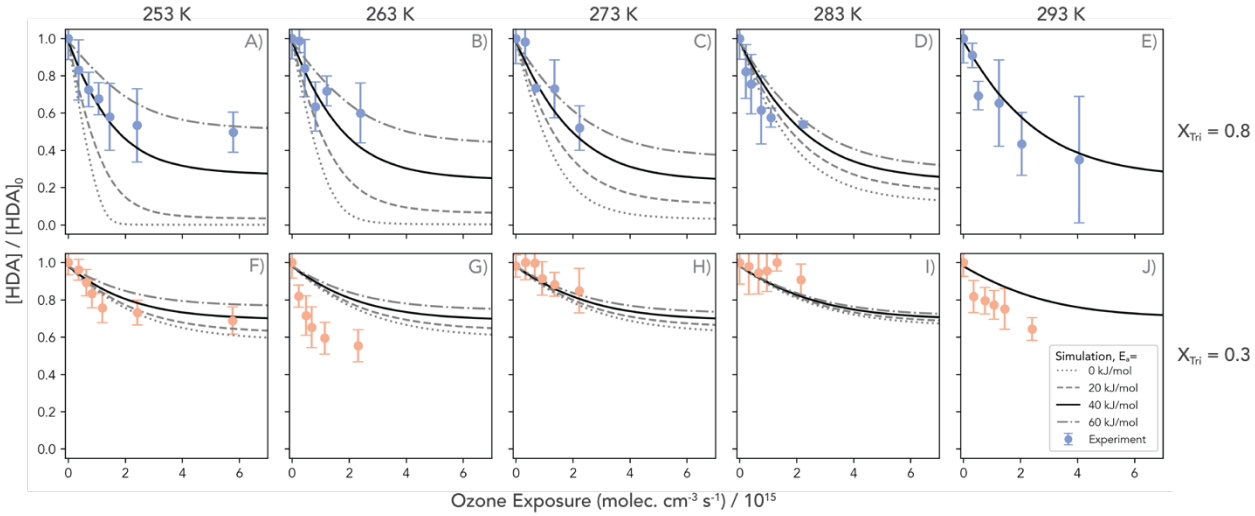

Figure 3.5. HDA decay kinetics from the *m/z* = 256 peak (points) normalized to the initial signal intensity, with simulation results overlaid (lines). Simulations assume four different temperature dependent descriptions of k_{AAHP} corresponding to activation energies (E_a) of 0, 20, 40, and 60 kJ mol^{-1} (denoted by line style).

The decay kinetics of HDA are monitored *via* the decay in intensity of the molecular ion peak at *m/z* = 256, as shown in Figure 3.5. As described previously, HDA fragment ions are observed at *m/z* = 172 and 144, and exhibit nearly identical kinetics to the molecular ion peak (see Figures S8 and S9, *Supporting Information*). Consistent with previous observations,[29] the fraction of the initial HDA remaining at long ozone exposures reaches a non-zero limiting value that depends on the initial composition of the aerosol: a larger fraction of the HDA is consumed when a smaller amount of HDA is initially present in the particle. The decay of HDA is attributed to the

reaction the carboxylic acid functionality with the sCI, which can also be consumed in competing unimolecular reactions (Fig. 3.1). As such, the decay kinetics of HDA can serve as a probe of the branching ratio between these pathways. Notably, the limiting fraction of HDA remaining does not seem to change dramatically across temperatures, suggesting that the change to the branching ratio over this temperature range may be small.

As discussed in more detail later, the temperature-dependent unimolecular decay reaction rate constants of the sCI produced in this mechanism have been constrained by gas phase measurements and theoretical estimates,[22] leaving the temperature dependence of the bimolecular rate constant, k_{AAHP}, free to be optimized to reproduce the experimental results. This rate constant has been found to have no activation barrier for small sCI reacting with small acids in the gas phase,[28] but previous work indicates that the particle phase reaction proceeds at a rate much slower than the expected liquid phase diffusion limit. Kinetic modeling is used to explore the behavior of this reaction mechanism assuming several different values for the activation energy (E_a) to assess a reasonable range of values for this parameter given the HDA decay kinetics observed in these experiments.

3.3.B.i. Optimization of $k_{AAHP}(T)$

The temperature dependence of k_{AAHP} is described using the Arrhenius equation,

$$k_{AAHP} = A \cdot e^{\frac{-E_a}{RT}} \qquad Eq.(3.2)$$

where A is the pre-factor, with the same units as the rate constant (cm^3 $molec.^{-1}$ s^{-1}), and E_a is the activation energy barrier in kJ mol^{-1}. As seen in Figure 3.5, simulations were carried out assuming four different E_a (0, 20, 40, and 60 kJ mol^{-1}). Pre-factors are calculated for each activation energy by assuming no temperature dependence in the pre-factor and by fixing the rate constant at 293 K to be equal to 2.1×10^{-19} cm^3 $molec.^{-1}$ s^{-1}, which is within one standard deviation of the value from previous measurements ($1.85 \pm 0.27 \times 10^{-19}$ cm^3 $molec^{-1}$ s^{-1}) and in accordance with the optimal value of k_{AAHP} previously used in previous simulations.[29] Values of the pre-factor corresponding to each choice of E_a are reported in Table S2, and plots of the corresponding behavior of k_{AAHP} with temperature for each set of Arrhenius parameters is shown in Figure 3.S10 (*Supporting Information*).

In the top row of Figure 3.5, simulation results for each activation energy are overlaid on the experimental data for the decay of HDA observed during ozonolysis of particles with X_{Tri}=0.8. At 293 K (panel E), all of the simulation lines lie atop one another by construction, but as temperature decreases (moving to the left, toward panel A), the model predictions for the extent of the HDA decay diverge. Smaller activation energies (0, 20 kJ mol^{-1}) lead to more extensive HDA decay, while the largest activation energies (40 and 60 kJ mol^{-1}) result in small to moderate decreases in HDA.

The temperature-dependent trend in the experimental data for X_{Tri}=0.8 is modest, with little change in the extent of HDA decay predicted as temperature decreases, and agreement is good between experiments and simulations with an E_a of at least 40 kJ mol^{-1}. This value aligns with predictions for the minimal change in HDA decay kinetics over this temperature range from the analytical expression for HDA decay kinetics derived in previous work.[29] (Figure 3.S11, *Supporting Information*) The simulation results corresponding to an E_a of 40 kJ mol^{-1} have been bolded in Figure 3.5. For the data where X_{Tri}=0.3, the model and experiments agree sufficiently

between 273 and 293 K, with model predictions for nearly all activation energies lying within the experimental error. Agreement is poorer at lower temperatures, where phase effects due to the higher freezing point of HDA may interfere with reaction at the lowest temperatures, as discussed previously.

3.3.C. Reaction Products

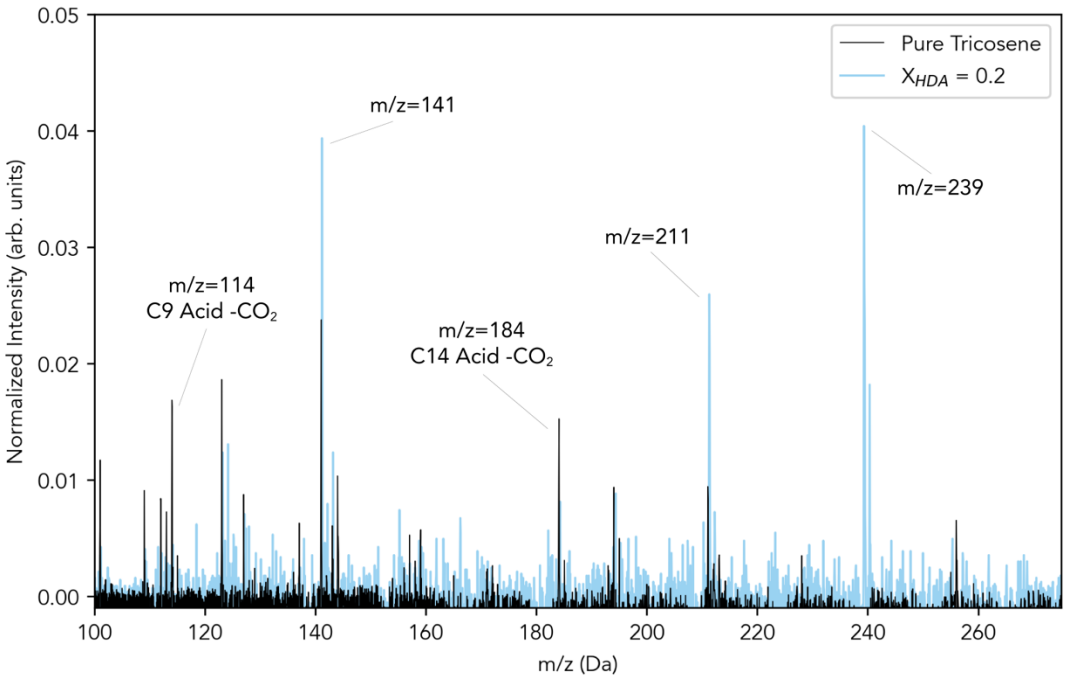

Figure 3.6. Difference Mass spectrum of products from ozonolysis of pure Tri aerosol (black spectrum) and an aerosol mixture with X_{Tri}=0.8, X_{HDA}=0.2 (blue spectrum) at 263 K.

3.3.C.i. Unimolecular sCI Reaction Products

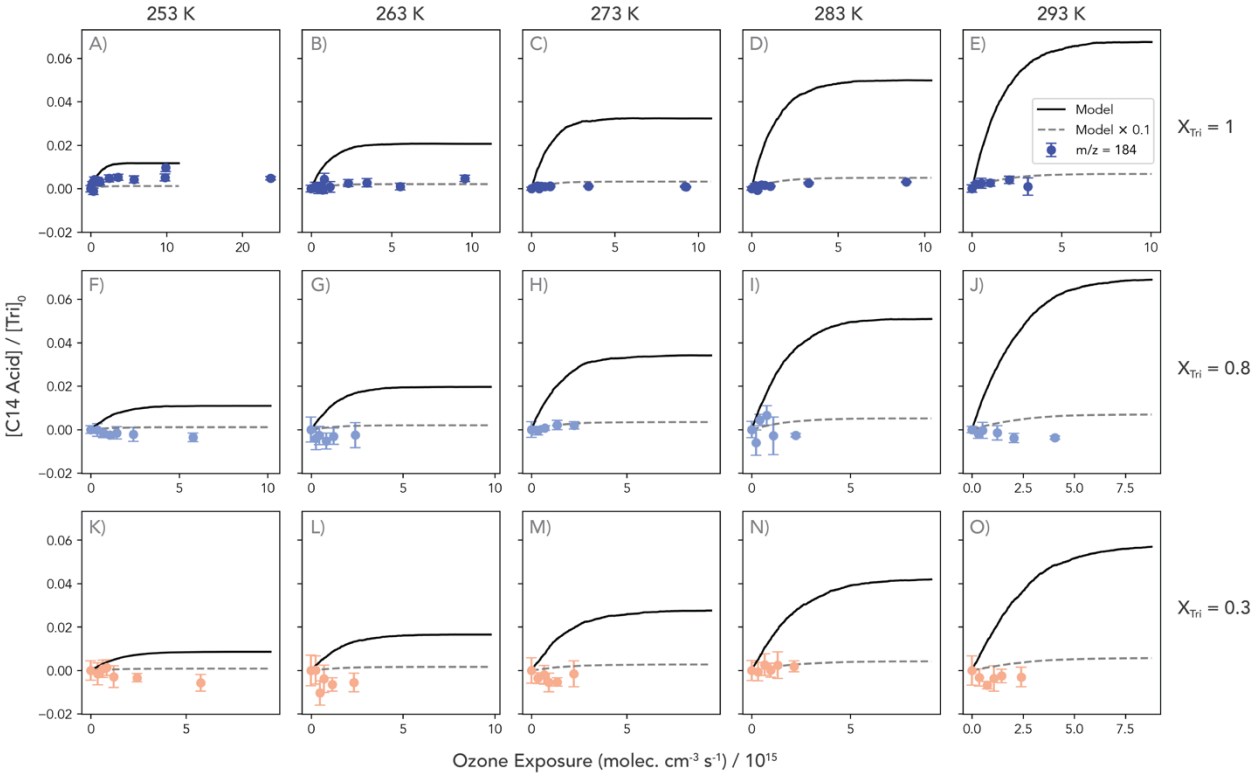

Figure 3.7. Observed kinetics of m/z=184 peak from AMS experiments and C14 acid kinetics from simulations across all conditions represented in this study, normalized to initial Tri signal intensity (experiments, points) or concentration (simulations, lines), respectively. The simulation results scaled down by a factor of 10 have also been overlaid for comparison.

As seen in the difference mass spectrum shown in Figure 3.6, a complex landscape of fragments of reaction products formed from Tri ozonolysis are visible. Two peaks of note are found at *m/z* =114 and 184, which are identified as the decarboxylation (M-CO_2) fragments of the carboxylic acids formed by isomerization of the C9 and C14 sCI (nonanoic acid, MW 158, and tetradecanoic acid, MW 228 — see Figure 3.1A). The growth kinetics of *m/z* = 184 normalized to the initial Tri intensity are displayed in Figure 3.7, showing that these decarboxylation fragments, corresponding to sCI isomerization, only have apparent kinetics in case of pure Tri, where no HDA is present. Corresponding product kinetics and model predictions for *m/z* = 114, corresponding to the decarboxylation fragment of nonanoic acid, are nearly identical and are shown in Figure 3.S5 (*Supporting Information*). For aerosols with X_{Tri}=0.8 or 0.3, these peaks show zero or negative growth relative to the background. Since the small acids assigned to these peaks are formed exclusively by isomerization of the sCI, the lack of growth kinetics for these isomerization products in the presence of HDA suggests that the reaction between sCI and HDA outcompetes this isomerization pathway at all temperatures. Instances of negative kinetics are likely due to fragments produced by ionization of unreacted Tri, which are isobaric with the assigned

decarboxylation fragments, thus decreasing below their background intensities as the reaction proceeds and Tri is consumed.

Simulation Results

The temperature-dependent rate of the sCI isomerization step, k_{iso}, defined in the model is taken from the theoretical structure-activity relationship (SAR) of Vereecken *et al.*,[22] for a primary ethyl sCI in its *anti*-conformer (with the O-O bond facing away from the alkyl chain). The sCI undergoes a 1,3-cyclization reaction to form a dioxirane intermediate, followed by a ring-opening and hydrogen shift to form a carboxylic acid. The rate of this unimolecular process is on the order of 70 s^{-1} at 293 K and decreases by nearly two orders of magnitude as the temperature approaches 253 K, resulting in the trend evident in the simulation results in Figure 3.7: a decrease in the predicted yield of the isomerization product with decreasing temperature. Scaling the simulated predictions down by an order of magnitude allows for reasonable agreement with the experimental data when X_{Tri}=1, but the experimental data does not exhibit the expected trend in product yield with temperature. A combination of factors could contribute to this discrepancy, including a *syn*:*anti* sCI conformer ratio produced by Tri ozonolysis that favors *syn* conformers, in contrast to the 1:1 ratio assumed here for simplicity.[38,39] Additionally, the temperature-dependent trend could be obscured by the scavenging of the isomerization product acids by subsequent reaction with an sCI, as discussed in the following section. However, the disappearance of these isomerization products in the presence of HDA still provides a benchmark for the magnitude of this unimolecular sink for the particle-phase sCI, namely that it is smaller than the sCI + HDA sink under these conditions.

3.3.C.ii. Bimolecular sCI Reaction Products

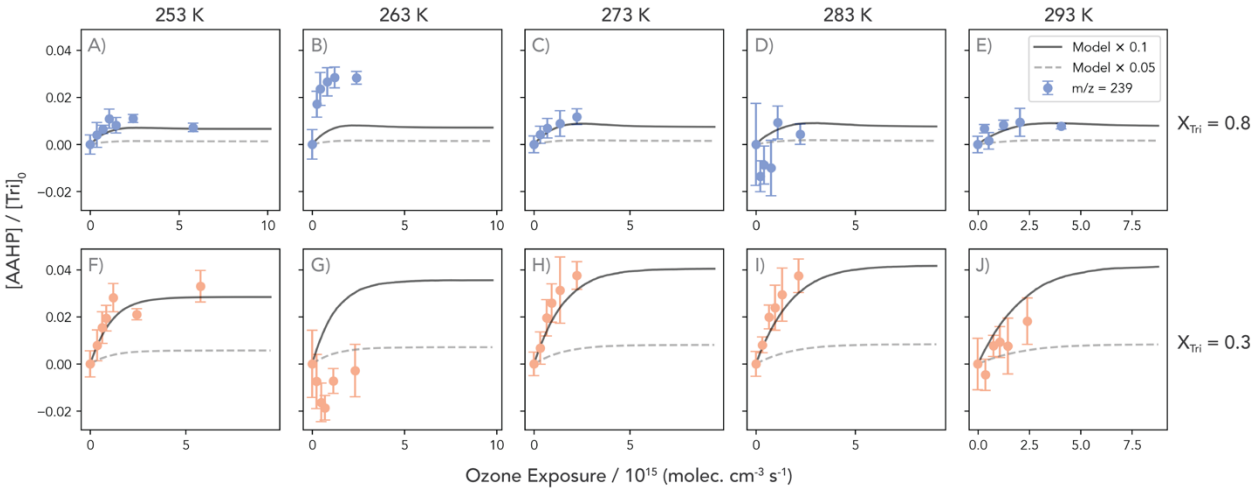

Figure 3.8. Observed kinetics of the *m/z* = 239 peak, identified as the C-O cleavage fragment of the HDA-derived AAHPs (see Scheme 3.S1). Signal intensities are normalized to the initial intensity of the Tri peak (*m/z* = 322) for each experimental condition. The predicted kinetics of the total AAHP production relative to initial Tri concentration ($[Tri]_0$) from the explicit kinetic simulations, scaled down by a factor of 10 and by factor of 20, have been overlaid for comparison.

In the difference spectrum for mixed Tri/HDA aerosols shown in Figure 3.6 (light blue spectrum), the three most prominent peaks are all of odd-integer mass, suggesting fragmentation from a larger molecule: *m/z* = 239 is observed as a product exclusively when HDA is present, and *m/z* = 141 and 211 both appear more abundant in the presence of HDA. A straightforward candidate for the identity of the *m/z* = 239 peak is a fragment of α-acyloxyalkyl hydroperoxide esters (AAHPs) formed from the reaction between either the C_9 or the C_{14} sCI and HDA, resulting in a C_{25} or C_{30} AAHP, respectively (Figure 3.1A).

Assuming these AAHP products are produced *via* the O-H insertion mechanism,[28,40] the C-O bond from the carboxylic acid head group of the HDA will be retained as the ester C-O bond in the AAHP product. Upon photoionization, these HDA-derived AAHPs can undergo fragmentation along the C-O bond of the ester group, yielding an $[HDA\text{-}OH]^+$ fragment at *m/z* = 239, as illustrated in Scheme 3.S1 (*Supporting Information*). Alternately, if photolytic cleavage proceeds along the C-C bond on the opposite side of the carbonyl, the result will be an $[HDA\text{-}HO_2]^+$ fragment at *m/z* = 211. Since both ions involve the HDA moiety, these peaks should probe the kinetics of both HDA-derived AAHPs in aggregate. As such, only the observed kinetics of *m/z* = 239 are shown in Figure 3.8.

By similar analysis, *m/z* = 141 can be assigned to a fragment of the AAHP formed from the reaction of either sCI with nonanoic acid, itself the isomerization product of the C_9 sCI (Figure 3.1A). As for HDA-derived AAHPs, fragmentation of a nonanoic acid-derived AAHP could occur along the ester C-O bond, yielding the observed fragment with *m/z* = 141, or along the alkyl-carbonyl C-C bond, yielding a fragment at *m/z* = 113 (Scheme 3.S2, *Supporting Information*). Although a small peak is observed at *m/z* = 113 in Figure 3.6, its intensity lies too close to the detection limit to be quantified reliably. The kinetics of the *m/z* = 141 peak, along with corresponding predictions of the nonanoic-derived AAHP kinetics, are shown in Figure 3.S7 (*Supporting Information*).

For tetradecanoic acid-derived AAHPs, C-O cleavage yields a fragment with *m/z* = 211, (Scheme 3.S3, *Supporting Information*) isobaric with the C-C cleavage fragment for the HDA-derived AAHPs, explaining why *m/z* = 211 is visible in the pure Tri spectra in Figure 3.6. Therefore, the kinetics of *m/z* = 211 in the presence of HDA, shown in Figure 3.S6 (*Supporting Information*), likely includes contributions from fragments of the tetradecanoic-derived AAHPs. C-C cleavage of the same AAHPs should yield a fragment at *m/z* = 183, where a peak is visible in Figure 3.6 but of too little intensity to be reliably quantified. The relatively low intensities of the C-C cleavage fragments in both Scheme 3.S2 and 3.S3 are consistent with the ester C-O bond in these species likely being more labile to dissociative photoionization.

Simulation Results

The kinetics of *m/z* = 239 in Figure 3.8 largely agree with predictions of the total HDA-derived AAHP kinetics from simulations, which depend on a chosen temperature-dependent description of k_{AAHP}. There is no clear temperature-dependence to the growth kinetics of the AAHP products, which provides further evidence that the branching ratio between unimolecular and bimolecular sCI reactions does not change significantly over this temperature range, as examined in detail in the Discussion.

It should be noted that the peak assignments made here are not definitive, and it is conceivable that some of the peaks in Figure 3.6 could belong to fragments of other reaction products not considered in the mechanism in Figure 3.1A, such as secondary ozonides (SOZs),

which are not observed directly in this study. However, given the symmetric structure of 5-membered SOZ rings, it seems reasonable to expect a nearly even distribution of heavier and lighter fragments from SOZs, which is inconsistent with the observed preference for *m/z* = 141 and 211 fragments over *m/z* = 113 and 183. Nonetheless, sensitivity tests of SOZ formation reactions in the kinetic model have been conducted, and the results are summarized in the *Supporting Information* (Figure 3.S4).

3.4 Discussion

3.4.A. Contributions of Various Reactive Sinks to γ_{eff}

As illustrated in Figure 3.1A, while consumption of Tri is initiated by ozonolysis, Tri can also be consumed by three classes of radical reactions: i) abstraction of a hydrogen atom by an OH radical, ii) OH radical addition to the alkene functionality, and iii) abstraction of a hydrogen atom by an alkoxy (RO) radical. A representation of the individual contributions of all four reactive sinks (ozonolysis and the three radical sinks) to the simulated decay kinetics of Tri, at a fixed ozone exposure of of $1x10^{15}$ molec. cm^{-3} sec^{-1}, are displayed in the bar chart in Figure 3.9. Each bar corresponds to one experimental condition (*i.e.,* T, X_{Tri}) represented in Figure 3.3, with temperature indicated by grouping along the X-axis, and initial X_{Tri} indicated by hatching on the bars. The total height of the bar is proportional to the amount of Tri consumed at the specified ozone exposure, and is proportional to the γ_{eff} predicted by the model. The experimentally-derived γ_{eff} have been overlaid for ease of comparison.

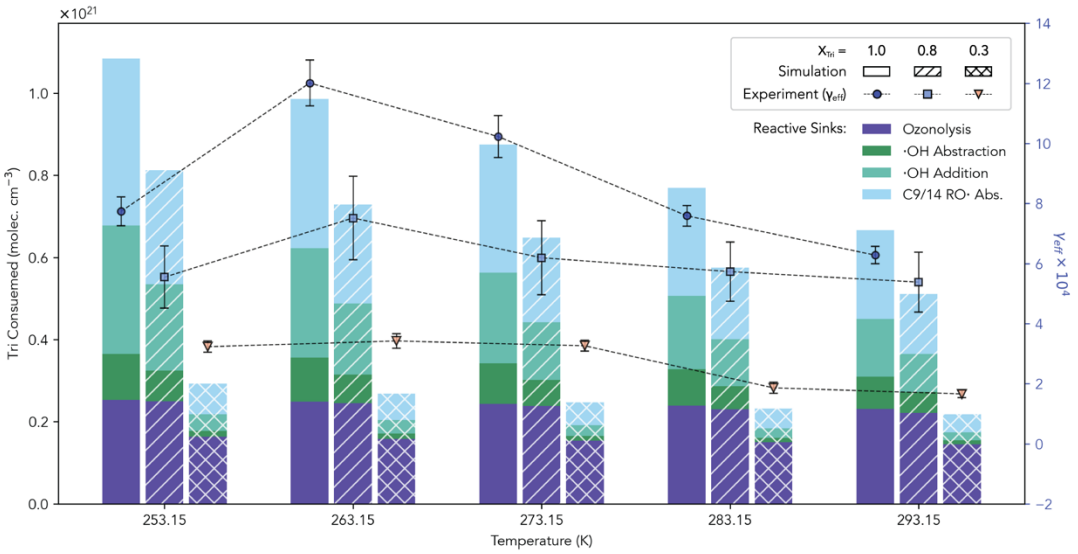

Figure 3.9. Bar chart displaying the breakdown of the contribution of each Tri sink (in ascending order from the bottom of the bar: ozonolysis, OH abstraction, OH addition, and RO radical abstraction) in the model to the overall consumption of Tri at a fixed ozone exposure of $1x10^{15}$ molec. cm^{-3} sec^{-1}. Uptake coefficients from experiments are overlaid (right vertical axis) for comparison.

In the case of pure Tri (unhatched bars), it should be noted that ozonolysis only accounts for approximately a third of the reactivity, with radical reactions accounting for the majority of Tri

consumed across all temperatures. This result is consistent with the single-compartment model published previously by Zeng and Wilson for room-temperature (298 K) ozonolysis of Tri aerosol.[32] As the initial concentration of HDA is increased at each temperature, the contribution of these radical sinks decreases dramatically, while the contribution of the ozonolysis sink changes very little. Since they are the most sensitive to changes in the chemical environment, the contributions of radical reactions to the Tri decay kinetics are key to unraveling the temperature dependent trend in γ_{eff} reported in this work. As shown in Figure 3.1A, all radical species responsible for consuming Tri in the model are generated by the unimolecular decomposition channel of the sCI, which creates both OH and RO radicals. Thus, to investigate how the contributions of radical sinks for Tri change with temperature, we must investigate the temperature-dependent kinetics of the sCI, first in pure Tri aerosols and then in the presence of added HDA.

3.4.B. The sCI Population Enhances the Initiation Rate of Radical Reactions

To begin, we revisit the rate law for the sCI formulated in prior work:[29]

$$\frac{d[\mathrm{sCI}]}{dt} = k_{\mathrm{O3}}[\mathrm{Tri}][\mathrm{O_3}]_b - [\mathrm{sCI}](k_{\mathrm{iso}} + k_{\mathrm{VHP}} + k_{\mathrm{AAHP}}[\mathrm{HDA}]) \qquad Eq.(3.3)$$

By relabeling the production rate of the sCI (the first term of the R.H.S.) as k_1, the sum of all the sink terms as k_2, and setting the initial concentration of Tri to be $[\mathrm{Tri}]_0$, the following solution can be found to Equation 3.3:

$$[sCI](t) = \frac{k_1[Tri]_0}{k_2 - k_1}(e^{-k_1 \cdot t} - e^{-k_2 \cdot t}) \qquad Eq.(3.4)$$

To determine the behavior of this expression with variable temperature, it is instructive to look at representative terms for the rates involved in Equation 3.4. Focusing first on pure Tri aerosols, we assume that [HDA] = 0 and the k_{AAHP} term can thus be neglected. The production rate k_1 is therefore proportional to two terms: the ozonolysis reaction rate, which decreases with decreasing temperature, and the bulk concentration of ozone in the particle (approximated by H_{gb}) which increases with decreasing temperature (Figure 3.1B). The behavior of k_1 is plotted in Figure 3.10A (blue curve, left vertical axis) and shows a slight increase from 293 to 253 K, indicating that the increased solubility of O_3 is dominant over this temperature range. By contrast, k_{VHP}, the unimolecular decay rate of sCI to yield OH and RO radicals, decreases rapidly over the same temperature range (red curve, right vertical axis). With these functional forms for k_1 and k_2, the result of Equation 3.4 are plotted against the model predictions of the total sCI population from kinetic simulations in Figure 3.S12 (Supporting Information).

Since all radical chemistry in the model is initated by unimolecular decay of the sCI, the expected radical contribution to the Tri decay should be proportional to this rate of radical initiation. We may estimate this rate as,

$$k_{VHP}(T) \cdot [sCI]_{tot}(T, X_{Tri}) \qquad Eq.(3.5)$$

where $[sCI]_{tot}$ is the time-integrated total amount of sCI produced during reaction at a given temperature, T, and initial mole fraction of Tri, X_{Tri},

$$[sCI]_{tot} = \int_0^\infty [sCI](t) \cdot dt = \frac{k_1[Tri]_0}{k_2 - k_1}\left(\frac{1}{k_1} - \frac{1}{k_2}\right) \qquad Eq.(3.6)$$

The behavior of Equation 3.6 as a function of temperature is plotted in Figure 3.10B (dashed black curve). Since both k_1 has a negative temperature dependence and k_2 in pure Tri particles has a positive temperature dependence, the total sCI formation rate is predicted to increase dramatically at low temperatures. However, due to the rapid fall-off of $k_{VHP}(T)$ with decreasing temperature, the effective radical initiation rate described in Equation 3.5 has only a modest negative temperature dependence (green curve, Figure 3.10B).

Together, these opposing trends—the increasing sCI concentration and decreasing unimolecular decay rate at low temperatures—explain the trend in radical reactivity in Figure 3.9: although the Tri consumed by ozonolysis remains nearly constant across temperatures, the increased sCI population initiated by ozonolysis drives modest increases in radical chemistry. At low temperatures, these increases contribute significantly to the Tri decay kinetics. This finding highlights the importance of considering secondary reactions when modeling aerosol oxidation at low temperatures. However, it should be noted that this analysis does not include the impact of bimolecular sinks, i.e., the reaction with carboxylic acids, in the sCI sink term k_2. Therefore, fully understanding the temperature dependent behavior of the sCI population requires a treatment of the sCI branching ratio between bimolecular and unimolecular reactions.

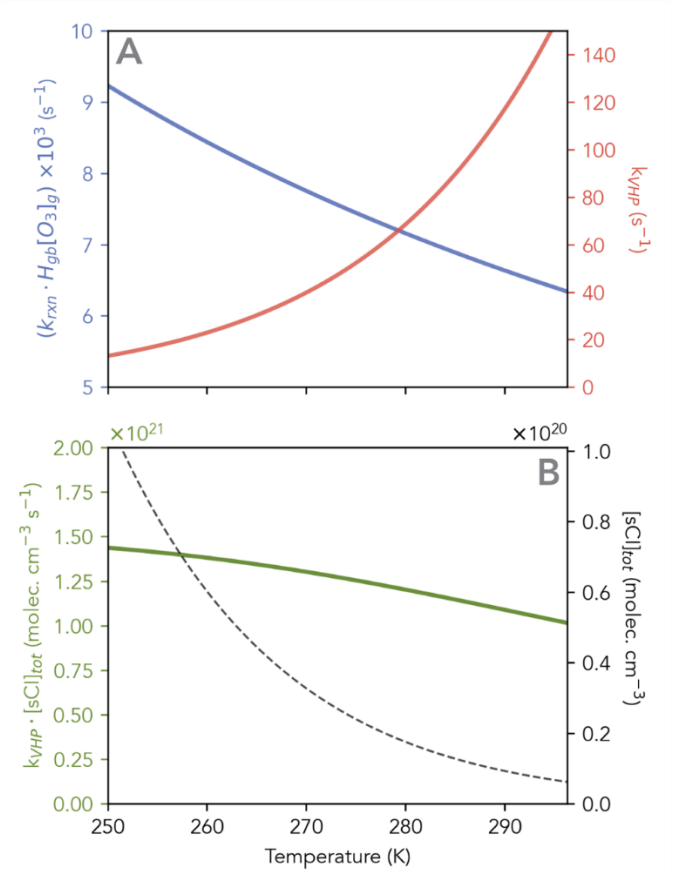

Figure 3.10. Curves illustrating the temperature-dependent behavior of key parameters in this study. A) the pseudo-first order rate of Tri ozonolysis, corresponding to term k_1 in Equation 3.4 (blue curve, lefthand vertical axis) and the sCI unimolecular decomposition rate k_{VHP} (red curve, righthand vertical axis). B) The integrated total concentration of sCI produced during reaction with pure Tri aerosols, according to Equation 3.6 (black dashed curve, righthand vertical axis), and the effective radical initiation reaction rate ($k_{VHP} \cdot [sCI]_{tot}$) during the reaction (green curve, lefthand vertical axis).

3.4.C. The sCI Branching Ratio (k') Balances Unimolecular and Bimolecular Pathways

As seen in Figure 3.9, when the initial HDA concentration in the particles increases, the reactive contributions of radical reactions decrease significantly. As a result, at high initial HDA concentrations, ozonolysis accounts for a much larger fraction of the Tri consumed during the reaction: for simulations with X_{Tri}=0.3 (cross-hatched bars), ozonolysis accounts for roughly two-thirds of the Tri consumption across all temperatures. The decrease in overall Tri consumption with the addition of HDA is therefore primarily due to the loss of radical reaction sinks *via* the reaction between sCI and HDA.

The kinetics of this reaction can be extrapolated from the decay kinetics of the HDA. In previous work at room temperature, the rate of HDA decay was shown to depend on the ratio of rate constants k',[29] defined as

$$k' = \frac{k_{AAHP}}{k_{iso} + k_{VHP}} \qquad Eq.(3.7)$$

Since other bimolecular sinks were neglected, k' also corresponds to the branching ratio between the bimolecular (numerator of Equation 3.7) and unimolecular (denominator) sinks of the particle-phase sCI. Fitting to experimental data in that work yielded a k' of $6.59 \pm 0.95 \times 10^{-22}$ cm^3 molec^{-1} at 293 K, very similar to a value extracted from a modeling study of the ozonolysis of oleic acid particles.[41] Assuming gas-phase literature values for k_{iso} + k_{VHP} at the same temperature, this corresponds to a k_{AAHP} of $1.85 \pm 0.27 \times 10^{-19}$ cm^3 molec^{-1} s^{-1}, which was successfully used to model the reaction kinetics. However, to extend this analysis to temperatures lower than 293 K, temperature-dependent descriptions of the rates in Equation 3.7 must be adopted. Since experimentally-benchmarked theoretical estimates are available for the temperature-dependence of the two unimolecular rates,[22] the description of $k_{AAHP}(T)$ in the particle phase will also determine the temperature dependence of k' for the purposes of this study. Four descriptions of $k_{AAHP}(T)$ are chosen corresponding to the four values of the activation energy (E_a) discussed in the Results and detailed in Table S2 and Figure 3.S10 (Supporting Information).

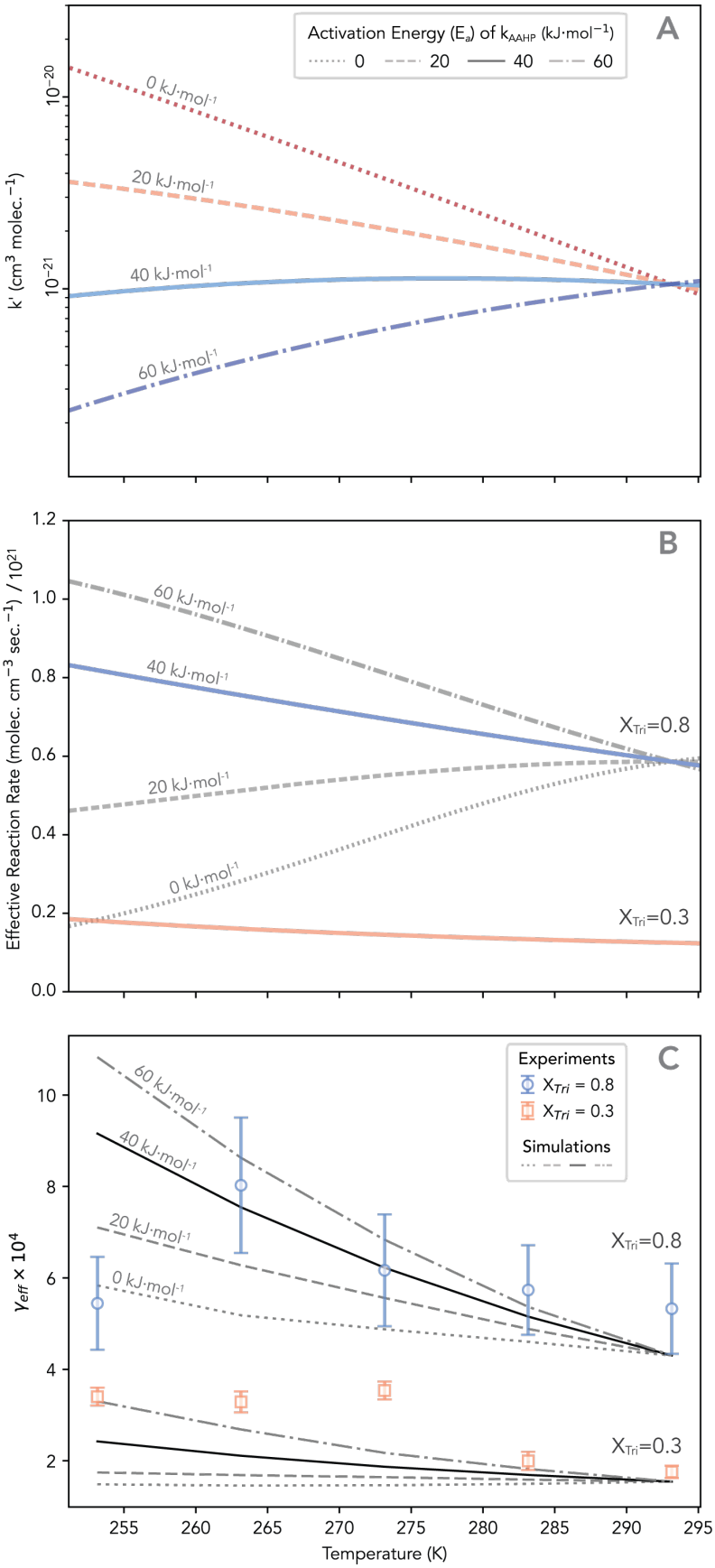

Figure 3.11. The impacts of the temperature-dependent branching ratio k'(T), between unimolecular and bimolecular reactions involving the sCI, on the overall reaction kinetics. Different possible values for the activation energy (E_a) of k_{AAHP}, as outlined in Table S2, are indicated by line style. A) Plot of k' (Equation 3.7) on a logarithmic scale as a function of temperature. B) The effective radical initiation reaction rate ($k_{VHP}\cdot[sCI]_{tot}$) during the reaction, including the effects of the k_{AAHP} sink at various values of E_a. C) Effect of changing the k_{AAHP} activation energy (and therefore k'(T)) on the simulation-predicted Tri uptake (γ_{eff}) when HDA is present, with experimental γ_{eff} overlaid (points).

Figure 3.11A shows the computed k'(T) for each choice of E_a for $k_{AAHP}(T)$, as described in the Results. Note that the values of $k_{AAHP}(T)$, and therefore k'(T), all converge at 293 K by construction in order to agree with room temperature measurements. When E_a=0, k_{AAHP} is constant across all temperatures, while the unimolecular decay rates falls off at low temperatures. This makes the bimolecular channel increasingly favorable at low temperatures, and thus increasing k'. As E_a is increased, the slope of k' with temperature gradually becomes more positive, reaching a nearly flat slope when E_a=40 kJ mol^{-1} (solid line), indicating that the changes in the unimolecular rates and k_{AAHP} under this condition are approximately equal over this temperature range. Thus, an unchanged branching ratio k' with temperature would imply an activation energy of k_{AAHP} on the order of 40 kJ mol^{-1}.

As before for neat Tri aerosols, we may estimate the temperature-dependent population of the sCI produced during the reaction by including the description of $k_{AAHP}(T)$ in the loss term (k_2) in Equation 3.6. The simulation results and predictions for the sCI population (both assuming an E_a of 40 kJ mol^{-1}) when HDA is present in the aerosol are shown in Figure 3.S12 (Panels B and C, Supporting Information). While lower temperatures still lead to enhanced buildup of sCI during the reaction, the presence of HDA reduces the overall sCI population across the modeled temperature range. Computing the effective radical initiation rate for an initial X_{Tri}=0.8 results in the curves plotted in Figure 3.11B, where the relationship between E_a and the slope of the curves is opposite the trend in k'(T): as E_a is increased, the reaction with HDA is diminished at low temperatures, causing the sCI to favor unimolecular reactions. Conversely, a smaller E_a results in a diminishing radical initiation rate with decreasing temperature, as reaction with HDA begins to dominate the unimolecular decay rate. It should also be noted that, as expected, the effect of the sCI + acid reaction scales with the initial HDA concentration in the aerosol, leading to the dramatic decrease in the radical initiation rate when X_{HDA} is increased to 0.7 (X_{Tri}=0.3, solid red line).

Thus, the temperature-dependent branching ratio k'(T), and by extension the activation energy of the primary bimolecular sink, controls a significant portion of the reactivity in mixed Tri/HDA aerosols. This effect is evident in the simulated Tri decay kinetics, as shown in Figure 3.11C. The choice of E_a, and thus the temperature dependence of k'(T), modulates the slope of the uptake coefficient with temperature: smaller values of E_a lead to smaller changes in γ_{eff} with temperature, according to the trend in the radical initiation rate seen in Figure 3.11B. Comparison between the experimental and simulated γ_{eff} additionally provides evidence of an activation barrier to the reaction between sCI and HDA on the order of 40–60 kJ mol^{-1}, in agreement with modeling of the HDA decay kinetics in Figure 3.5. However, it should be noted that simulations with no activation barrier still have a slight negative temperature dependence, due to increases in ozone solubility.

Therefore, consistent with the results presented in Figure 3.9, the net effect of adding HDA to the aerosol mixture is to decrease the effective rate of radical reaction initiation at all temperatures. However, the magnitude of the increase in γ_{eff} requires that the branching ratio k'(T) be sufficiently constant across the temperature range studied here to allow unimolecular reactions to remain competitive. Such a "flat" temperature-dependence of the branching ratio requires a significant activation energy barrier on k_{AAHP} in the particle phase. This result is again in contrast with gas-phase measurements of the sCI + carboxylic acid reaction, which have been shown to be barrierless and enhanced by long-range interactions between the reactants.[27,28,40] In particular, Vereecken notes that reactant orientation is crucial in this reaction, as the insertion reaction mechanism implicated in AAHP formation requires the sCI and the acid functional group

to adopt a co-planar geometry, likely making this reaction subject to substantial steric effects in the particle phase, which could create an activation barrier. Thus, while the presence of particle-phase acids as bimolecular reaction partners does lead to sCI scavenging at low temperatures, relatively high concentrations of acids (*i.e.*, in excess of the alkene) still appear to be required to shut off the effects of sCI-initiated radical chain cycling.

3.5. Conclusion

Together, the experimental data and modeling results presented here highlight how the kinetics of heterogeneous ozonolysis reactions on aerosol particles are strongly determined by the reactivity of particle-phase intermediates, especially unimolecular reactions of the sCI, even at low temperatures. While decreases in temperature lead to decreases in the radical-initiating unimolecular decay rates of sCI, low temperatures also increase the solubility of ozone, leading to increased buildup of reactive intermediate concentrations over the temperature range studied here. Thus, decreases in temperature can have the net effect of enhancing reactivity by indirectly driving increases in secondary chemistry. Additionally, in the presence of a sCI scavenger, such as the saturated acid used here, the activation energy required for the sCI + carboxylic acid reaction in the particle phase leads to decreases in the rate that closely match the decreases in unimolecular rates, maintaining a nearly constant branching ratio between these reactions over the temperature range studied here. This finding would again suggest that, up to a factor of the concentration of scavenger molecules in the particle phase, unimolecular reactions of particle-phase sCI can remain competitive at low temperatures and continue to drive radical chain chemistry.

These results could have implications for other model systems for heterogeneous reactivity, such as oleic acid, where the importance of secondary chemistry to the overall reactivity has been explored.[8,41] In particular, an unchanging temperature-dependent branching ratio between bimolecular and unimolecular reactions could explain why the temperature dependence of the uptake of ozone by supercooled oleic acid aerosols appears to be flat.[7] Due to the high concentration of acid functional groups in oleic acid, bimolecular reactions could modulate both the concentration of particle-phase sCI as well as the radical initiation rate, keeping chain-propagating and chain-terminating reactions in equilibrium before the onset of particle freezing. Future studies could be conducted to explore how well this effect generalizes to similar reaction systems, and to determine the temperature range and conditions over which it is relevant before particle phase effects become dominant.

Finally, avenues for future experimental work include more explicit treatment of particle phase and morphology, both of which affect reactant transport. Experiments with different particle-phase reactants, varied relative humidity, or which include nucleation seeds to induce particle freezing[42] could help to disentangle the effects of particle morphology from the temperature-dependent chemistry explored here. In addition, the role of the surface in facilitating the reaction with respect to changes in temperature and particle composition is a key question, which could be addressed by size-dependent measurements at low temperatures, which report the scaling of the reactivity with particle surface area, or by surface-sensitive spectroscopic techniques, such as X-ray photoelectron spectroscopy, which could report on the evolving composition of the particle surface during reaction.

3.6. Supporting Information

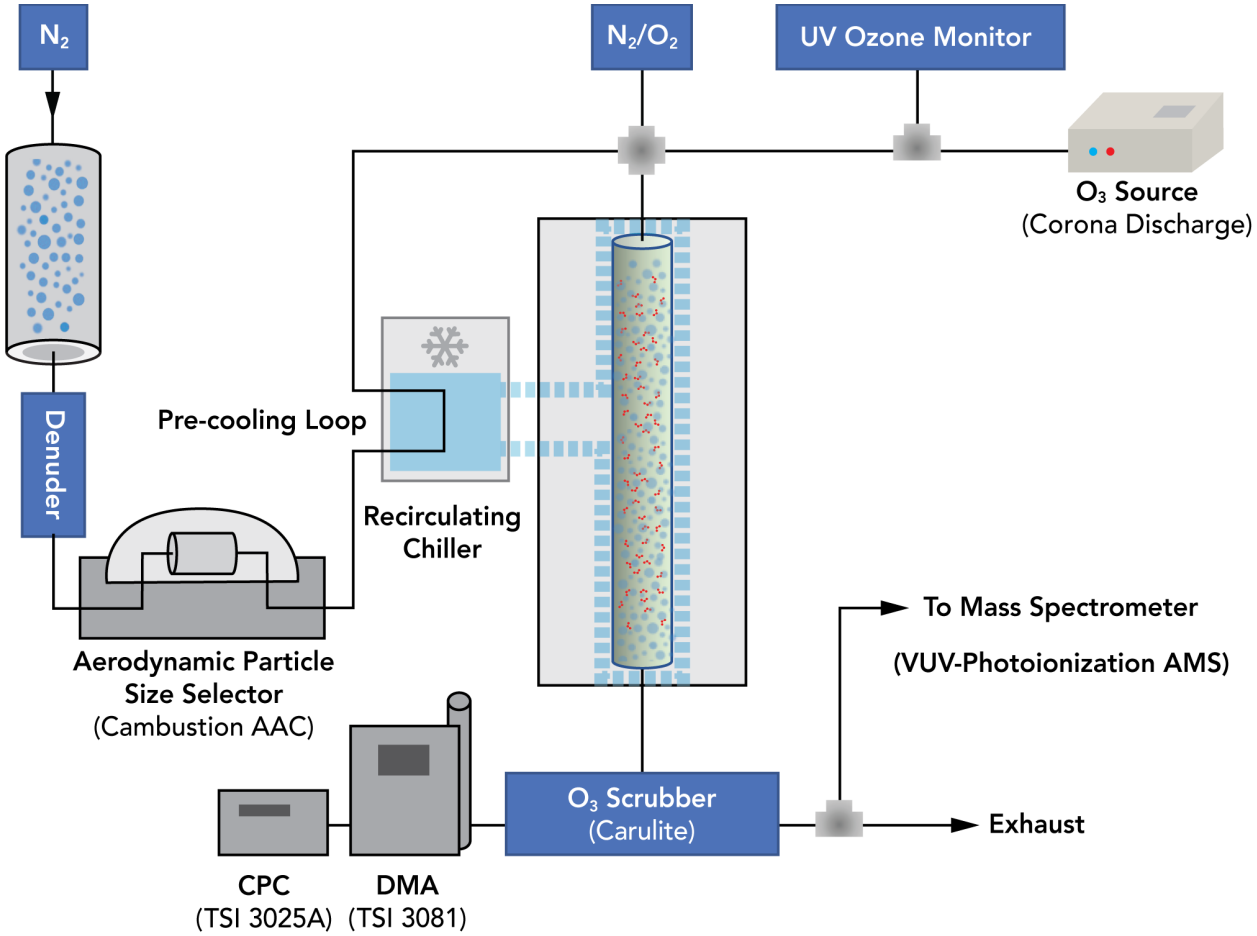

Figure 3.S1. Experimental schematic for temperature-controlled flow tube reactor studies.

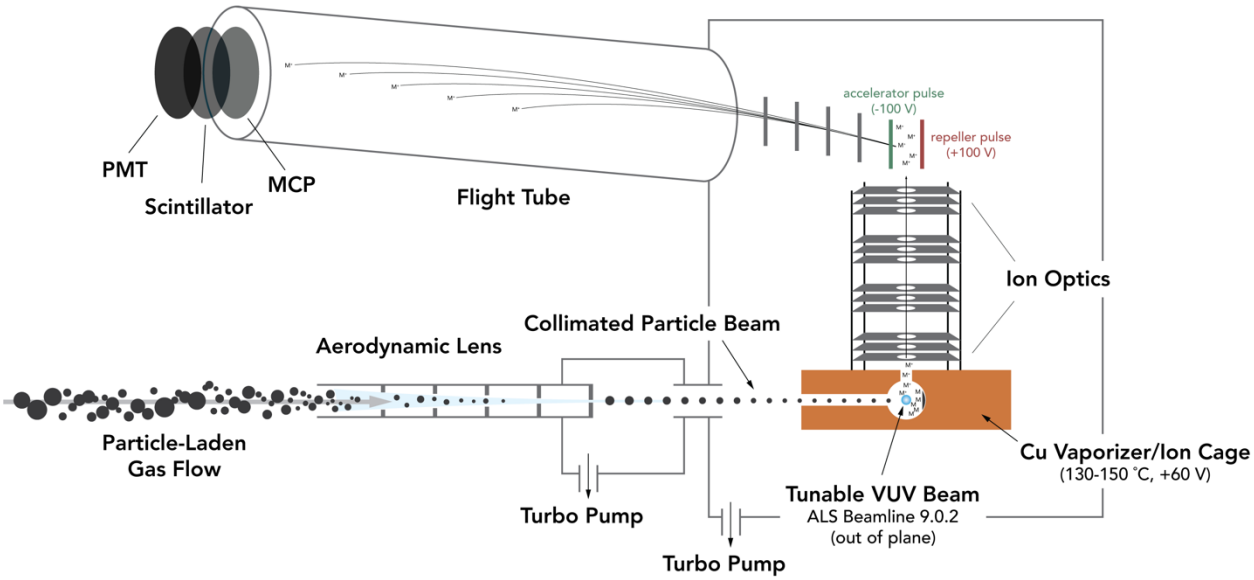

Figure 3.S2. Schematic of the operation of the Vacuum Ultraviolet (VUV) photoionization aerosol mass spectrometer used in this study.

Table 3.S1. Rate constants and associated Arrhenius parameters employed in kinetic modeling studies. ($k = A \cdot T^m e^{\frac{-E_a}{RT}}$, where k is the reaction rate constant, A is the prefactor, m is the temperature exponent, and E_a is the activation energy) Unimolecular reactions (*U*) carry units of s^{-1} for rate constants and pre-factors; bimolecular reactions (*B*) carry units of cm^3 $molec.^{-1}$ s^{-1}.

Label	Reaction	k(293 K)	A	m	E_a (kJ/mol)	Units	Reference
k_{ads}	O_3 (g) -> O_3 (ads)	225	13.1	0.5	0	*U*	Calculated (see below)
k_{des}	O_3 (ads) -> O_3 (g)	$1.35x10^{10}$	$7.91x10^{8}$	0.5	0	*U*	“”
k_{sol}	O_3 (ads) -> O_3 (bulk)	$7.16x10^{9}$	$4.18x10^{8}$	0.5	0	*U*	“”
k_{desol}	O_3 (bulk) -> O_3 (ads)	$1.73x10^{-12}$	$8.27x10^{-10}$	0.5	10.73878	*B*	This Work
k_{rxn}	O_3 (ads) + Tri -> CI + C=O	$1.88x10^{-16}$	$2.5x10^{-15}$		8.0	*B*	Calculated (see below)
k_{VHP}	CI -> RO· + ·OH	205	$2.41x10^{-62}$	24.3	61.35	*U*	Vereecken[22]
k_{iso}	CI -> RCOOH	74	$5.63x10^{9}$	1.2	-21.375	*U*	Vereecken[22]
k_{AAHP}	CI + HDA -> AAHP	$2.1x10^{-19}$	$2.82x10^{-12}$		40 (base model)	*B*	This work, Reynolds (2023)[29]
k_{SOZ}	CI + RC=O -> SOZ					*B*	*(Sensitivity Test Only)*
	·OH + Tri -> Tri-R· + H_2O (1˚ abstraction)		$2.68x10^{-17}$	2	2.52	*B*	Atkinson[43]
	·OH + Tri -> Tri-R· + H_2O (2˚ abstraction)		$1.64x10^{-16}$	2	-1.94	*B*	“”
	Tri-R· + O_2 -> Tri-ROO·	10^{6}				*U*	Zeng[32]
	2 Tri-ROO· -> 2 RC=O + ROH		$3.32x10^{-14}$		8.4	*B*	Denisov[44]
	RO· + RH -> R· + ROH		$1.66x10^{-11}$		22.4	*B*	“”
	·OH + Tri -> Tri-OH· (addition)		$1.10x10^{-11}$		-4.05	*B*	Peeters[45]

Label	Reaction	k(293 K)	A	m	E_a (kJ/mol)	Units	Reference
	Tri-OH· + O_2 -> β-ROO·	10^6				*U*	Zeng[32]
	2 β-ROO· -> 2 RC=O + ROH		3.32×10^{-14}		8.4	*B*	Denisov[44]
$k_{\beta RO2}$	β-ROO· -> CI + ROH	120				*U*	Zeng[32]
	HDA + ·OH (1˚ abstraction)		2.68×10^{-17}	2	2.52	*B*	Atkinson[43]
	HDA + ·OH (2˚ abstraction)		1.04×10^{-16}	2	-1.94	*B*	“”
	HDA + ·OH (3˚ abstraction)		1.89×10^{-18}	2	-5.91	*B*	“”
$k_{diff,C=O}$	C9_aldehyde (bulk) => C9_aldehyde_des	10^4				*U*	Calculated
k_{evap}	C9_aldehyde_des => C9_aldehyde (g)		3.5×10^{16}	-0.5	55.33	*U*	Calculated

(Table 3.S1, continued from previous page)

Discussion of Kinetic Parameters

Primary Ozonolysis Rate Constant: $k_{rxn}(T)$

For an estimate of the rate at 293 K in the dilute solution limit, we consulted Sazhina et al.,[46] which reported a range of ozonolysis rate constants for long-chain carboxylic acids at 293 K in CCl_4 between 1–2.5x10^{-16} cm^3 $molec.^{-1}$ sec^{-1}. The activation barrier to the primary ozonolysis rate was benchmarked to gas-phase data.[47] For various symmetrical internal alkenes (C_2-C_{10}), the reported activation energies ranged from 8–21 kJ/mole.[47] A value of 8 kJ/mol was chosen for the activation energy of the ozonolysis reaction, and the pre-factor back-calculated from the solution-phase rate at 293 K. While the overall kinetics of ozonolysis predicted by the model are moderately sensitive to the absolute ozonolysis rate constant used in the model, the observed trend in experimental uptake cannot be reproduced by merely decreasing the activation energy of the ozonolysis rate or the absolute magnitude of the pre-factor.

Ozone Equilibrium Partitioning Parameters: $H_{gs}(T)$, $H_{gb}(T)$, and ΔG_{sol}

The transport of ozone from the gas phase into the particle phase is modeled as a coupled-equilibrium process, following the framework developed by Willis and Wilson.[9] The equilibrium ozone concentration in the bulk of the aerosol particle is determined by the (dimensionless) gas-bulk Henry's law constant of O_3 in Tri, expressed as

$$H_{cc}^{gb} = e^{\frac{-\Delta G_{sol}}{RT}} \qquad Eq.(3.S1)$$

where ΔG_{sol} is the solvation free energy of ozone in the organic phase. Since O_3 is reactive with Tri, the solubility of O_3 in organic solvents as reported by Panich and Ershov[20] is used to determine a reasonable value of ΔG_{sol}. The room temperature (293 K) Henry's law constant for O_3 was benchmarked to a reasonable range found in literature for organic solvents, which suggested an H_{cc}^{gb} below 3, corresponding to a ΔG_{sol} of -2.7 kJ mol^{-1} or greater.

For the partitioning between the gas and the interface, we turn to Molecular Dynamics simulations to inform our understanding. Von Domaros et al.[48] predict that for the solvation of O_3 into squalene, a branched, unsaturated lipid-like molecule, there is no surface or near-surface minima for O_3 in the potential of mean force (PMF) plot, unlike the functional form of the PMF observed for O_3 in water.[49] Instead, the PMF appears to decrease monotonically until it reaches the favorable environment of the bulk condensed phase. Given that no enhancement in the concentration of surface-adsorbed ozone is favored over the gas phase concentration, the equilibrium constant H_{cc}^{gs} is fixed to be unity.

Accurately describing the solvation entropy change, and therefore the slope of the solvation free energy change across the temperature range measured here is essential for capturing the expected increase in ozone solubility with temperature. Following the method for calculating solvation entropy changes outlined by Garza,[50] we determined a reasonable estimate for the solvation entropy change between -40 and -60 J mol^{-1} K^{-1}. The primary contribution this entropy loss upon solvation in Garza's model is the decrease in rotational degrees of freedom, which occurs due to the solvated ozone molecule residing in the constricted space of solvation cavities determined by the free volume available within the solvent. The value of ΔG_{sol} at 263 K adopted in the model was found by adjusting the value until agreement was achieved with experimental results, yielding a free energy of -3.598 kJ mol^{-1}. By back calculating the slope given the value of -2.47 kJ mol^{-1} for ΔG_{sol} at 293 K, an empirical value for ΔH_{sol} of -10.739 kJ mol-1 and a ΔS_{sol} of

-28.206 J mol^{-1} K^{-1}. For comparison, the ΔH_{sol} reported for O_3 in CCl_4 by Panich and Ershov is -11 kJ mol^{-1}, and the predicted ΔG_{sol} for O_3 in squalene predicted from MD is roughly -10.5 kJ mol^{-1} (-2.5 kcal mol^{-1}),[48] which yields a ΔH_{sol} of roughly -18.9 kJ mol^{-1}, if the empirically-derived value of ΔS_{sol} above is used at 298 K. In summary, the chosen parameters for solubility lie in a range of reasonable values outlined by experiment and theory.

Adsorption, Desorption, and Solvation Rates

The rate of adsorption is given by,

$$k_{ads} = \frac{\sigma A_{surf} \bar{c}}{4} [O_3]_g \qquad Eq.(3.S2)$$

where σ is the sticking coefficient, A_{surf} is the surface area of the simulation, and

$$\bar{c} = \sqrt{\frac{8RT}{\pi M_{O_3}}} \qquad Eq.(3.S3)$$

is the mean speed of an impinging ozone molecule on the particle surface at temperature T. An ozone concentration of 1 ppm (or 2.5x10^{13} molec. cm^{-3}) was assumed for these simulations. Sensitivity tests were conducted on the sticking coefficient and no difference in the kinetics were observed for $\sigma > 0.1$, so a value of 0.1 was used for the sake of computational efficiency. Since

$$H_{gs} = \frac{k_{ads}}{k_{des}} = 1 \qquad Eq.(3.S4)$$

we set k_{des} to be equal to $k_{ads}[Site]$, where [Site] is the concentration of adsorption sites on the surface, which is implicitly included in the rate in Kinetiscope simulations. In practice in simulations this site concentration is set equal to $[Tri]_0$, and is never significantly depleted during the course of the reaction.

The solvation rate is linked to the desorption rate *via* the mass accommodation coefficient:

$$\alpha = \frac{k_{sol}}{k_{sol} + k_{des}} \qquad Eq.(3.S5)$$

$$k_{sol} = \left(\frac{\alpha}{1-\alpha}\right) k_{des} \qquad Eq.(3.S6)$$

where $\alpha = 0.346$ from MD simulations of O_3 on Squalene.[48] Finally, the solvation and desolvation rate are coupled by

$$H_{sb} = \frac{H_{gb}}{H_{gs}} = H_{gb} = \frac{k_{solv}}{k_{desolv}} \qquad Eq.(3.S7)$$

where H_{sb} is the surface-bulk partitioning coefficient of O_3, and remembering that $H_{gs} = 1$ as discussed above. Thus, for the desolvation rate coefficient, we have

$$k_{desolv} = \left(\frac{\alpha}{1-\alpha}\right)\frac{k_{des}}{H_{gb}[Site]} \qquad Eq.(3.8)$$

where we have divided by a factor of the site concentration to account for the adsorption site description in Kinetiscope, as was done for the desorption rate.

Diffusion of O_3

In the simulation framework assumed here, the diffusion rate of O_3 between the particle surface and bulk compartments is assumed to be constant with respect to temperature and proportional to the viscosity of the organic matrix. The viscosity (η) of Tri has been measured to be 15 mPa·s.[51] Assuming a collisional radius (R_{coll}) for Tri of 2 Å, an approximate self-diffusion coefficient may be calculated using the Stokes-Einstein Relation,

$$D_{org} = \frac{k_B T}{6\pi\eta R_{coll}} \qquad Eq.(3.S9)$$

which yields a value of approximately $2.99\text{x}10^{-7}$ cm^2 s^{-1}. Following a common assumption in the oleic acid literature, we estimated the diffusion coefficient of ozone in the organic, D_{O_3}, as one order of magnitude faster than the self-diffusion coefficient of the organic.[52,53]

The choice of diffusion coefficient for reactive species in the particle should thus be proportional to the temperature-dependent phase and viscosity behavior of the particle matrix, which is additionally expected to evolve with reaction. As a result, any description of diffusion that does not account for changes with reactivity is certainly an oversimplification of the true temperature-dependent behavior of the diffusion coefficient of the reactants displayed. This assumption should especially break down in the case of a particle phase transition, as has been postulated for the lowest-temperature kinetic data in this study (see Results). However, following a similar approach, Li and Knopf[54] estimated the self-diffusion coefficient of OH radicals in saturated alkane aerosol particles across the broad temperature range measured in their experiments (213-293 K) in a similar manner by estimating the viscosity of squalane from a Volgel-Fulcher-Tamman equation fit, and the diffusion coefficient of OH radicals from a fractional Stokes-Einstein relationship. This approach allowed for excellent agreement between model and experiment, albeit with several adjustable parameters, and suggested that the temperature dependence of the diffusion coefficient over the range investigated in this study (253–293 K) was less than an order of magnitude.

Thus, to assess the importance of the parameter choice of D_{O_3} on the model, a sensitivity test of this parameter was conducted for room temperature simulations by scaling D_{O_3} up and down by an order of magnitude (factor of 10). The results are displayed in Figure 3.S3 and show that the choice of D_{O_3} does indeed have a significant impact on the simulated Tri decay kinetics.

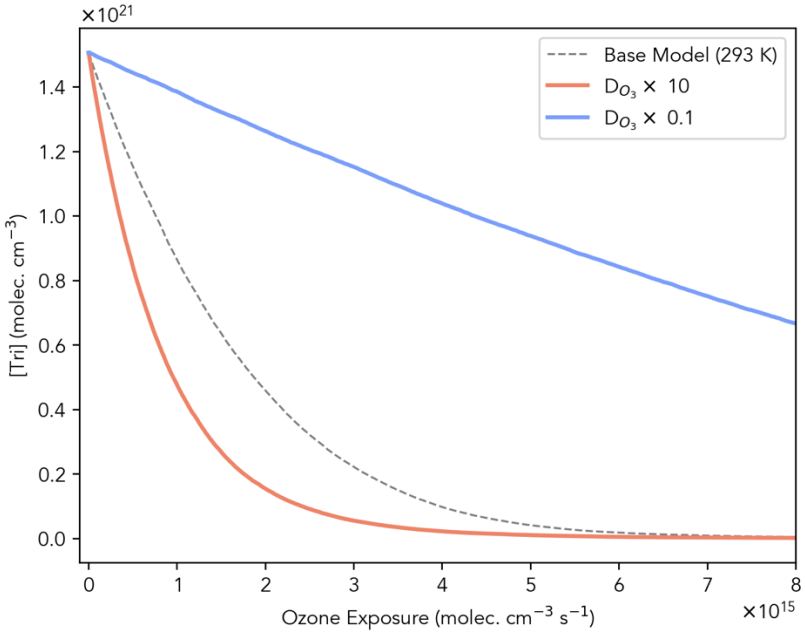

Figure 3.S3. Sensitivity test of the diffusion coefficient of ozone through the particle bulk (D_{O_3}, from the surface to the bulk compartment in the simulated kinetic model) on the predicted Tri decay kinetics in pure Tri aerosol at 293 K. The base model (D_{O_3}=2.92x10^{-6} cm^2 sec.$^{-1}$) is shown in the black dotted line, while the two sensitivity test conditions (D_{O_3} = 2.92x10^{-5} cm^2 sec.$^{-1}$, red curve below the dotted line, and D_{O_3} = 2.92x10^{-7} cm^2 sec.$^{-1}$, blue curve above the dotted line) are displayed as solid lines.

Evaporation of Volatile Carbonyl Species

Following the approach used in previous studies,[13] temperature-dependent evaporation rate constants are derived from the Hertz-Knudsen equation:

$$k_{evap} = \sqrt{\frac{N_A}{2\,\pi M k_B T}}\left(\frac{A_{sim}}{V_{sim}}\right)\frac{p_{sat}(T)}{[Org]_0} \qquad Eq.(3.S10)$$

where N_A is Avogadro's number, M is the molar mass of the evaporating compound in g mol^{-1}, A_{sim} / V_{sim} is the surface to volume ratio of the compartment from which the molecule is evaporating (in this case, a 1 nm^3 surface compartment, so A_{sim}/V_{sim} = 10^{-9} m^{-1}), $[Org]_0$ is the number density of the total organic material in the surface compartment (as an approximation to the Hertz-Knudsen equation, which is derived for evaporation of pure components), and $p_{sat}(T)$ is the temperature-dependent saturation vapor pressure of the compound of interest, which may be fit from literature data for the species of interest assuming ideality using a form of the Clausius-Clapeyron equation:

$$\frac{p_{sat}(T)}{p_{sat}(T_{ref})} = p_{sat}(T_{ref}) \cdot e^{\frac{-\Delta H_{vap}}{RT}} \qquad Eq.(3.S11)$$

Values of ΔH_{vap} for nonanal and tetradecanal were taken from the measurements of Verevkin et al.,[55] and the corresponding Arrhenius parameters for k_{evap} calculated for nonanal are listed in Table S1.

Before evaporation, an evaporating molecule is required to traverse to the surface compartment and encounter a surface desorption site (des_site in the Kinetiscope model), from which it can then evaporate with the rate k_{evap} described above. We assume that this process is diffusion-controlled, with the diffusion coefficient being the same as that of self-diffusion in the organic. As such, the characteristic rate for a nonanal molecule to traverse the bulk and surface compartments (of dimension R/3 = 61.7 nm) should be on the order of

$$k_{diff,C=O} \approx \frac{D_{org}}{\left(\frac{R}{3}\right)^2} = \frac{2.92 \cdot 10^7 \frac{nm^2}{sec}}{(61.7\ nm)^2} \approx 7.67 \cdot 10^3\ sec.^{-1} \qquad \text{Eq. (3.S12)}$$

Thus, a rate of 10^4 sec.$^{-1}$ was used in simulations for an evaporating molecule finding a desorption site.

Given that there are a limited number of desorption sites, any molecule with significantly slow evaporation kinetics will deplete the number of available sites and inhibit other species from evaporating. This is a known issue with this evaporation description, which is currently under development in extending the usability of this model framework. The evaporation kinetics for tetradecanal, nonanoic acid, and tetradecanoic acid all exhibited this unphysical behavior, and thus the evaporation of these species was not explicitly treated in the model. The evaporation of the multi-carbonyl C_9 products derived from ozonolysis of TriO, $TriO_2$, $TriO_3$, and higher-order oxidized species produced by peroxy radical chemistry were treated with the same evaporation kinetics as nonanal. The kinetic model predicts, in agreement with equilibrium partitioning calculations,[56] that nonanal will entirely evaporate out of the particles over the reaction timescale considered here.

Secondary Ozonide (SOZ) Formation Rate

Although direct evidence of secondary ozonide (SOZ) formation, primarily from the recombination of sCI with carbonyl products from ozonolysis, was not observed in these experiments, some aldehydes and other carbonyl reaction products are expected to be in the particle phase to react with the sCI. Although gas-phase temperature dependencies of the CI + carbonyl rate constant have been measured via "direct production" experiments, and found to have a slight negative temperature dependence,[57,58] it is unclear whether these kinetic parameters would translate from the small, gas phase molecules to the longer-chain particle phase aldehydes and sCI considered here. Therefore, a sensitivity test was conducted assuming rate constants optimized previously in modeling studies of squalene nanoparticle ozonolysis, and assuming these coefficients were constant with temperature: a rate constant of 1.3×10^{-18} molec. cm^{-3} sec.$^{-1}$ for "in-cage" recombination (the reaction partners result from decomposition of the same primary ozonide and thus presumably do not need to leave their solvent "cage" to have a reactive encounter, *viz*. nonanal + C14 sCI and tetradecanal + C9 sCI) and a slightly slower rate constant of 6.7×10^{-19} molec. cm^{-3} sec.$^{-1}$ for "out-of-cage" recombination (*viz*. tetradecanal + C14 sCI and nonanal + C9 sCI). The results on the γ_{eff} predicted by the kinetic model are shown in panel A of Figure 3.S3. In comparison to the base simulations without SOZ formation reactions, the γ_{eff} are much smaller

when SOZ reactions are included, and the negative slope of the kinetics with temperature is less steep, presumably due to the extra sink for the sCI reducing the amount of radical chemistry initiated by decomposition.

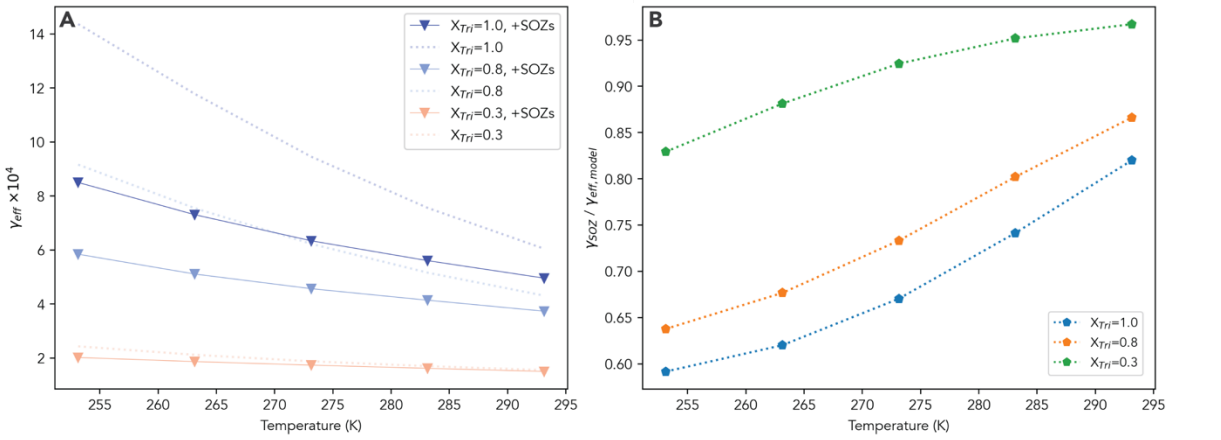

Figure 3.S4. Simulation results of sensitivity tests of the SOZ forming (sCI + aldehyde) reaction on the kinetics predicted by the model. A) Uptake coefficients predicted when the SOZ reaction pathway is included (solid lines/triangles), with uptake coefficients predicted by the base model (dotted lines) displayed for comparison. B) The ratio of uptake coefficients predicted with the SOZ formation step to base-model uptake coefficients as a function of temperature.

However, as seen in Figure 3.S4.B, the effect of greater partitioning of nonanal into the particle at lower temperatures can be seen in the ratio of the γ_{eff} with and without the SOZ formation step included. At low temperatures and low HDA concentrations, where radical chemistry becomes a more significant sink for Tri, the increased abundance of nonanal increases the sCI sink attenuated by increasing the initial HDA concentration, as the sCI sink provided by the sCI + acid reaction is more significant than that provided by the SOZ formation pathway. Thus, the SOZ sink may have a significant effect on this reaction mechanism, and future studies on its temperature-dependent behavior in the particle phase are needed to assess whether its energetics differ from gas-phase measurements.

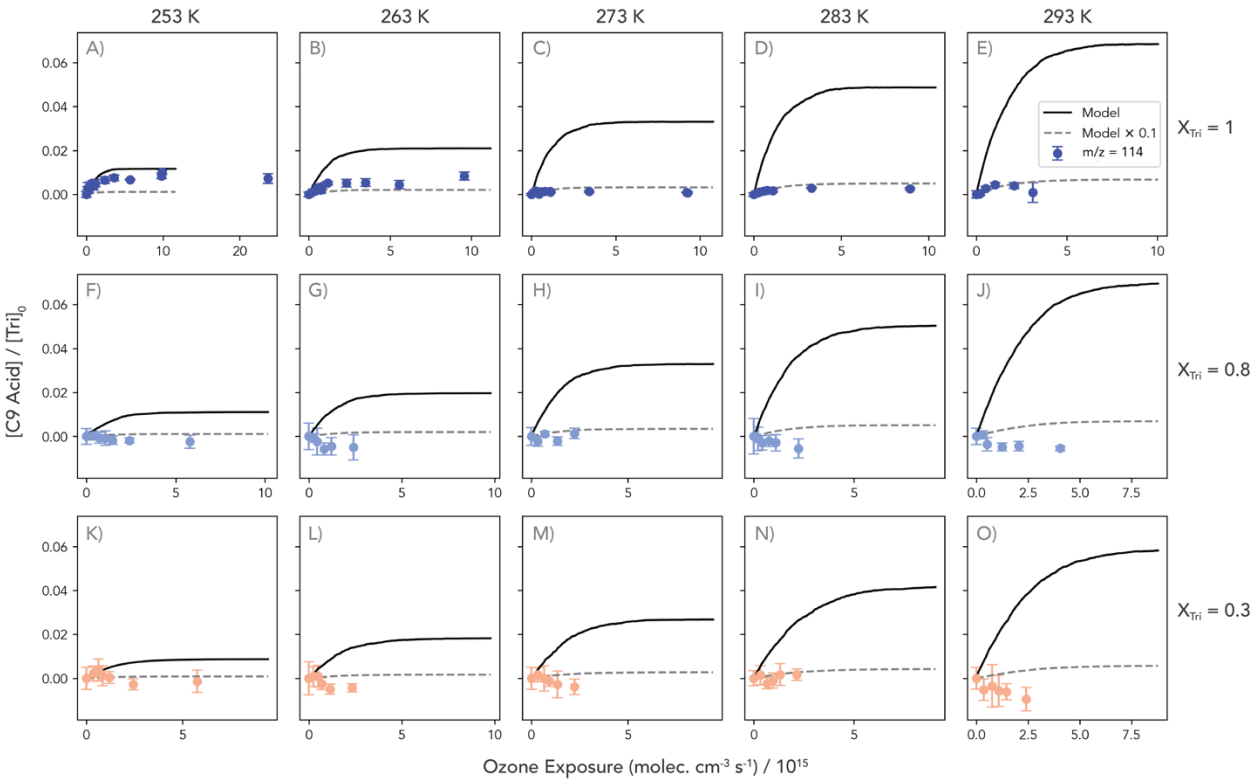

Figure 3.S5. Observed kinetics of the m/z=114 peak, identified as a decarboxylation fragment of the C9 acid formed by isomerization of the sCI.

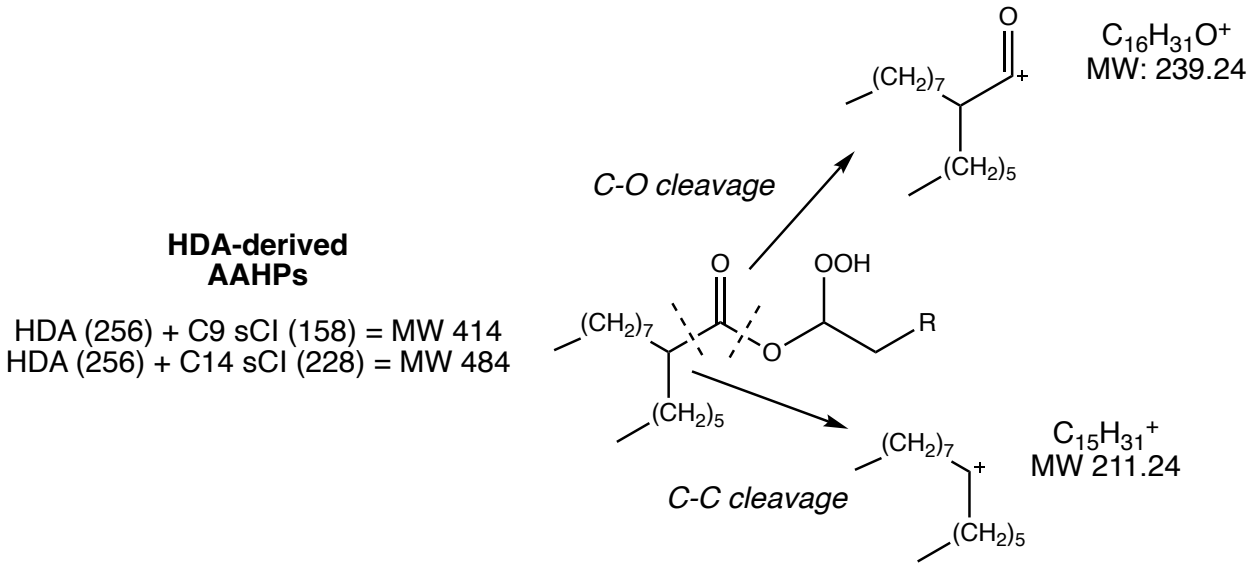

Scheme 3.S1. Proposed fragmentation scheme of an HDA-derived AAHPs into two fragments (m/z = 211 and 239).

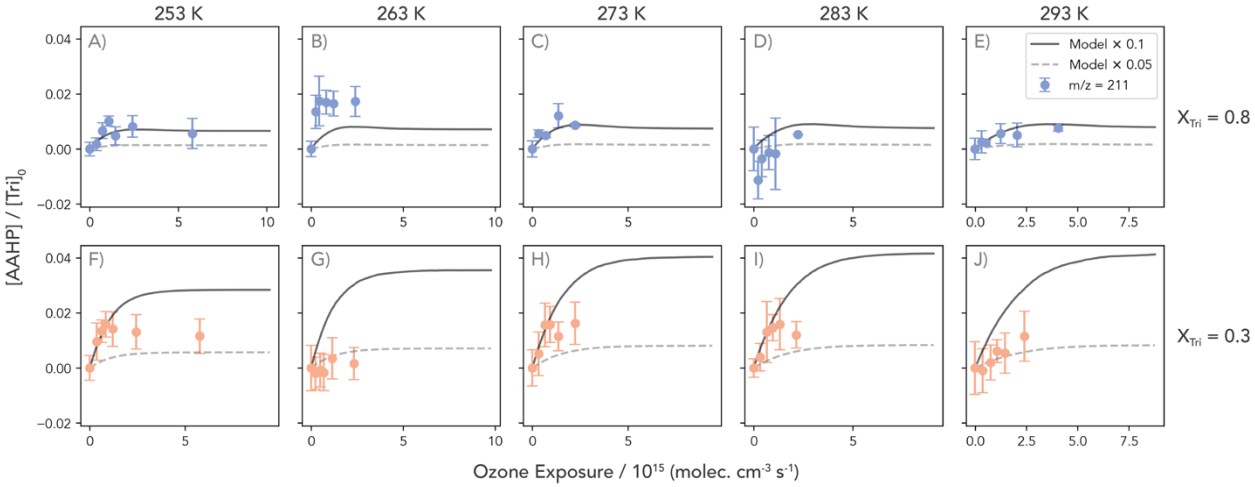

Figure 3.S6. Observed kinetics of the m/z = 211 peak, identified as either the C-C cleavage fragment of the HDA-derived AAHPs (see Scheme S1) or the C-O cleavage fragment of the tetradecanoic acid-derived AAHPs (see Scheme 3.S3). Signal intensities are normalized to the initial intensity of the Tri peak (m/z=322) for each experimental condition. The predicted kinetics of the total AAHP production relative to initial Tri concentration ($[Tri]_0$) from the explicit kinetic simulations, scaled down by a factor of 10 and by factor of 20, have been overlaid for comparison.

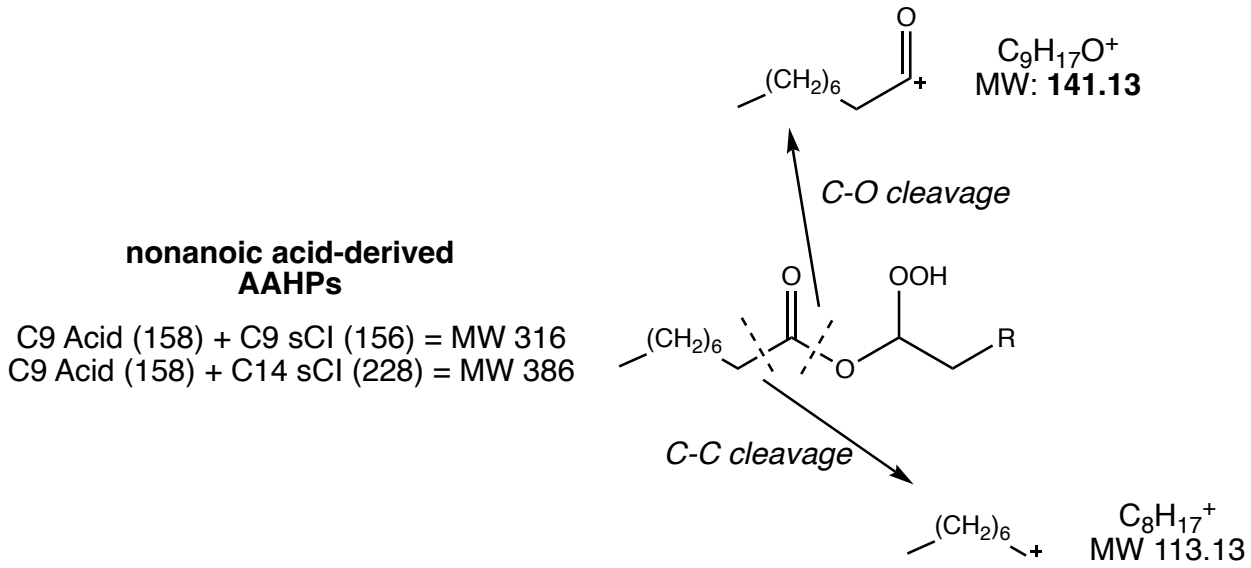

Scheme 3.S2. Proposed fragmentation schemes of AAHPs derived from tetradecanoic acid ($C_{14}H_{28}O_2$, MW 158) reacting with the C9 and C14 sCI.

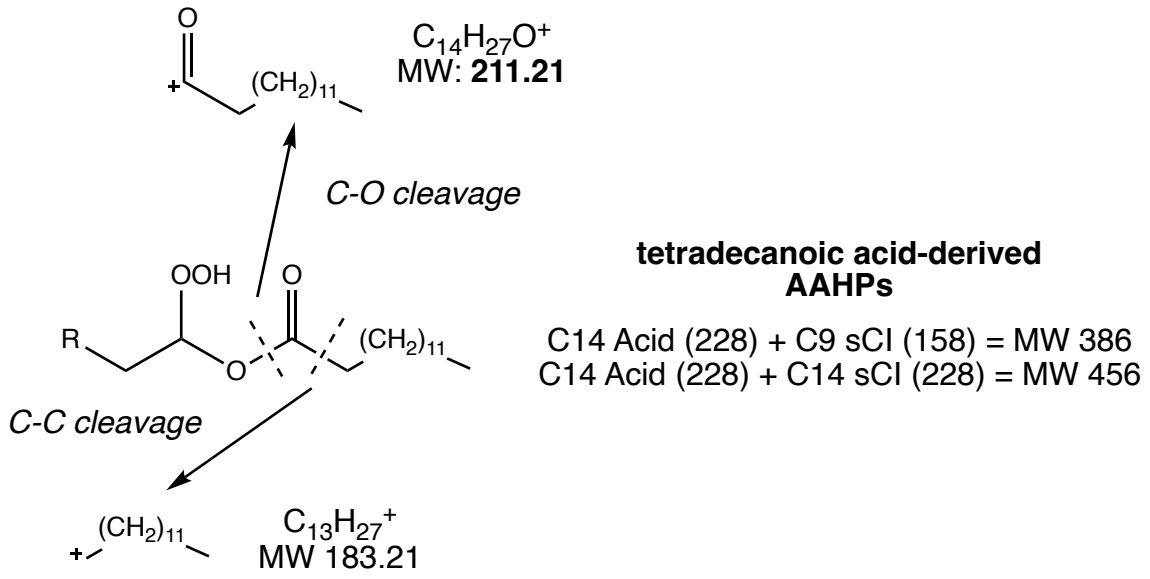

Scheme 3.S3. Proposed fragmentation schemes of AAHPs derived from tetradecanoic acid ($C_{14}H_{28}O_2$, MW 228) reacting with the C_9 and C_{14} sCI.

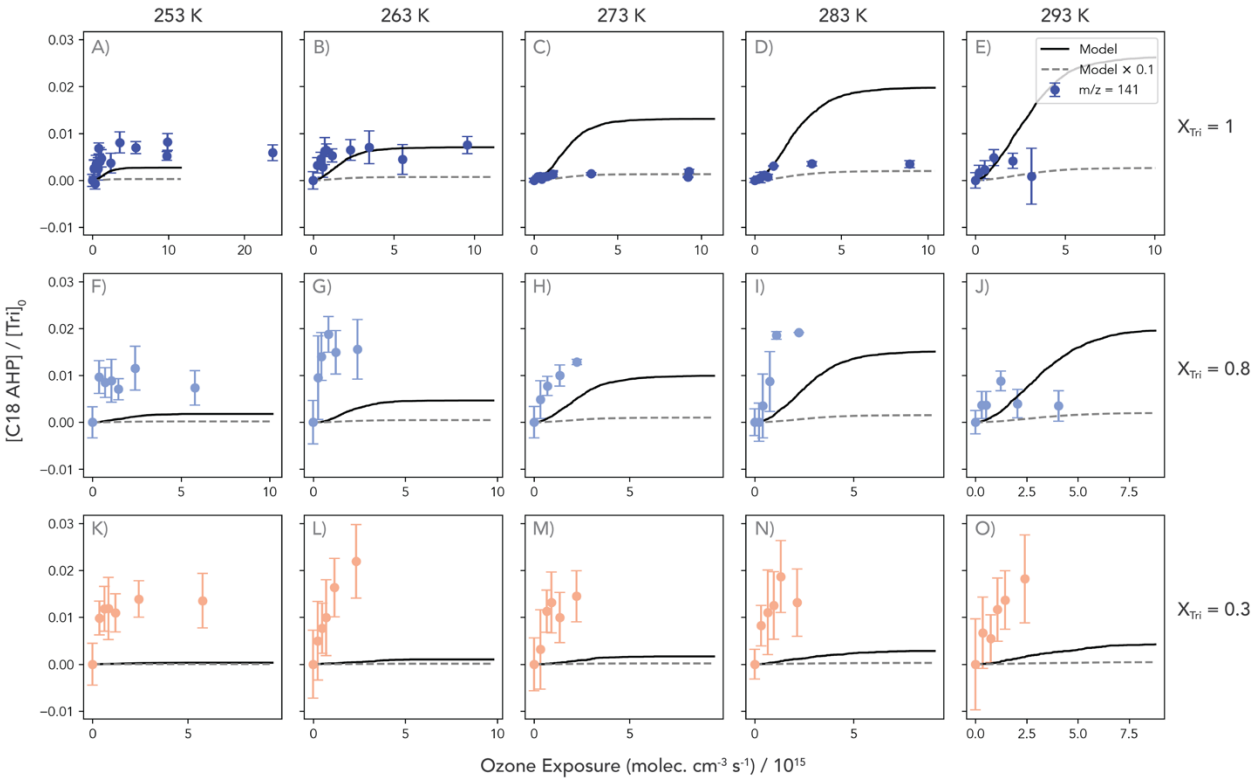

Figure 3.S7. Observed kinetics of the *m/z* = 141 peak, identified as a fragment of the C_9 acid derived C_{18}-AAHP, normalized to the initial intensity of the Tri peak (*m/z* = 322) for each experimental condition. Predicted kinetics of the C_{18} AAHP normalized to initial Tri concentration ($[Tri]_0$) from the explicit kinetic simulations, as well as the prediction scaled down by a factor of 10, have been overlaid for comparison.

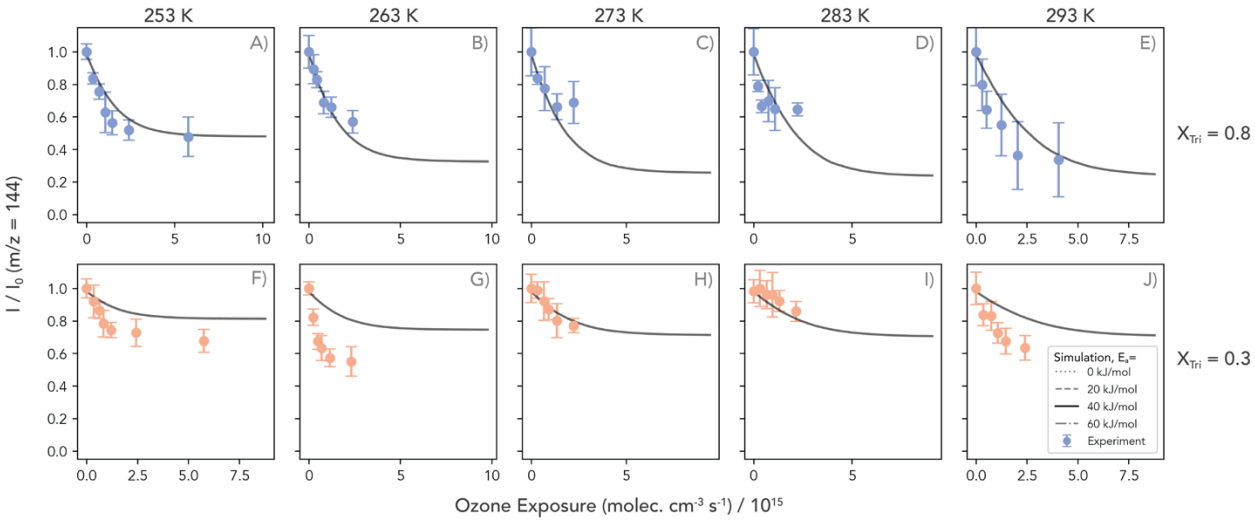

Figure 3.S8. Decay kinetics of *m/z* = 144, identified as a C_8 fragment of HDA (see Figure 3.2 and Experimental section). Organized by increasing temperature (columns, left to right) and initial HDA concentration/X_{Tri} (rows, top to bottom), as labeled.

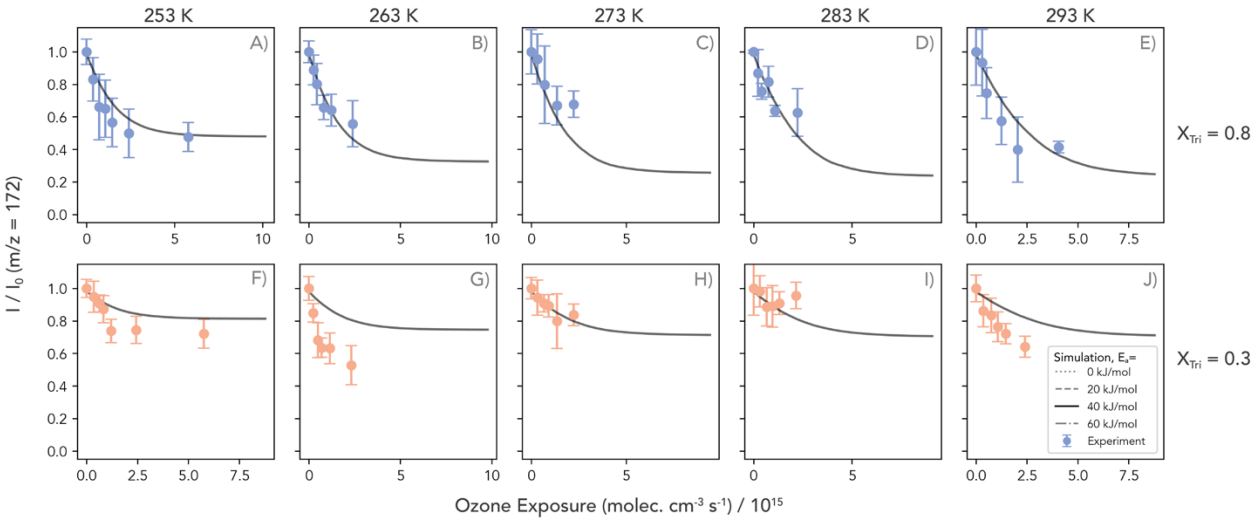

Figure 3.S9. Decay kinetics of *m/z* = 172, identified as a C_{10} fragment of HDA (see Figure 2 and Experimental section). Organized by increasing temperature (columns, left to right) and initial HDA concentration/X_{Tri} (rows, top to bottom), as labeled.

Table 3.S2. Arrhenius parameters for k_{AAHP} corresponding to the values of activation energy (E_a) considered in this study.

E_a (kJ mol^{-1})	A (cm^3 molec.$^{-1}$ sec.$^{-1}$)	k (293.15 K)	k (253.15 K)	$k_{CI+acid}$(253 K) / $k_{CI+acid}$(293 K)
0	2.10 x 10^{-19}	2.10 x 10^{-19}	2.10 x 10^{-19}	1.00
20	7.69 x 10^{-16}	2.10 x 10^{-19}	5.74 x 10^{-20}	0.27
40	2.82 x 10^{-12}	2.10 x 10^{-19}	1.57 x 10^{-20}	0.07
60	1.03 x 10^{-8}	2.10 x 10^{-19}	4.29 x 10^{-21}	0.02

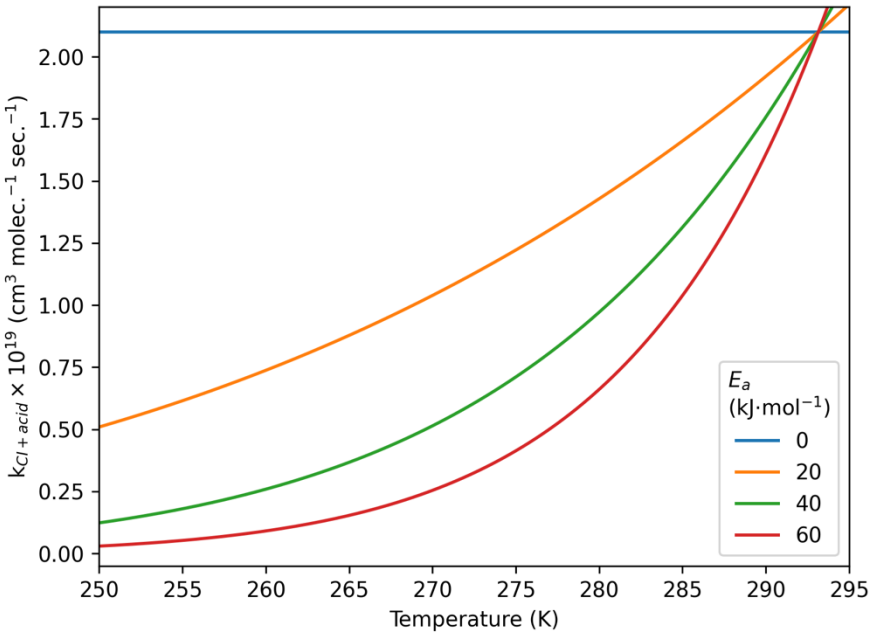

Figure 3.S10. k_{AAHP} as a function of temperature for each of the choices of Arrhenius parameters outlined in Table 3.S2.

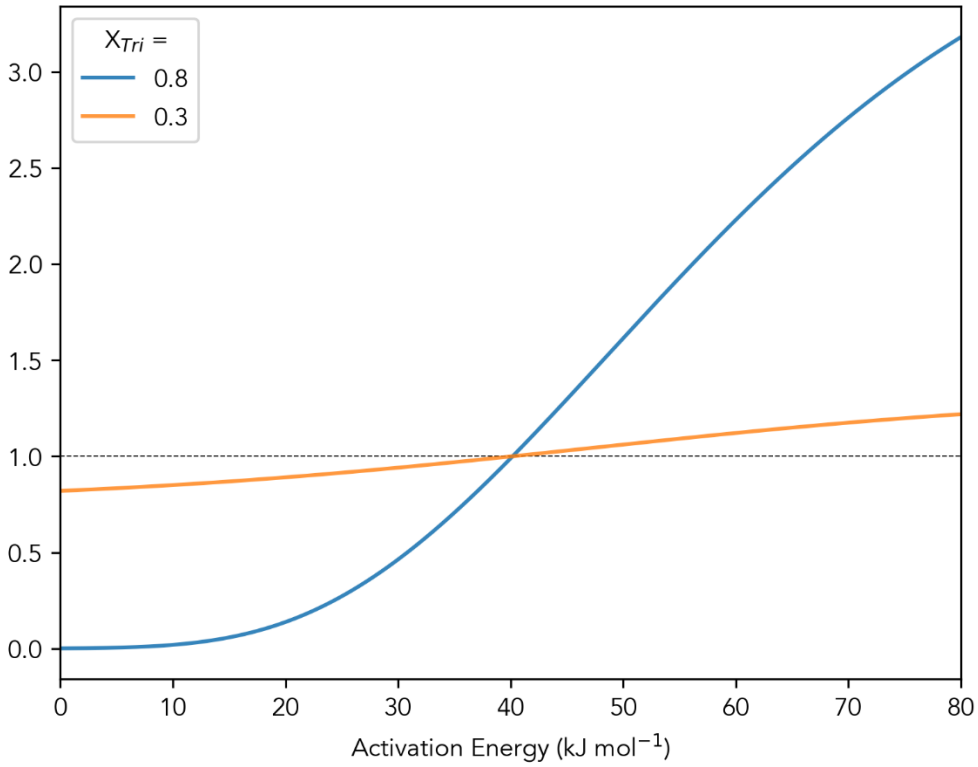

Figure 3.S11. Ratio of $[HDA]_{\infty}^{(T=263K)}$ to $[HDA]_{\infty}^{(T=293K)}$, the asymptotic values of the HDA decay at 263 and 293 K respectively, as a function of the activation energy (E_a) of k_{AAHP}. The dotted horizontal line denotes a ratio of 1, indicating no net change in the extent of the HDA decay between these two temperatures. $[HDA]_{\infty}$ is calculated by finding the infinite-time limit of Equation 6 from Reynolds and Wilson:[29]

$$[HDA]_{\infty} = \frac{1}{k'} W_0\left(k' \cdot e^{\frac{k' \cdot (2X_{Tri}-1)}{X_{Tri}-1}}\right) \qquad \text{Eq. (3.S13)}$$

where k' is the temperature-dependent branching ratio between unimolecular and bimolecular sCI reactions as defined in the main text of Reynolds and Wilson (Equation 7). Plots for both X_{Tri}=0.8 and X_{Tri}=0.3 have been overlaid to indicate the relative sensitivity to the value of E_a in each initial condition.

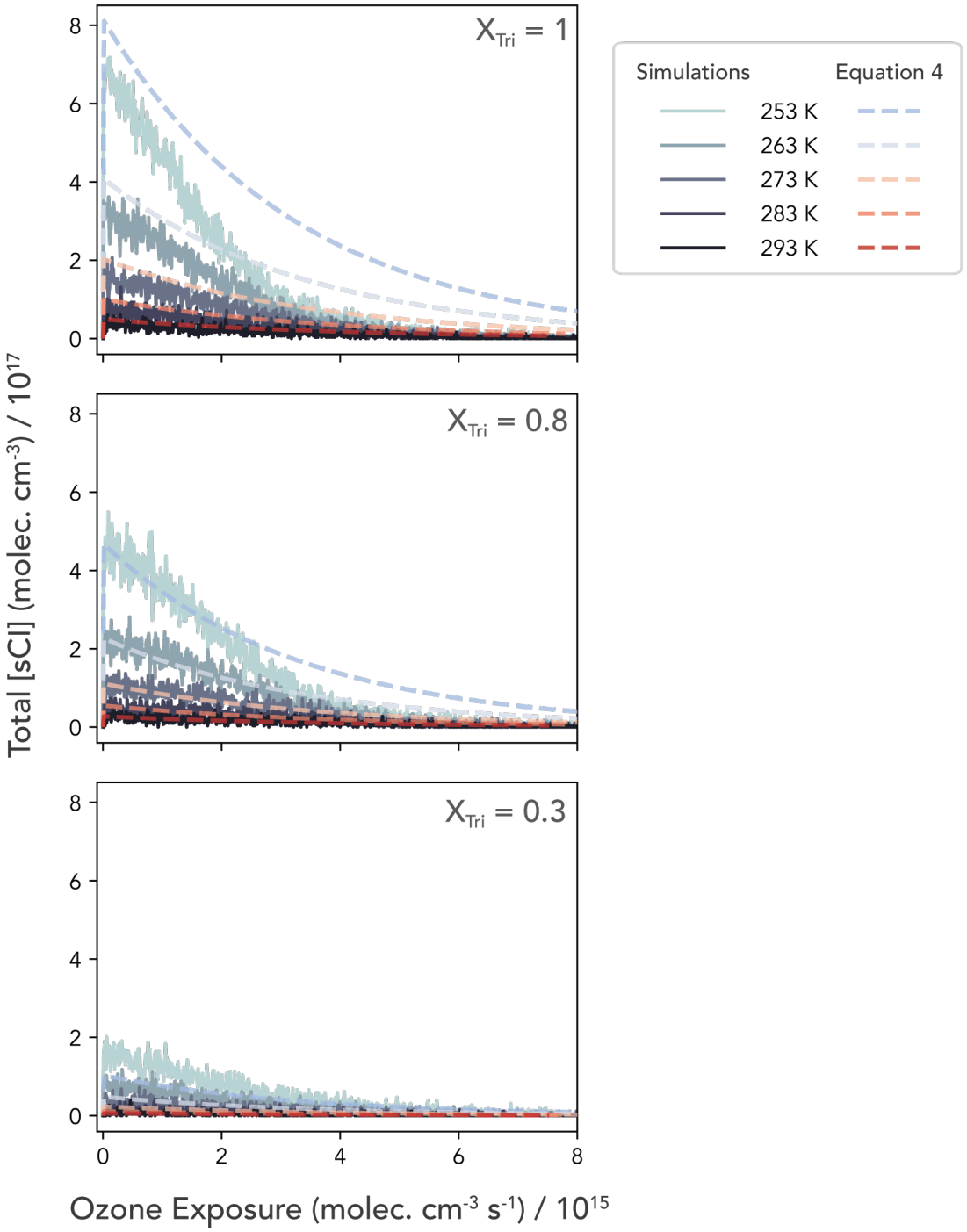

Figure 3.S12. Predicted total concentrations of the stabilized Criegee Intermediate (sCI) from simulations (solid plots, showing stochastic noise) and the analytical expression derived in Equation 3.4 in the Discussion (dotted lines) as a function of ozone exposure. Line color indicates temperature, as denoted in the legend.

3.7. References

(1) Finlayson-Pitts, B. J.; Pitts, J. N. *Chemistry of the Upper and Lower Atmosphere: Theory, Experiments, and Applications*; Academic Press: San Diego, 2000.

(2) Worsnop, D. R.; Morris, J. W.; Shi, Q.; Davidovits, P.; Kolb, C. E. A Chemical Kinetic Model for Reactive Transformations of Aerosol Particles: REACTIVE TRANSFORMATION OF AEROSOL PARTICLES. *Geophys. Res. Lett.* **2002**, *29* (20), 57-1-57–4. https://doi.org/10.1029/2002GL015542.

(3) Wilson, K. R.; Prophet, A. M.; Willis, M. D. A Kinetic Model for Predicting Trace Gas Uptake and Reaction. *J. Phys. Chem. A* **2022**, *126* (40), 7291–7308. https://doi.org/10.1021/acs.jpca.2c03559.

(4) Davies, J. F.; Wilson, K. R. Nanoscale Interfacial Gradients Formed by the Reactive Uptake of OH Radicals onto Viscous Aerosol Surfaces. *Chem. Sci.* **2015**, *6* (12), 7020–7027. https://doi.org/10.1039/C5SC02326B.

(5) Reid, J. P.; Bertram, A. K.; Topping, D. O.; Laskin, A.; Martin, S. T.; Petters, M. D.; Pope, F. D.; Rovelli, G. The Viscosity of Atmospherically Relevant Organic Particles. *Nature Communications* **2018**, *9* (1), 1–14. https://doi.org/10.1038/s41467-018-03027-z.

(6) Slade, J. H.; Ault, A. P.; Bui, A. T.; Ditto, J. C.; Lei, Z.; Bondy, A. L.; Olson, N. E.; Cook, R. D.; Desrochers, S. J.; Harvey, R. M.; Erickson, M. H.; Wallace, H. W.; Alvarez, S. L.; Flynn, J. H.; Boor, B. E.; Petrucci, G. A.; Gentner, D. R.; Griffin, R. J.; Shepson, P. B. Bouncier Particles at Night: Biogenic Secondary Organic Aerosol Chemistry and Sulfate Drive Diel Variations in the Aerosol Phase in a Mixed Forest. *Environ. Sci. Technol.* **2019**, *53* (9), 4977–4987. https://doi.org/10.1021/acs.est.8b07319.

(7) Kaur Kohli, R.; Reynolds, R. S.; Wilson, K. R.; Davies, J. F. Exploring the Influence of Particle Phase in the Ozonolysis of Oleic and Elaidic Acid. *Aerosol Science and Technology* **2024**, *58* (4), 356–373. https://doi.org/10.1080/02786826.2023.2226183.

(8) Berkemeier, T.; Mishra, A.; Mattei, C.; Huisman, A. J.; Krieger, U. K.; Pöschl, U. Ozonolysis of Oleic Acid Aerosol Revisited: Multiphase Chemical Kinetics and Reaction Mechanisms. *ACS Earth Space Chem.* **2021**, *5* (12), 3313–3323. https://doi.org/10.1021/acsearthspacechem.1c00232.

(9) Willis, M. D.; Wilson, K. R. Coupled Interfacial and Bulk Kinetics Govern the Timescales of Multiphase Ozonolysis Reactions. *J. Phys. Chem. A* **2022**, *126* (30), 4991–5010. https://doi.org/10.1021/acs.jpca.2c03059.

(10) Tobias, H. J.; Ziemann, P. J. Thermal Desorption Mass Spectrometric Analysis of Organic Aerosol Formed from Reactions of 1-Tetradecene and O3 in the Presence of Alcohols and Carboxylic Acids. *Environ. Sci. Technol.* **2000**, *34* (11), 2105–2115. https://doi.org/10.1021/es9907156.

(11) Ziemann, P. J. Aerosol Products, Mechanisms, and Kinetics of Heterogeneous Reactions of Ozone with Oleic Acid in Pure and Mixed Particles. *Faraday Discuss.* **2005**, *130* (0), 469–490. https://doi.org/10.1039/B417502F.

(12) Wang, M.; Yao, L.; Zheng, J.; Wang, X.; Chen, J.; Yang, X.; Worsnop, D. R.; Donahue, N. M.; Wang, L. Reactions of Atmospheric Particulate Stabilized Criegee Intermediates Lead to High-Molecular-Weight Aerosol Components. *Environ. Sci. Technol.* **2016**, *50* (11), 5702–5710. https://doi.org/10.1021/acs.est.6b02114.

(13) Heine, N.; Houle, F. A.; Wilson, K. R. Connecting the Elementary Reaction Pathways of Criegee Intermediates to the Chemical Erosion of Squalene Interfaces during Ozonolysis. *Environ. Sci. Technol.* **2017**, *51* (23), 13740–13748. https://doi.org/10.1021/acs.est.7b04197.

(14) Li, J.; Forrester, S. M.; Knopf, D. A. Heterogeneous Oxidation of Amorphous Organic Aerosol Surrogates by O_3, NO_3, and OH at Typical Tropospheric Temperatures. *Atmospheric Chemistry and Physics* **2020**, *20* (10), 6055–6080. https://doi.org/10.5194/acp-20-6055-2020.

(15) Liu, W.; He, L.; Liu, Y.; Liao, K.; Chen, Q.; Kuwata, M. Suppressed Atmospheric Chemical Aging of Cooking Organic Aerosol Particles in Wintertime Conditions. *Atmos. Chem. Phys.* **2024**, *24* (9), 5625–5636. https://doi.org/10.5194/acp-24-5625-2024.

(16) Moschos, V.; Dzepina, K.; Bhattu, D.; Lamkaddam, H.; Casotto, R.; Daellenbach, K. R.; Canonaco, F.; Rai, P.; Aas, W.; Becagli, S.; Calzolai, G.; Eleftheriadis, K.; Moffett, C. E.; Schnelle-Kreis, J.; Severi, M.; Sharma, S.; Skov, H.; Vestenius, M.; Zhang, W.; Hakola, H.; Hellén, H.; Huang, L.; Jaffrezo, J.-L.; Massling, A.; Nøjgaard, J. K.; Petäjä, T.; Popovicheva, O.; Sheesley, R. J.; Traversi, R.; Yttri, K. E.; Schmale, J.; Prévôt, A. S. H.; Baltensperger, U.; El Haddad, I. Equal Abundance of Summertime Natural and Wintertime Anthropogenic Arctic Organic Aerosols. *Nat. Geosci.* **2022**, *15* (3), 196–202. https://doi.org/10.1038/s41561-021-00891-1.

(17) Su, B.; Zhang, G.; Song, C.; Liang, Y.; Wang, L.; Li, L.; Zhou, Z.; Yan, J.; Wang, X.; Bi, X. Submicron Organic Aerosol Types in the Summertime Arctic: Mixing State, Geographic Distribution, and Drivers. *JGR Atmospheres* **2024**, *129* (17), e2024JD041061. https://doi.org/10.1029/2024JD041061.

(18) Razumovskii, S. D.; Zaikov, G. E. The Solubility of Ozone in Various Solvents. *Russ Chem Bull* **1971**, *20* (4), 616–620. https://doi.org/10.1007/BF00853885.

(19) Biń, A. K. Ozone Solubility in Liquids. *Ozone: Science & Engineering* **2006**, *28* (2), 67–75. https://doi.org/10.1080/01919510600558635.

(20) Panich, N. M.; Ershov, B. G. Solubility of Ozone in Organic Solvents. *Russ J Gen Chem* **2019**, *89* (2), 185–189. https://doi.org/10.1134/S1070363219020026.

(21) Atkinson, R.; Baulch, D. L.; Cox, R. A.; Crowley, J. N.; Hampson, R. F.; Hynes, R. G.; Jenkin, M. E.; Rossi, M. J.; Troe, J.; IUPAC Subcommittee. Evaluated Kinetic and Photochemical Data for Atmospheric Chemistry: Volume II – Gas Phase Reactions of Organic Species. *Atmos. Chem. Phys.* **2006**, *6* (11), 3625–4055. https://doi.org/10.5194/acp-6-3625-2006.

(22) Vereecken, L.; Novelli, A.; Taraborrelli, D. Unimolecular Decay Strongly Limits the Atmospheric Impact of Criegee Intermediates. *Phys. Chem. Chem. Phys.* **2017**, *19* (47), 31599–31612. https://doi.org/10.1039/C7CP05541B.

(23) Lester, M. I.; Klippenstein, S. J. Unimolecular Decay of Criegee Intermediates to OH Radical Products: Prompt and Thermal Decay Processes. *Acc. Chem. Res.* **2018**, *51* (4), 978–985. https://doi.org/10.1021/acs.accounts.8b00077.

(24) Long, B.; Bao, J. L.; Truhlar, D. G. Rapid Unimolecular Reaction of Stabilized Criegee Intermediates and Implications for Atmospheric Chemistry. *Nat Commun* **2019**, *10* (1), 2003. https://doi.org/10.1038/s41467-019-09948-7.

(25) Vereecken, L.; Novelli, A.; Kiendler-Scharr, A.; Wahner, A. Unimolecular and Water Reactions of Oxygenated and Unsaturated Criegee Intermediates under Atmospheric Conditions. *Physical Chemistry Chemical Physics* **2022**, *24* (11), 6428–6443. https://doi.org/10.1039/D1CP05877K.

(26) Krüger, M.; Mishra, A.; Spichtinger, P.; Pöschl, U.; Berkemeier, T. A Numerical Compass for Experiment Design in Chemical Kinetics and Molecular Property Estimation. *J Cheminform* **2024**, *16* (1), 34. https://doi.org/10.1186/s13321-024-00825-0.

(27) Welz, O.; Eskola, A. J.; Sheps, L.; Rotavera, B.; Savee, J. D.; Scheer, A. M.; Osborn, D. L.; Lowe, D.; Murray Booth, A.; Xiao, P.; Anwar H. Khan, M.; Percival, C. J.; Shallcross, D. E.; Taatjes, C. A. Rate Coefficients of C1 and C2 Criegee Intermediate Reactions with Formic and Acetic Acid Near the Collision Limit: Direct Kinetics Measurements and Atmospheric Implications. *Angewandte Chemie* **2014**, *126* (18), 4635–4638. https://doi.org/10.1002/ange.201400964.

(28) Vereecken, L. The Reaction of Criegee Intermediates with Acids and Enols. *Phys. Chem. Chem. Phys.* **2017**, *19* (42), 28630–28640. https://doi.org/10.1039/C7CP05132H.

(29) Reynolds, R.; Ahmed, M.; Wilson, K. R. Constraining the Reaction Rate of Criegee Intermediates with Carboxylic Acids during the Multiphase Ozonolysis of Aerosolized Alkenes. *ACS Earth Space Chem.* **2023**. https://doi.org/10.1021/acsearthspacechem.3c00026.

(30) Gloaguen, E.; Mysak, E. R.; Leone, S. R.; Ahmed, M.; Wilson, K. R. Investigating the Chemical Composition of Mixed Organic–Inorganic Particles by "Soft" Vacuum Ultraviolet Photoionization: The Reaction of Ozone with Anthracene on Sodium Chloride Particles. *International Journal of Mass Spectrometry* **2006**, *258* (1–3), 74–85. https://doi.org/10.1016/j.ijms.2006.07.019.

(31) Hinsberg, W. D.; Houle, F. A. Kinetiscope – A Stochastic Kinetics Simulator, 2020. http://hinsberg.net/kinetiscope.

(32) Zeng, M.; Wilson, K. R. Efficient Coupling of Reaction Pathways of Criegee Intermediates and Free Radicals in the Heterogeneous Ozonolysis of Alkenes. *J. Phys. Chem. Lett.* **2020**, *11* (16), 6580–6585. https://doi.org/10.1021/acs.jpclett.0c01823.

(33) Gibbs, A. Physical Properties of Insect Cuticular Hydrocarbons: Model Mixtures and Lipid Interactions. *Comparative Biochemistry and Physiology Part B: Biochemistry and Molecular Biology* **1995**, *112* (4), 667–672. https://doi.org/10.1016/0305-0491(95)00119-0.

(34) Hearn, J. D.; Smith, G. D. Measuring Rates of Reaction in Supercooled Organic Particles with Implications for Atmospheric Aerosol. *Physical Chemistry Chemical Physics* **2005**, *7* (13), 2549–2551. https://doi.org/10.1039/B506424D.

(35) Katrib, Y.; Biskos, G.; Buseck, P. R.; Davidovits, P.; Jayne, J. T.; Mochida, M.; Wise, M. E.; Worsnop, D. R.; Martin, S. T. Ozonolysis of Mixed Oleic-Acid/Stearic-Acid Particles: Reaction Kinetics and Chemical Morphology. *J. Phys. Chem. A* **2005**, *109* (48), 10910–10919. https://doi.org/10.1021/jp054714d.

(36) *2-Hexyldecanoic Acid*; SDS No. 464449; Sigma-Aldrich: St. Louis, MO, 2024. https://www.sigmaaldrich.com/US/en/sds/Aldrich/464449 (accessed 2024-07-31).

(37) Wells, J. R.; Morrison, G. C.; Coleman, B. K.; Spicer, C.; Dean, S. W. Kinetics and Reaction Products of Ozone and Surface-Bound Squalene. *J. ASTM Int.* **2008**, *5* (7), 101629. https://doi.org/10.1520/JAI101629.

(38) Donahue, N. M.; Drozd, G. T.; Epstein, S. A.; Presto, A. A.; Kroll, J. H. Adventures in Ozoneland: Down the Rabbit-Hole. *Physical Chemistry Chemical Physics* **2011**, *13* (23), 10848–10857. https://doi.org/10.1039/C0CP02564J.

(39) Cremer, D. Theoretical Determination of Molecular Structure and Conformation. 7. Stereoselectivity of the Ozonolysis Reaction. *J. Am. Chem. Soc.* **1981**, *103* (13), 3619–3626. https://doi.org/10.1021/ja00403a001.

(40) Taatjes, C. A. Criegee Intermediates: What Direct Production and Detection Can Teach Us About Reactions of Carbonyl Oxides. *Annu. Rev. Phys. Chem.* **2017**, *68* (1), 183–207. https://doi.org/10.1146/annurev-physchem-052516-050739.

(41) Gallimore, P. J.; Griffiths, P. T.; Pope, F. D.; Reid, J. P.; Kalberer, M. Comprehensive Modeling Study of Ozonolysis of Oleic Acid Aerosol Based on Real-Time, Online Measurements of Aerosol Composition. *Journal of Geophysical Research: Atmospheres* **2017**, *122* (8), 4364–4377. https://doi.org/10.1002/2016JD026221.

(42) Liu, W.; Liao, K.; Chen, Q.; He, L.; Liu, Y.; Kuwata, M. Existence of Crystalline Ammonium Sulfate Nuclei Affects Chemical Reactivity of Oleic Acid Particles Through Heterogeneous Nucleation. *JGR Atmospheres* **2023**, *128* (12), e2023JD038675. https://doi.org/10.1029/2023JD038675.

(43) Atkinson, R. Estimations of OH Radical Rate Constants from H-Atom Abstraction from C–H and O–H Bonds over the Temperature Range 250-1000 K. *International Journal of Chemical Kinetics* **1986**, *18* (5), 555–568. https://doi.org/10.1002/kin.550180506.

(44) Denisov, E. T.; Afanas'ev, I. B. *Oxidation and Antioxidants in Organic Chemistry and Biology.*; Taylor & Frances: Oxford, 2005.

(45) Peeters, J.; Boullart, W.; Pultau, V.; Vandenberk, S.; Vereecken, L. Structure−Activity Relationship for the Addition of OH to (Poly)Alkenes: Site-Specific and Total Rate Constants. *J. Phys. Chem. A* **2007**, *111* (9), 1618–1631. https://doi.org/10.1021/jp066973o.

(46) Sazhina, N. N.; Evteeva, N. M.; Titov, V. N. Experimental Evaluation of Velocity Constants for Ozone Interaction with Individual Fatty Acids. *Bull Exp Biol Med* **2018**, *165* (3), 356–359. https://doi.org/10.1007/s10517-018-4169-8.

(47) Atkinson, R. Gas-Phase Tropospheric Chemistry of Volatile Organic Compounds: 1. Alkanes and Alkenes. *Journal of Physical and Chemical Reference Data* **1997**, *26* (2), 215–290. https://doi.org/10.1063/1.556012.

(48) von Domaros, M.; Lakey, P. S. J.; Shiraiwa, M.; Tobias, D. J. Multiscale Modeling of Human Skin Oil-Induced Indoor Air Chemistry: Combining Kinetic Models and Molecular Dynamics. *J. Phys. Chem. B* **2020**, *124* (18), 3836–3843. https://doi.org/10.1021/acs.jpcb.0c02818.

(49) Li, W.; Pak, C. Y.; Tse, Y.-L. S. Free Energy Study of H2O, N2O5, SO2, and O3 Gas Sorption by Water Droplets/Slabs. *The Journal of Chemical Physics* **2018**, *148* (16), 164706. https://doi.org/10.1063/1.5022389.

(50) Garza, A. J. Solvation Entropy Made Simple. *J. Chem. Theory Comput.* **2019**, *15* (5), 3204–3214. https://doi.org/10.1021/acs.jctc.9b00214.

(51) *Cis-Tricos-9-Ene*; Directive 98/8/EC; Assessment Report Product-type 19 (Repellents and Attractants); European Chemicals Agency (ECHA): Helsinki, Finland, 2012. https://echa.europa.eu/documents/10162/47e4aff7-3a1c-ea39-f501-368d5b161b56 (accessed 2024-09-05).

(52) Smith, G. D.; Woods, E.; DeForest, C. L.; Baer, T.; Miller, R. E. Reactive Uptake of Ozone by Oleic Acid Aerosol Particles: Application of Single-Particle Mass Spectrometry to Heterogeneous Reaction Kinetics. *J. Phys. Chem. A* **2002**, *106* (35), 8085–8095. https://doi.org/10.1021/jp020527t.

(53) Lee, L.; Wilson, K. The Reactive–Diffusive Length of OH and Ozone in Model Organic Aerosols. *J. Phys. Chem. A* **2016**, *120* (34), 6800–6812. https://doi.org/10.1021/acs.jpca.6b05285.

(54) Li, J.; Knopf, D. A. Representation of Multiphase OH Oxidation of Amorphous Organic Aerosol for Tropospheric Conditions. *Environ. Sci. Technol.* **2021**, acs.est.0c07668. https://doi.org/10.1021/acs.est.0c07668.

(55) Verevkin, S. P.; Krasnykh, E. L.; Vasiltsova, T. V.; Koutek, B.; Doubsky, J.; Heintz, A. Vapor Pressures and Enthalpies of Vaporization of a Series of the Linear Aliphatic Aldehydes. *Fluid Phase Equilibria* **2003**, *206* (1–2), 331–339. https://doi.org/10.1016/S0378-3812(03)00035-9.

(56) Pankow, J. F. An Absorption Model of Gas/Particle Partitioning of Organic Compounds in the Atmosphere. *Atmospheric Environment* **1994**, *28* (2), 185–188. https://doi.org/10.1016/1352-2310(94)90093-0.

(57) Taatjes, C. A.; Welz, O.; Eskola, A. J.; Savee, J. D.; Osborn, D. L.; Lee, E. P. F.; Dyke, J. M.; Mok, D. W. K.; Shallcross, D. E.; Percival, C. J. Direct Measurement of Criegee Intermediate (CH 2 OO) Reactions with Acetone , Acetaldehyde , and Hexafluoroacetone. *Physical Chemistry Chemical Physics* **2012**, *14* (30), 10391–10400. https://doi.org/10.1039/C2CP40294G.

(58) Elsamra, R. M. I.; Jalan, A.; Buras, Z. J.; Middaugh, J. E.; Green, W. H. Temperature- and Pressure-Dependent Kinetics of CH2OO + CH3COCH3 and CH2OO + CH3CHO: Direct Measurements and Theoretical Analysis. *International Journal of Chemical Kinetics* **2016**, *48* (8), 474–488. https://doi.org/10.1002/kin.21007.

Chapter 4. Progress Toward Organocerium Photocatalysis in Aerosols

4.1 Background

Cerium photocatalysts have been identified as potentially useful agents for C-H activation due to their efficiency, earth-abundance, and low toxicity, and the ability to use visible light to initiate the catalytic cycle due to the availability of low-lying 4*f* to 5*d* transitions.[1–4] Their catalytic activity in solution can be driven by the reduction of cerium (IV) complexes to cerium (III) *via* ligand-to-metal charge transfer (LMCT), homolytically breaking a Ce–ligand bond and generating a radical species capable of hydrogen atom transfer (HAT) from a C–H bond.[4] In one recent example, gaseous ethane and methane were functionalized using a liquid-phase cerium (IV) photocatalyst with high turnover numbers.[3] However, many practical limitations remain to the use of such catalysts at scale to functionalize light hydrocarbons, including the need for high pressure feedstocks to increase reactant solubility in the liquid phase. In addition, the precise catalytic mechanism has itself been the subject of some controversy, with conflicting suggestions that the active species (i.e. the radical performing HAT) is either an alkoxy (RO) radical,[3,5] or a Cl atom produced from chloride salts used to generate the cerium (IV) catalyst *in situ*.[6]

Given these challenges, there are several potential benefits to developing an aerosolized methodology for catalyst delivery. Due to the high surface area to volume ratio of aerosols compared to bulk liquids, interactions between reactive gases and catalysts in the particle phase are increased, potentially reducing the pressures needed for feedstock gases to achieve desired concentrations in solution. This could couple Ce photocatalysis with the gas-liquid phase transfer catalysis recently demonstrated in organic aerosols.[7,8] Additionally, if a catalyst could be designed to produce surface-active Ce complexes, the catalytic efficiency (*i.e.* turnover number) could also be improved by reducing the timescale needed for an inactivated catalyst to be replaced at the particle surface from a reservoir of catalyst in the particle bulk. And finally, established aerosol analytical techniques, such as the measurement of uptake coefficients and the use of aerosol mass spectrometry to study particle-phase reactions, could provide a reliable way to measure kinetics, refine chemical mechanisms, and optimize the rate of reaction.

However, aerosolizing of Ce catalysts poses several key experimental challenges. First, Ce (IV) catalysts are typically sensitive to ambient oxygen, both in the form of water, and, in varying degrees, to atmospheric oxygen (O_2), necessitating control of at least relative humidity conditions during aerosol generation and reaction initiation. As such, non-aqueous solutions are generally a requirement, meaning organic solvents should be used for aerosol generation. Due to their generally high vapor pressures compared to water, and due to the impact of solvent choice on catalytic efficiency, organic solvents must be selected such that they allow for droplet nucleation while not interfering with reaction or detection. Finally, the reactants, products, and, ideally, the catalytic intermediates themselves should be detectible by analytical techniques such as mass spectrometry. In what follows, progress will be reported toward generation and characterization of Ce (IV) catalyst species in submicron organic solvent droplets.

4.2 Experimental Design and Description

The experimental design first revolved around the choice of model reaction, taking the experimental constraints listed above into account. With the suggestions and guidance of

collaborators, a candidate photocatalytic reaction was chosen from literature involving oxygenated reactants and products, as well as a directly-generated cerium (IV) catalytic species (Scheme 4.1).[9]

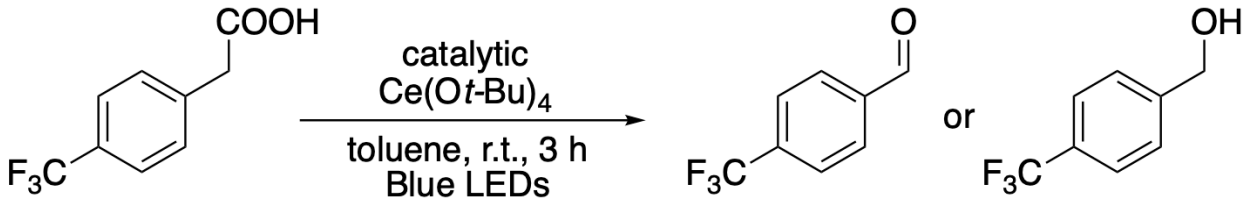

Scheme 4.1. The initial target reaction for this study, decarboxylative oxidation of a fluorine-substituted aryl acid using cerium (IV) *tert*-butoxide, resulting in either an aldehyde or an alcohol product, with corresponding conditions used in the bulk liquid phase to achieve reaction as reported by Shirase *et al.*[9]

This reaction, the decarboxylative oxidation of a carboxylic acid with an available C–H bond on the α-carbon, meets the requirements for detection, as the reactant (an aryl acid) and the products (either an aldehyde or an alcohol) should be detectable and distinguishable using ambient pressure ionization mass spectrometry techniques. Additionally, the catalyst, Ce(*t*-BuO)$_4$, where *t*-BuO is the *tert*-butoxide anion, is commercially available and resistant to O_2, requiring experimental control only over relative humidity. The aryl acid chosen for this experiment is the trifluoromethyl-substituted derivative of a species tested by Shirase *et al.* which showed high reaction efficiency (99% conversion), possibly due to its ability to stabilize the benzylic carbanion generated during decarboxylation *via* resonance effects. Thus, a first attempt was made to detect these reactants *via* mass spectrometry.

4.3 Results

4.3.A. Nanospray Ionization Mass Spectrometry of Reactants

Mass spectra were collected using a linear ion trap mass spectrometer (Velos Pro, ThermoFisher Scientific) fitted with a nanospray ionization (NSI) source. This ionization techinique is nearly identical to the electrospray ionization mass spectrometry (ESI-MS) used by Shirase *et al.* to characterize the reaction in their work,[9] up to a factor of the size of capillary and resulting droplet distribution produced during ionization. The mass spectra of solutions of interest were collected by directly infusing them into a commercially-available NSI source (ThermoFisher Scientific) using a syringe pump operating at a flow rate of 10 μL min^{-1}.

A mass spectrum of the reactant in Scheme 4.1 was first collected without any aerosolization or reaction prior to the ionization source. The aryl acid ($C_9H_7F_3O_2$, MW 204 g/mol) was dissolved in a methanol solution and the mass spectrum collected in negative polarity (Figure 4.1), which resulted in a deprotonation peak (m/z = 203.09), as well as a deprotonated acid dimer (m/z = 407.09) observed previously for carboxylic acids in ambient pressure ionization.[10] Additional peaks besides these were apparent but were not characterized, as they were suspected to be due to clustering with background organics present in the ionization region.

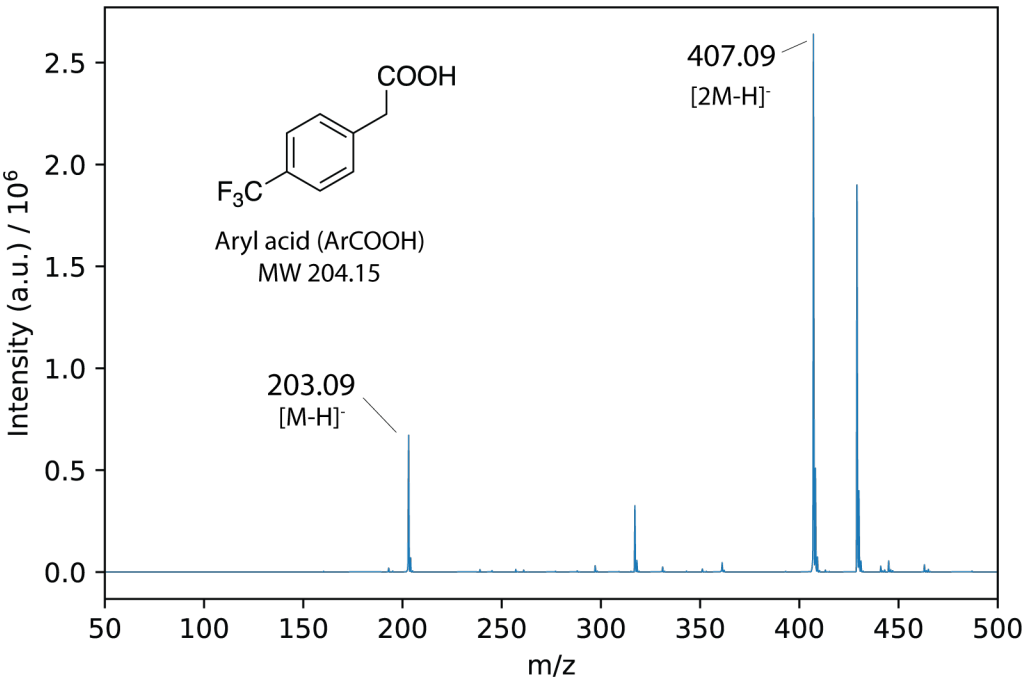

Figure 4.1. Negative ion NSI mass spectrum of the aryl acid (ArRCOOH) dissolved in methanol.

After validation of the expected reactant peaks, an attempt was made to observe Ce-acid complexes, as seen in Shirase *et al.*[9] However, when the Ce(*t*-BuO)$_4$ was added to the methanol solution, no new peaks were observed. This is likely due to a different solvent (methanol) than that used by Shirase, as pure toluene could not maintain a stable spray current in the NSI source. Unfortunately, solubility issues were encountered in mixed aryl acid and Ce(*t*-BuO)$_4$ solutions in multiple solvents and solvent combinations, resulting in precipitates forming in the syringe before they could be ionized by the NSI source or detected by the mass spectrometer. Additionally, attempts were made to irradiate the solution prior to spraying in order to potentially see reaction products, but no new peaks were observed.

As a result, the target reactant was changed to a saturated fatty acid, 2-hexyldecanoic acid (HDA, Scheme 4.2) used in previous studies.[10] HDA has the advantage of being highly soluble in organic solvents, as well as being a liquid at room temperature. Shirase *et al.* reported that carboxylic acids with similar chain length, including stearic and oleic acids, also undergo decarboxylative oxygenation in the presence of the Ce catalyst and blue light, with 80% and 79% total yields, respectively.[9] Since HDA has the required C–H bond available on the α-carbon to the acid head group, it is expected to undergo the same reaction as the aryl acid.

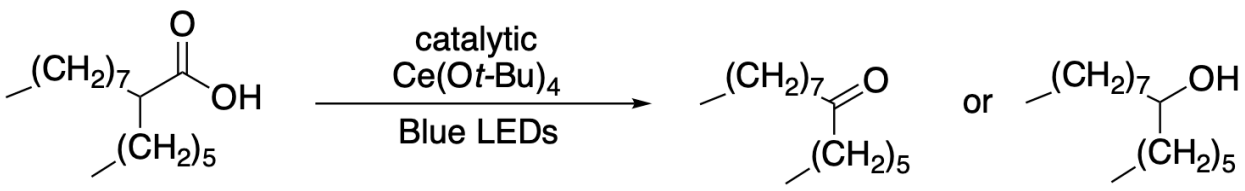

Scheme 4.2. The subsequent target reaction for this study, Ce-catalyzed decarboxylative oxidation of a lipid-like carboxylic acid, 2-hexyldecanoic acid (HDA), resulting in either a ketone or secondary alcohol product upon exposure to blue LEDs.

A mixture of HDA and Ce(*t*-BuO)$_4$ was prepared and introduced into the mass spectrometer *via* nanospray ionization in a mixture of 50% MeOH and hexanes to achieve a balance between stable spray current, ionization efficiency, and reactant solubility. The resulting mass spectrum of the HDA and Ce mixture is shown in Figure 4.2A.

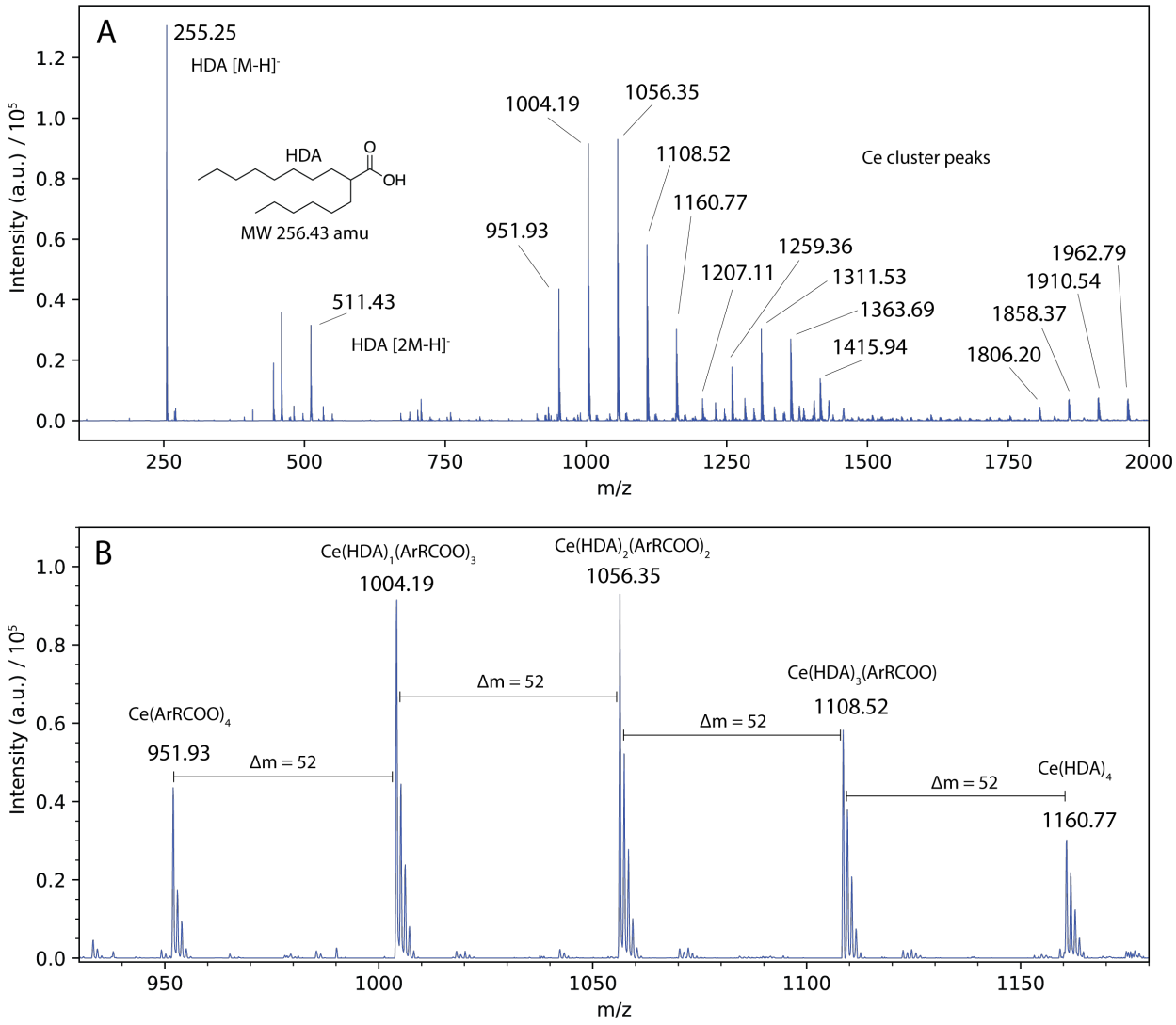

Figure 4.2. (A) NSI-MS spectra of a mixture of HDA and Ce(*t*-BuO)$_4$, showing the unclustered HDA peaks, as well as series of cluster peaks. (B) Enlarged view of the first series of peaks between *m/z* = 950 and 1170.

The expected peaks for HDA (deprotonation, *m/z* = 255.25, and singly-deprotonated acid dimer, *m/z* = 511.43) were observed, in addition to three series of peaks beginning at *m/z* = 951.93, 1259.36, and 1806.20. These peaks are observed uniquely in the presence of the Ce catalyst. Closer inspection of the first of these series (Figure 4.2B) reveals that each peak has at least 3 subsequent isotopic peaks separated by unit mass, indicating a singly-charged species, and that the mass difference between major peaks in the first series is consistent (Δm = 52). The number of peaks in this series (5) was suggestive of ligand exchange with a 4-coordinate Ce complex, given the stoichiometry of the catalyst. However the mass difference between peaks was unexpected, as this does not correspond to the mass difference between HDA and *t*-BuO ligands (Δm = 182). Upon investigation, however, it was discovered that there was significant contamination in the ionization region by the aryl acid from the previous reaction (Scheme 4.1). Although this background was undesirable, the remnant aryl acid proved advantageous for peak identification: the difference in mass between HDA and an aryl acid ligand (ArRCOO) is 52 amu, corresponding to the Δm in Figure 4.2B. The mass of a neutral Ce complex with four ArRCOO ligands is expected to be 952.68 amu, within a mass unit of the observed *m/z* = 951.93 in Figure 4.2B. Four ligand exchanges in this complex between ArRCOO and HDA (as illustrated in Scheme 4.3) would yield a series of 5 peaks, consistent with the observed mass separation. Thus, the high and low peaks in Figure 4.2B are assigned to Ce complexes with four HDA and ArRCOO ligands, respectively.

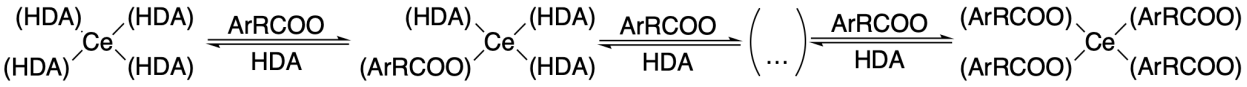

Scheme 4.3. Ligand exchange between HDA and ArRCOO in cerium (IV) complexes observed in the NSI mass spectrum (Figure 4.2).

As discussed in Chapter 2 on the ambient pressure chemical ionization (APCI) mass spectrometry of HDA, the HDA anion and easily clusters with other bulky organic molecules, acting as a soft ionizing agent. This mechanism can explain the nearby series of peaks in Figure 4.2A beginning at *m/z* = 1207.18, which is separated from the first peak in the previous series by a Δm of 255, corresponding to an HDA anion. Accordingly, the second series of peaks (*m/z* = 1207.11, 1259.36, 1311.53, 1363.69, 1415.94) is attributed to HDA anions clustering with the complexes outlined in Figure 4.2B and Scheme 2.

For the third series of peaks, only four peaks separated by Δm = 52are apparent (*m/z* = 1806.20, 1858.37, 1910.54, and 1962.79). However, the upper observation limit of the Velos Pro at the scan rate employed in this spectrum is *m/z* = 2000, meaning the expected final peak of the series, expected at *m/z* = 2014.96 if this were another 4-coordinate Ce complex, could not be observed in this spectrum. This peak will be discussed further in a following section using a higher mass range (Figure 4.4).

4.3.B. Generation and Characterization of Solvent Nanodroplets

After confirming that the reactants and Ce complexes could be observed with nanospray mass spectrometry, an attempt was made to observe the reactants in Scheme 4.2 in aerosols. Prior to aerosolizing the HDA and catalyst, the droplet distribution produced by various organic solvents

in an atomizer (Model 3076, TSI Inc.) was evaluated using a Scanning Mobility Particle Spectrometer (SMPS) composed of a Differential Mobility Analyzer (DMA 3080, TSI Inc.) connected to a Condensation Particle Counter (CPC 3025A, TSI Inc.) with *n*-butanol as its working reagent. Several candidate solvents were considered for aerosol generation before narrowing down to either hexanes or tetrahydrofuran (THF), chosen for their effectiveness in solvating the reactants and for the stability and size of the aerosols generated by each solvent. The particle size distributions resulting from atomizing hexanes and toluene are shown below.

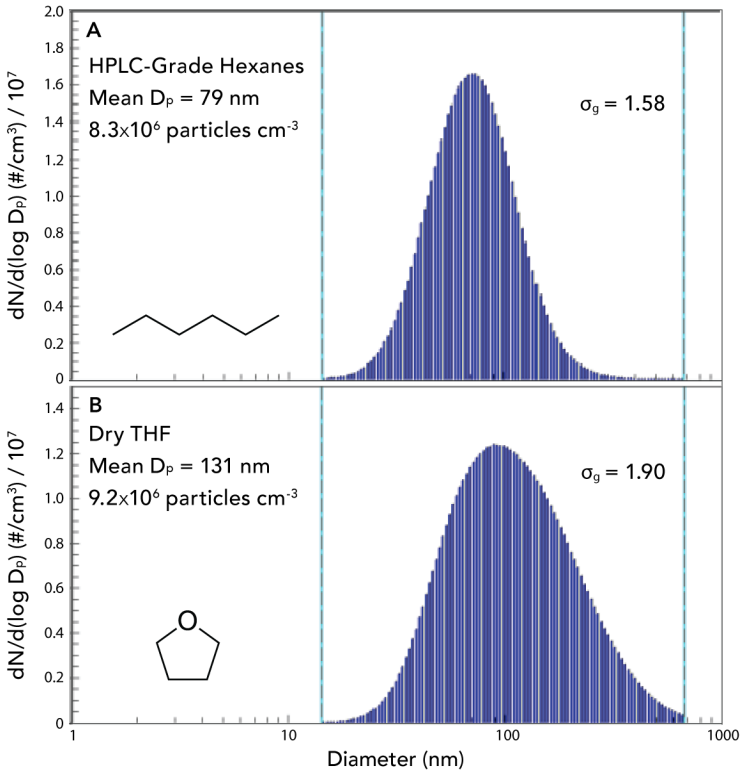

Figure 4.3. Particle size spectra recorded by SMPS for aerosol generated by atomizing (A) hexanes and (B) tetrahydrofuran (THF).

Due to the high vapor pressure of these solvents, it was expected that pure solvent droplets would evaporate away quickly. However, these solvent droplets were observed to persist in a flow tube reactor with a residence time of approximately 15 seconds, presumably due to the gas phase becoming quickly saturated with vapor, allowing for a gas-particle equilibrium to be established. Both aerosols size distributions have mean values near 100 nm, providing a high surface-to-volume ratio. Due to the slightly narrower size distribution of hexanes, as well as the ease of working with hexanes over THF, which requires more safety precautions, hexanes were chosen as the target solvent for aerosol catalyst experiments.

4.3.C. Characterization of Particle-Phase Ce-Ligand Complexes

After selection of a solvent, aerosol mass spectra were collected by crossing the hexane particle stream exiting the atomizer at a right angle to the negatively charged methanol beam

exiting the NSI source, analogous to an extractive electrospray technique.[11] The flow rates of MeOH, the spray voltage, and the position of the spray beam on a 3D stage were all optimized to achieve maximum signal from the incoming hexane droplets.

Initial attempts to directly observe Ce(*t*-BuO)$_4$ alone were unsuccessful, as for the direct NSI experiments; however, upon addition of HDA directly to the atomizer solution containing Ce(*t*-BuO)$_4$, the spectrum in Figure 4.4 was observed. Due to differences in the mass calibration of the Velos Pro between the scan range settings employed in Figures 4.2 and 4.4, a first-order correction to the mass calibration has been applied to the spectrum in Figure 4.4 to align with previously-identified *m/z* values.

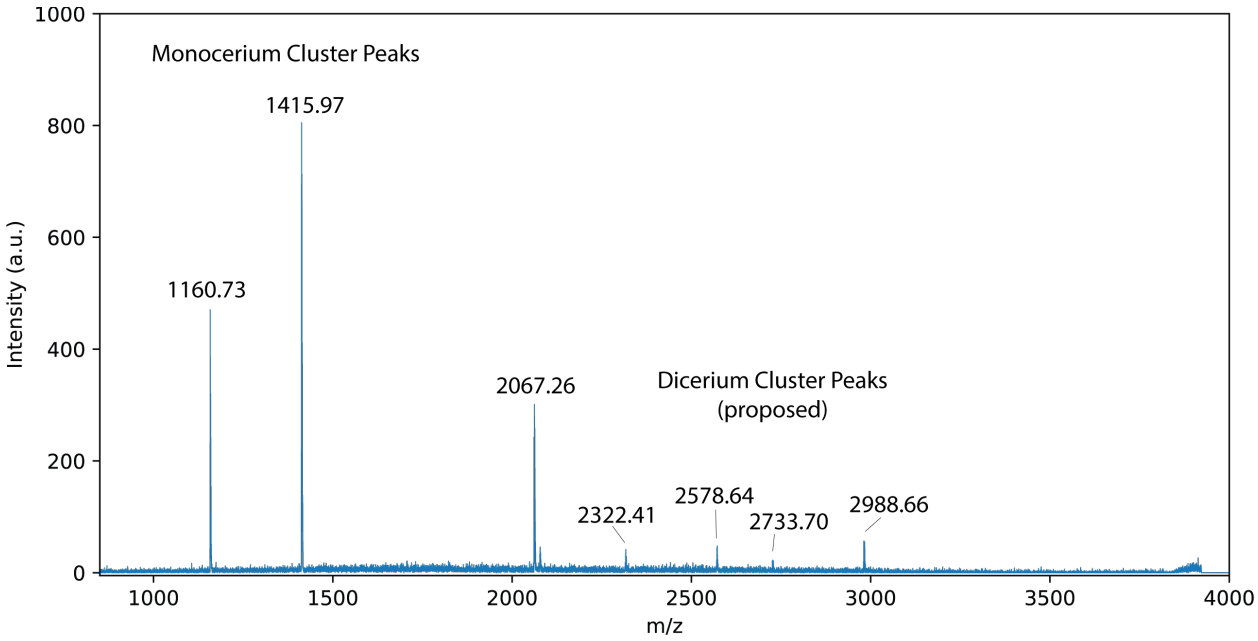

Figure 4.4. Negative ion polarity mass spectrum of the reactants in Scheme 4.2 in hexane aerosols, collected via an extractive electrospray technique. A first-order correction to the mass calibration has been applied to account for calibration differences between the scan range used here and that used to collect the spectrum in Figure 4.2.

The two most prominent peaks in Figure 4.4 align with peaks identified in Figure 4.2, namely *m/z* = 1160.73, corresponding to a 4-coordinate Ce(HDA)$_4$ complex, and *m/z* = 1415.97, corresponding to an HDA anion clustered with this complex. To confirm the identity of the first peak, a high-resolution scan was conducted on the isotopic peaks beginning at *m/z* = 1160.73, as displayed in Figure 4.5. Due to differences in mass calibration, a first-order correction was again applied to the result to bring it into agreement with the *m/z* values observed in Figure 4.2. The mass spectrum predicted by isotopic abundances of a neutral Ce(HDA)$_4$ complex was then calculated[12] and overlaid on the observed spectrum (Figure 4.5). Agreement between the observed and calculated spectra is excellent, with an absolute difference of less than 0.05 mass units at each value of *m/z*, as displayed in Table 4.1.

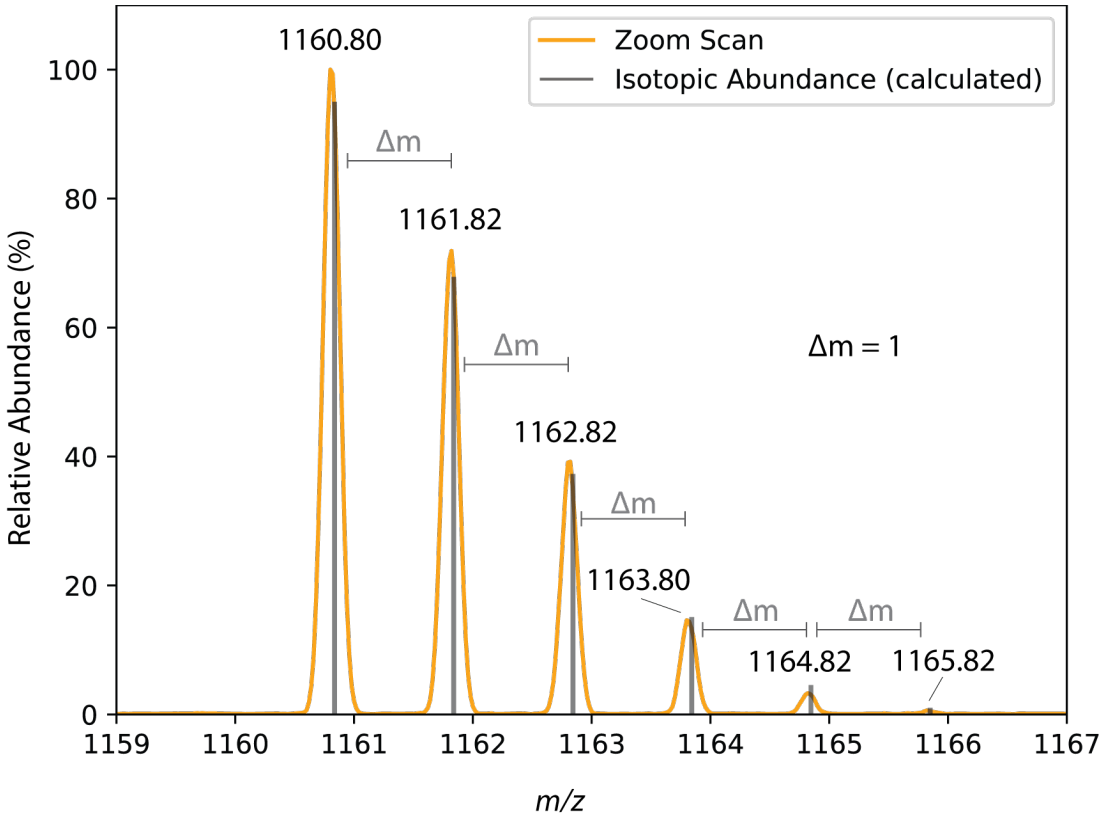

Figure 4.5. Zoom scan of peak cluster beginning at m/z = 1160.80, overlaid on the mass spectrum calculated from isotopic abundance for $Ce(HDA)_4$. Peaks are separated by unit mass.

Table 4.1. Comparison of observed peak positions and relative abundances to those predicted by isotopic abundance for the spectrum in Figure 4.5.

Observed *m/z* (Corrected)	**Calculated Isotope Mass (amu)**	**Mass Defect (amu)**	**Predicted Relative Abundance (%)**
1160.80	1160.835	0.035	100.0
1161.82	1161.838	0.018	71.4
1162.82	1162.842	0.022	39.3
1163.80	1163.842	0.042	15.9
1164.82	1164.846	0.026	4.8
1165.82	1165.849	0.029	1.1

In addition, two successive MS-MS experiments were performed to confirm the identities of the *m/z* =1416 and m/z=1161 (Figure 4.6). First, *m/z* = 1416.08 was selected in the ion trap of the Velos Pro (blue spectrum, far right of Figure 4.6) before being subjected to Collision Induced Dissociation (CID) *via* in-trap collisions with He gas. The normalized collision energy (NCE) was scanned until dissociation was complete; the spectrum at an NCE of 50 (arb. units) is shown in Figure 4.6. The resulting ion from these collisions was m/z = 1160.80, confirming that m/z = 1416.08 is a cluster with HDA anion. A second MS-MS experiment was then conducted by

selecting m/z = 1160.80 in the ion trap and subjecting it to CID at an NCE of 43. The primary peak yielded from this experiment was m/z = 922.56, a Δm of 238 mass units from the parent peak, which could correspond to a dehydration product of HDA. However, as only a fragment of an HDA ligand appears to be lost, this suggests that the carboxylate head groups of the HDA ligands in the complex at *m/z* = 1160.80 are bound more tightly to the Ce center, again consistent with *m/z* = 1160.80 being a 4-coordinate Ce (IV) complex.

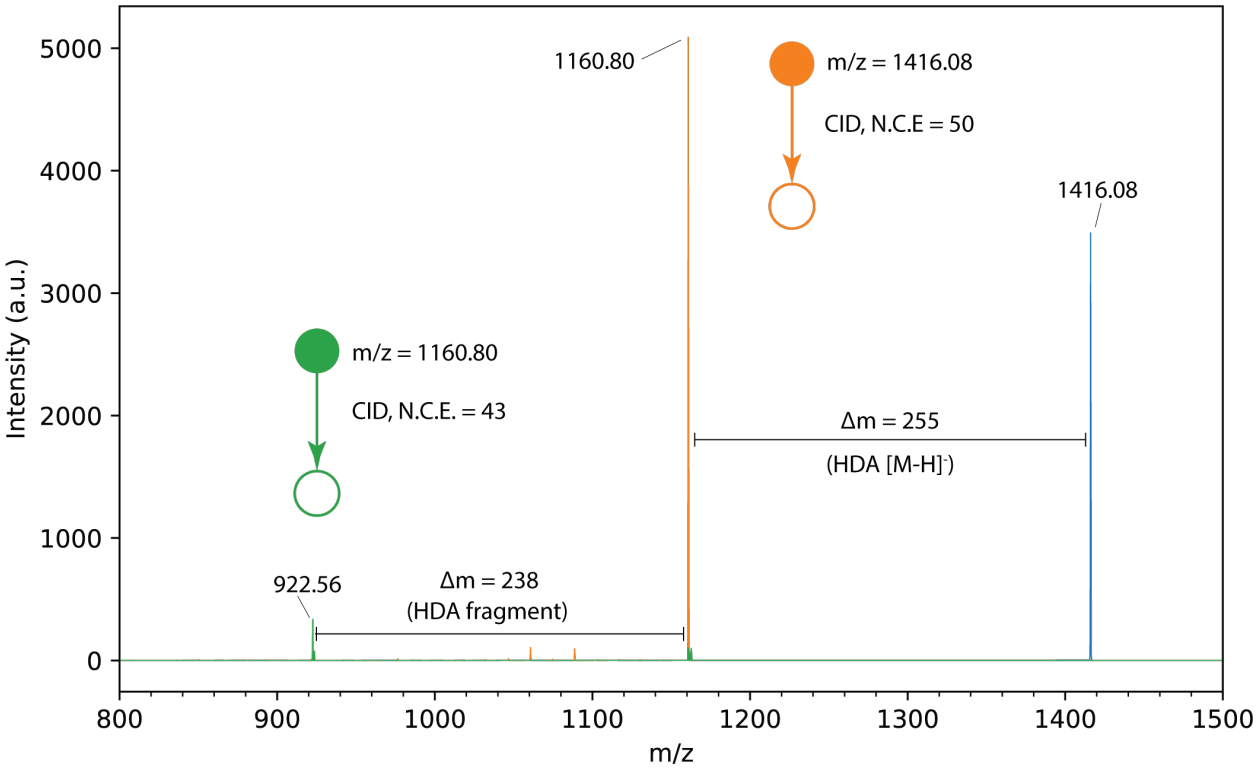

Figure 4.6. Results of successive MS/MS experiments under collision induced dissociation (CID). First, CID of *m/z* = 1416.08 (furthest to the right), yields *m/z* = 1160.80 (center). Second, CID of *m/z* = 1160.80 yields *m/z* = 922.56 (left).

Returning to Figure 4.4, we now discuss the peaks visible above *m/z* = 2000. The most prominent peak, *m/z* = 2067.26, which is 52 mass units heavier than the *m/z* value predicted from the third peak series in Figure 4.2. The mass of this peak seems to correspond to a complex with two Ce atoms and 7 HDA ligands, as shown in the first row of Table 4.2. The following two peaks (*m/z* = 2322.41 and 2578.64) are each separated by 255 mass units, indicating addition of HDA, either as ligands or in an anion cluster. The stoichiometry of the first proposed complex indicates that the carboxylate group of one of the HDA ligands may be bridging the two Ce metal centers. Bridged structures such as these are common in organometallic complexes,[13] and a bridged structure has been hypothesized previously for HDA complexes with other metal ions.[14]

Table 4.2. Observed *m/z* values and masses of proposed di-cerium complexes in Figure 4.4.

***m/z* (Observed)**	**Formula of Proposed Complex or Cluster**	**Neutral MW (amu)**
2067.26	$Ce_2(HDA)_7$	2068.19
2322.41	$Ce_2(HDA)_8$	2323.61
2578.64	$Ce_2(HDA)_9$	2579.03

The remaining peaks in the spectrum in Figure 4.4 could not be identified, but due to their separation by 255 mass units, they also appear to be related to one another by HDA anion clustering. These peaks might be related to higher-order Ce complexes, which have been observed previously. In particular, the dominant peak observed Shirase *et al.* in ESI-MS of their Ce-aryl acid system was identified as a doubly-charged species corresponding to a complex with a $Ce_6O_4(OH)_4$ core and 12 carboxylate ligands.[9] However, the corresponding structure with HDA ligands in this system would be greater than the upper limit of the mass range of the Velos Pro, and thus this species was not observed in these experiments. Additional experiments were conducted by increasing the catalyst loading (from 1% by mole, as in Figure 4.4 up to 10% by mole, not shown), which resulted in subtle changes in the relative intensities of the masses observed in Figure 4.4, but no new peaks. As a result, it seems the formation of the $Ce_6O_4(OH)_4$ core hypothesized by Shirase *et al.* may suppressed by the reaction conditions employed here.

Finally, unsuccessful attempts were made at observing the photocatalysis illustrated in Scheme 4.2, both in the aerosol and in the bulk phase. Aerosols containing HDA and the Ce catalyst were routed through a UV-transparent quartz flow tube and exposed to light from mercury vapor lamps with a peak output at 254 nm, exceeding the required photon energy required to induce LMCT. However, new peaks corresponding to the expected reaction products (ie, ketones and alcohols) were not observed. A bulk experiment was also attempted by placing the HDA-catalyst solution in a cuvette and irradiating it with the same 254 nm Hg lamps over the course of 4 hours. Aliquots of the solution were taken every hour and introduced into the mass spectrometer *via* the atomization technique described earlier, but still no appreciable change in products was observed. As a result, a different catalytic reaction with faster kinetics may be required to observe chemistry on the timescales accessible to aerosol analytical techniques.

4.4 Summary and Outlook

In conclusion, much remains to be done in order to observe organocerium photocatalysis in aerosols. However, the results shown here indicate that submicron droplets formed by atomization of organic solvents, such as hexanes, can successfully deliver a Ce (IV) photocatalyst and target reactant. Additionally, the resulting Ce metal-ligand complexes can be detected by ambient pressure ionization mass spectrometry methods, with experiments conducted using an extractive electrospray technique indicating that the most abundant complexes visible in aerosols contain a single Ce center. Several peaks corresponding to complexes with at least 2 Ce centers were observed, but structures corresponding to the highly-coordinate $Ce_6O_4(OH)_4$ core observed by Shirase *et al.*[9] were not apparent under these conditions. Although experimental evidence of a photocatalytic reaction was not immediately apparent in bulk or in aerosol measurements under irradiation by UV light, future experiments still hold the potential to successfully observe particle-

phase photocatalysis through the optimization of the reaction conditions and through advances in the design of surface-active catalyst species.

4.5 References

(1) Yin, H.; Carroll, P. J.; Anna, J. M.; Schelter, E. J. Luminescent Ce(III) Complexes as Stoichiometric and Catalytic Photoreductants for Halogen Atom Abstraction Reactions. *J. Am. Chem. Soc.* **2015**, *137* (29), 9234–9237. https://doi.org/10.1021/jacs.5b05411.

(2) Yin, H.; Jin, Y.; Hertzog, J. E.; Mullane, K. C.; Carroll, P. J.; Manor, B. C.; Anna, J. M.; Schelter, E. J. The Hexachlorocerate(III) Anion: A Potent, Benchtop Stable, and Readily Available Ultraviolet A Photosensitizer for Aryl Chlorides. *J. Am. Chem. Soc.* **2016**, *138* (50), 16266–16273. https://doi.org/10.1021/jacs.6b05712.

(3) Hu, A.; Guo, J.-J.; Pan, H.; Zuo, Z. Selective Functionalization of Methane, Ethane, and Higher Alkanes by Cerium Photocatalysis. *Science* **2018**, *361* (6403), 668–672. https://doi.org/10.1126/science.aat9750.

(4) Abderrazak, Y.; Bhattacharyya, A.; Reiser, O. Visible-Light-Induced Homolysis of Earth-Abundant Metal-Substrate Complexes: A Complementary Activation Strategy in Photoredox Catalysis. *Angew Chem Int Ed* **2021**, *60* (39), 21100–21115. https://doi.org/10.1002/anie.202100270.

(5) An, Q.; Xing, Y.-Y.; Pu, R.; Jia, M.; Chen, Y.; Hu, A.; Zhang, S.-Q.; Yu, N.; Du, J.; Zhang, Y.; Chen, J.; Liu, W.; Hong, X.; Zuo, Z. Identification of Alkoxy Radicals as Hydrogen Atom Transfer Agents in Ce-Catalyzed C–H Functionalization. *J. Am. Chem. Soc.* **2023**, *145* (1), 359–376. https://doi.org/10.1021/jacs.2c10126.

(6) Yang, Q.; Wang, Y.-H.; Qiao, Y.; Gau, M.; Carroll, P. J.; Walsh, P. J.; Schelter, E. J. Photocatalytic C–H Activation and the Subtle Role of Chlorine Radical Complexation in Reactivity. *Science* **2021**, *372* (6544), 847–852. https://doi.org/10.1126/science.abd8408.

(7) Zeng, M.; Wilson, K. R. Experimental Evidence That Halogen Bonding Catalyzes the Heterogeneous Chlorination of Alkenes in Submicron Liquid Droplets. *Chem. Sci.* **2021**, *12* (31), 10455–10466. https://doi.org/10.1039/D1SC02662C.

(8) Zeng, M.; Liu, C.-L.; Wilson, K. R. Catalytic Coupling of Free Radical Oxidation and Electrophilic Chlorine Addition by Phase-Transfer Intermediates in Liquid Aerosols. *J. Phys. Chem. A* **2022**, *126* (19), 2959–2965. https://doi.org/10.1021/acs.jpca.2c00291.

(9) Shirase, S.; Tamaki, S.; Shinohara, K.; Hirosawa, K.; Tsurugi, H.; Satoh, T.; Mashima, K. Cerium(IV) Carboxylate Photocatalyst for Catalytic Radical Formation from Carboxylic Acids: Decarboxylative Oxygenation of Aliphatic Carboxylic Acids and Lactonization of Aromatic Carboxylic Acids. *J. Am. Chem. Soc.* **2020**, *142* (12), 5668–5675. https://doi.org/10.1021/jacs.9b12918.

(10) Reynolds, R.; Ahmed, M.; Wilson, K. R. Constraining the Reaction Rate of Criegee Intermediates with Carboxylic Acids during the Multiphase Ozonolysis of Aerosolized Alkenes. *ACS Earth Space Chem.* **2023**. https://doi.org/10.1021/acsearthspacechem.3c00026.

(11) Gallimore, P. J.; Kalberer, M. Characterizing an Extractive Electrospray Ionization (EESI) Source for the Online Mass Spectrometry Analysis of Organic Aerosols. *Environ. Sci. Technol.* **2013**, *47* (13), 7324–7331. https://doi.org/10.1021/es305199h.

(12) Manura, J. J.; Manura, D. J. Isotope Distribution Calculator and Mass Spec Plotter. https://www.sisweb.com/mstools/isotope.htm (accessed 2024-10-07).

(13) Miessler, G. L.; Fischer, P. J.; Tarr, D. A. *Inorganic Chemistry*, Fifth ed.; Pearson: Boston, 2014.

(14) Abdullah, N.; Al-Hakem, Y.; Abdullah, N.; Samsudin, H.; Ahmad Tajidi, N. S. Room-Temperature Magnetic Liquid Complexes of 2-Hexyldecanoato Ligand with Cu(II), Ni(II) and Co(II) Ions. *Asian J. Chem.* **2014**, *26* (4), 987–990. https://doi.org/10.14233/ajchem.2014.15714.

Chapter 5. Conclusions

This concluding chapter will summarize and synthesize the key points discussed and key themes explored in this thesis, which center on the important role that reactive intermediates in the kinetics of reactions in aerosols comprising organic constituents. Experiments constructed around measurements of effective uptake coefficients can reveal the role which various transport and reaction phenomena play in multiphase reactions (Chapter 1). In particular, they offer a way to quantitatively explore the competition between chain cycling and chain termination steps in complex reaction mechanisms, and to distinguish chemical effects on reaction kinetics from those induced by transport limitations.

The majority of the work presented herein addresses the contribution of stabilized Criegee Intermediates (sCIs) formed by ozonolysis to oxidation in the particle phase. New applications of aerosol-sensitive mass spectrometry techniques, such as ambient pressure chemical ionization mass spectrometry methods, were used to probe the secondary reactivity in aerosols, providing more direct kinetic access to the decay kinetics of sCI (Chapter 2). Following on the discovery of the importance of sCI-driven chain cycling chemistry in ozonolysis during the particle phase, the importance of accurate measurements of particle-phase rate constants for sCI reacting carboxylic acids in atmospheric particulate matter became apparent. By measuring the decay of HDA with ozone exposure, it was shown that HDA scavenges CIs at rates comparable to competing unimolecular pathways involving sCIs, and kinetic modeling yielded an estimate of the branching ratio between these reactions. In combination with theoretical estimates of the rate of unimolecular sCI reactions and stochastic kinetic simulations of the chemistry, a sCI + acid rate constant could be inferred that is six orders of magnitude slower than the expected diffusion limit in a liquid organic matrix. This result raised many new questions, including whether the barrierless gas phase mechanism for the sCI + acid reaction holds true in the particle phase.

Further investigation of the thermodynamics of this reaction were conducted to explore how the branching ratio between unimolecular and bimolecular sCI reactions, and thus between chain-propagating and chain-terminating chemistry in the particle phase, changes with temperature (Chapter 3). A temperature-controlled flow tube study was conducted, and showed that the effective uptake of ozone in neat Tri aerosols increased by a factor of two as temperature decreased from 293 K to 263 K. Although low temperatures are expected to decelerate the unimolecular sCI reactions that drive chain propagation chemistry, the particle-phase reaction kinetics did not appear diminished at low temperatures. Instead, increased ozone solubility at low temperatures increased the sCI population sufficiently to keep chain cycling reactions competitive. When HDA was again incorporated into the aerosols at low temperature, the decay kinetics suggested that the rate of the chain-terminating bimolecular reaction between sCIs and HDA were still competitive with sCI unimolecular chemistry. As a result, a substantial activation energy to the sCI + acid reaction step in the particle phase could be inferred, on the order of 40 kJ mol^{-1}. This energy barrier maintains a balanced branching ratio between chain propagation and termination reactions over the 263–293 K temperature range. These results indicate that the composition of the particle phase might play the most important role in determining the overall chemical mechanism of particle-phase transformations during ozonolysis at low temperatures. Further studies should explore the role of gas-surface interactions in enhancing the rates of reactions that are slow in the particle phase, *e.g.* reactions between sCI and carboxylic acid groups that reside on the surface of aerosol particles.

Additionally, more careful characterization of the phase and diffusion properties of the model aerosol used in these studies, both before and during reaction at low temperatures, would greatly improve the uncertainties of kinetic predictions at low temperatures. Measurements of effective particle density, or other measurements that directly probe the viscosity of collected samples of the particles, could aid in accomplishing this goal.

Finally, several of the techniques explored in the preceding chapters were applied to a novel system with applications in synthetic chemistry and heterogeneous catalysis (Chapter 4). A prototype was developed of a delivery system for organocerium photocatalysts in aerosols composed of organic solvent droplets, with an eye to eventually investigating the catalytic mechanism, as well as informing future catalyst design for such applications. While catalytic activity was not observed upon irradiation, progress was made toward identifying the structure of the ligand-metal complexes which form in particle-phase solutions of catalysts and reactants, finding that primarily singly-charged, four-coordinate complexes with 1 or 2 Ce centers were formed, with some evidence for complexes for higher-order complexes. This investigation will aid in the design of future iterations of this system and help constrain the classes of reactions to be considered for future studies. In the future, measurements of kinetics, such as the uptake coefficients of gas-phase feedstock molecules, may reveal new ways to optimize reaction efficiency and catalyst design. To this end, any future work should first identify a target reaction and set of reactants whose bulk kinetics are sufficiently fast to be observed on the timescales required for aerosol measurements.

In conclusion, the study of reactive intermediates in organic aerosols has the potential to bring together discoveries in gas-phase, condensed-phase, and interfacial chemistry to explore how species such as radicals, Criegee intermediates, and even metal-ligand complexes preside over myriad chemical transformations in aerosol particles. It is my hope that the findings presented here will enable a deeper understanding of not only aerosol aging in the atmosphere, especially at low temperatures, but also of multiphase oxidation reactions wherever they are encountered.